Raman spectroscopy and single-photon source in an ion-cavity system

Dissertation

zur Erlangung des Doktorgrades an der
Fakultät für Mathematik, Informatik und Physik
der Leopold-Franzens-Universität Innsbruck

vorgelegt von

Helena Gonçalves de Barros

durchgeführt am Institut für Experimentalphysik
unter der Leitung von
Univ.-Prof. Dr. Rainer Blatt

Innsbruck, January 2010

Abstract

The study of the interaction between single photons and single atoms represents a fundamental step in the understanding of more complex quantum systems. A single atom coupled to the electromagnetic field of a resonator provides the ideal system for this purpose.

The work presented in this thesis explores the interaction between a single trapped $^{40}Ca^{+}$ ion and the electromagnetic field inside a high-finesse optical cavity. The coupling takes place via the use of a vacuum stimulated Raman transition, composed of a drive laser operating at a wavelength of 397 nm and a high-finesse optical cavity resonant to 866 nm light. This transition transfers atomic population from the $S_{1/2}$ to the $D_{3/2}$ manifolds of the calcium ion producing a photon in the cavity. This photon is measured and properties of the system are evaluated.

Spectroscopy measurements of the Raman transitions are performed and all possible transitions are identified for different polarizations of both drive laser and cavity fields. Theoretical data obtained using calibrated parameters is in good agreement with the experimental results, supporting our understanding of the system's behavior. The secular motion of the ion in the trap is visible in the experimental spectra in form of sidebands, offering prospects for cavity-assisted sideband cooling. Furthermore, mapping of the cavity standing wave via the Raman transition is performed and a reduction of its contrast is observed for the case of a hot ion, confirming the impact of motion on the ion-cavity interaction.

The system is also used to deterministically produce single photons. The single-photon creation efficiency obtained in this work overcomes previous ion-cavity setups and is comparable to state-of-the-art systems composed of a neutral atom and a cavity operating in the strong coupling regime. Simulation curves quantitatively match the experimental results within calibration error bars.

Entanglement between a single ion and a cavity photon represents one of the near-future goals of this project. To make this operation possible, a laser addressing the $S_{1/2} \leftrightarrow D_{5/2}$ quadrupole transitions is introduced for coherent control of the ion's internal state. Preliminary results are provided, including spectroscopic measurements and a first step towards sideband cooling to the ground state of motion.

Zusammenfassung

Die Untersuchung der Wechselwirkung zwischen einzelnen Photonen und einzelnen Atomen ist ein wesentlicher Schritt im Verständnis komplexerer Quantensysteme. Ein einzelnes Atom, welches an eine einzelne Mode des elektromagnetischen Felds koppelt, stellt hierfür ein ideales System dar.

Diese Arbeit untersucht die Wechselwirkung zwischen einem einzelnen gefangen $^{40}Ca^{+}$ Ion und dem elektromagnetischen Feld in einem optischen Hochfinesse-Resonator. Die Kopplung erfolgt über einen vakuum-stimulierten Ramanübergang, der von einem Laser bei einer Wellenlänge von 397 nm und einem bei 866 nm mit einer Mode resonanten optischen Resonator getrieben wird. Dieser Übergang bringt die atomaren Population von der $S_{1/2}$ zur $D_{3/2}$ Mannigfaltigkeit des Calcium Ions, wobei ein Photon im Resonator erzeugt wird. Dieses Photon verlässt den Resonator durch einen der beiden Spiegel und wird in einem Hanbury-Brown & Twiss Aufbau detektiert. Dieser Aufbau ermöglicht es neben der Messung der Intensität auch zeitliche Korrelationen zwischen Photonen zu bestimmen und so die Eigenschaften des Systems zu untersuchen.

Spektroskopische Messungen der Ramanübergänge werden durchgeführt und alle möglichen Übergänge für unterschiedliche Polarisationen des Lasers bei 397 nm und des Feldes im Resonator identifiziert. Die gute Übereinstimmung von theoretischen Simulationen mit den experimentellen Ergebnissen zeugen von gutem Verständnis des Systems. Die säkulare Bewegung der Ionen in der Falle ist in den experimentellen Spektren in Form von Seitenbändern sichtbar, was in zukünftigen Experimenten Resonator-Seitenband-Kühlung ermöglichen könnte. Außerdem wird die optische Stehwelle des Resonators über den Ramanübergang vermessen. Dabei wird im Falle eines heißen Ions ein reduzierter Kontrast beobachtet, was eine direkte Konsequenz der Delokalisierung des Ions entlang der Stehwelle aufgrund der Bewegung ist.

Das System wurde auch als deterministische Einzelphotonenquelle betrieben. Die Effizienz der Erzeugung einzelner Photonen übertrifft die früherer Ionen-Resonator-Systeme und ist vergleichbar mit aktuellen Systemen, in welchen ein neutrales Atom im Bereich der starken Kopplung an einen Hohlraum-Resonator gekoppelt ist. Die

theoretischen Simulationen entprechen den experimentellen Ergebnissen innerhalb der Fehlergrenzen.

Die Verschränkung zwischen einem einzelnen Ion und einem Resonator-Photon ist eines der Ziele des Projektes in näherer Zukunft. Hierfür wird ein Laser benötigt, der den $S_{1/2} \leftrightarrow D_{5/2}$ Quadrupolübergang treibt und somit die kohärente Kontrolle des internen Zustand des Ions erlaubt. Es werden vorläufige Ergebnisse gezeigt: Spektroskopischen Messungen und ein erster Schritt in Richtung Seitenband-Kühlung in den Grundzustand der Bewegung.

Contents

1 Introduction

The interaction between light and matter has been a subject of interest for a long time. The description of the light as a wave has been introduced by Thomas Young in the beginning of the 19th century, when he observed the interference of light in his famous double-slit experiment. Until then, light had been described as being composed of particles in the Newtonian theory of optics. This idea of particles returned in the beginning of the 20th century, when Einstein stated his "light quantization hypothesis". In a series of papers [1–5], he laid out the idea that a light ray consisted of a finite number of energy quanta, which could only be produced or absorbed in complete units. His description of the photoelectric effect [1] constitutes the first application of quantum electrodynamics (QED).

In 1946, Purcell published his observation on enhancement of spontaneous emission of nuclear magnetic moment transitions when coupled to a resonant circuit [6], known today as the Purcell effect. Enhancement of atomic spontaneous emission in resonant cavities has been first reported by Goy *et al.* in 1983 [7]. In this experiment, Rydberg atoms of sodium were resonantly excited at 340 GHz in a superconducting niobium cavity. The first observations of the Purcell effect on optical transitions came with the work of Heinzen *et al.* in 1987 [8, 9]. With this discovery by Purcell and others, the field of cavity quantum electrodynamics emerged, centered on the study of the interaction between atomic systems and electromagnetic fields inside resonators [10–14].

Many experimental approaches for exploring this interaction have been adopted in research laboratories worldwide. Rydberg atoms flying through microwave cavities [15], superconducting two-level systems coupled to transmission line resonators [16], monolithic semiconductor microcavities with quantum wells as active medium [17], quantum dots in semiconductor microresonators [18, 19] and single neutral [12] or charged [20–22] atoms interacting with high-finesse optical cavities are examples of experiments developed in this research field. Fundamental properties of these systems like the observation of the vacuum Rabi splitting [23, 24] and Rabi oscillations using the cavity field [25, 26], investigation of the dynamics of atoms inside cavities [27] and the forces exerted by single photons on these atoms [28] have been studied.

This work focuses on the interaction of a single calcium ion trapped inside a high-finesse optical resonator via vacuum-stimulated Raman transitions. Characteristics of this system are examined through spectroscopy measurements of these transitions [29], which allows us to explore the behavior of the ion-cavity system and observe the influences of motion on this interaction. The understanding of such fundamental properties opens the way for future applications of cavity QED systems.

Specifically, the interaction of a single atom with a single mode of the electromagnetic field presents promising prospects in quantum information science [30–33]. The success of quantum computation protocols relies on the precise coherent control of the atom-field interaction. This can be achieved by placing single trapped neutral or charged atoms inside high-finesse optical resonators. For neutral atoms, entanglement between two photons mediated by an atom [34] and reversible mapping of a photonic state to an atomic state [35] have been achieved. Trapped ions, however, present some advantages when compared to neutral atoms. Despite the challenge of achieving strong coupling to high-finesse cavities, trapped ions allow for a better control of the interaction due to their well-localized position in space [20–22]. Additionally, the much longer trap lifetimes of ions yields the implementation of potentially elaborate quantum information processing protocols. Furthermore, successful implementation of quantum computation protocols in trapped ions using phonons [36–41] and, more recently, photons in free space [42–45] to couple two ions provide a rich background for the investigation of quantum information in ion-cavity systems. Entanglement and state mapping between ions and photons in such setups have yet to be demonstrated.

An important step toward establishing these goals lies in the deterministic production of single photons [33, 46]. Single photons act as basis elements in both linear optical quantum computing and quantum cryptography [47–49] and as 'flying qubits' traveling between the nodes of a quantum network [31, 50]. The generation of single photons through the process of spontaneous decay from a single excited emitter has been demonstrated in diverse systems [51], for example in molecules [52, 53], color centers in diamonds [54, 55], quantum dots [56, 57], neutral atoms [58] and ions [59, 60]. Nonetheless, poor collection efficiency and lack of determinism in such procedures favor the use of vacuum stimulated transitions for single photon production, as has been realized for single atoms [61, 62] and single ions [63] trapped inside optical resonators.

Here, a deterministic and high-efficiency single-photon source is reported [64]. The single photon creation efficiency obtained is considerably superior to previously

reported single-photon sources in ion-cavity systems [63, 65] and is comparable to state-of-the-art results in neutral atoms inside high-finesse optical resonators [61]. The high-efficiency and deterministic production of single photons together with the fundamental investigations of the ion-cavity system presented in this work provide some of the necessary tools for achieving a coherent atom-photon interface useful in quantum information science.

This thesis begins with the basic quantum theory of two and three-level atomic systems interacting with the electromagnetic field of lasers and a cavity, in chapter 2. The master equation formalism is introduced followed by a discussion on Raman transitions in the context of an effective two-level system.

In chapter 3, a theoretical model describing the experimental situation is introduced. This more realistic model involves eight atomic levels and two orthogonally polarized cavity modes. It is based on the master equation formalism and dissipation mechanisms are included via collapse operators in a dissipation Liouvillian. Steady-state solutions as well as time dependent ones are obtained, the latter via the numerical integration of the equations of motion. The theory presented in this chapter is used for simulating the experimental situation of chapters 5 and 6, using as input parameters the values obtained from calibration experiments.

An overview of the experimental setup is given in chapter 4. The ion trap is introduced, followed by a description of the high-finesse optical cavity, where some of its important characteristics are shown. Information about the laser systems used in the experiments is provided, including the transfer lock system for the cavity. Two geometric configurations of the laser beams and magnetic field are depicted and the detection devices and also the computer-hardware interface are explained.

Chapter 5 starts with a description of the calibration experiments used to obtain values of experimental parameters to be used in the simulations. Cavity standing wave measurements are then shown, where the effects of Doppler cooling on the cavity-ion interaction become apparent. Raman spectroscopy measurements are presented for different polarizations of both drive laser and cavity photons. The presence of sidebands on these spectra manifests the motion of the ion in the trap.

A high-efficiency single-photon source is reported in chapter 6. Results on the second-order correlation function and on the temporal pulse shape of the cavity photon are shown. A simulation of the temporal evolution of the atomic populations is provided and the coherence of the photon generation process is simulated.

Preliminary experimental results on the $S_{1/2} \leftrightarrow D_{5/2}$ quadrupole transition are presented in chapter 7. It is the only chapter that does not involve the high-finesse optical cavity. Its purpose is to show initial investigative experiments on

this transition, essential for future work. The spectrum of one carrier transition is presented, together with its first order secular motion sidebands. Rabi oscillations on one carrier are shown, followed by preliminary Ramsey experiment results required for frequency stabilizing the laser to the ion. Finally, measurements on sideband cooling are reported, demonstrating significant reduction of the red axial motional sideband.

A summary and outlook of the work described in this thesis is provided in the last chapter. Current problems and future perspectives are discussed, including ideas for new experimental setups. Two appendices are further added to this thesis to describe side experiments reporting on the APDs afterpulsing phenomenon and the mechanical instability of both cavity and trap.

2 Theory of two and three-level atoms

The basic theory behind the interaction of an atom with an electromagnetic field is presented in this chapter. In particular, the description of a two-level atom interacting with the fields of a laser and a cavity is developed. This treatment is then expanded to a three-level atomic system under the influence of two lasers and a cavity field, in a fashion that resembles the experiments to be presented. Dissipation mechanisms are considered and the master equation is introduced. A more realistic and detailed description of the experimental situation is left for chapter 3.

2.1 Two-level atom interacting with an electric field

The level scheme of an atom composed of the ground state $|\downarrow\rangle$ and the excited state $|\uparrow\rangle$, separated by the energy $\hbar\omega_a$, is depicted in figure 2.1. In the presence of an electric field, the system can be described in quantum mechanics by the Hamiltonian

$$\hat{\mathcal{H}} = \hat{\mathcal{H}}_0 + \hat{\mathcal{H}}_I. \tag{2.1}$$

The first term of this Hamiltonian represents the bare system, constituted by the bare field Hamiltonian (discussed in the next subsections) and by the bare atom Hamiltonian [66] given by

$$\hat{\mathcal{H}}_{0\text{atom}} = \hbar\omega_a\hat{\sigma}_z, \tag{2.2}$$

where $\hat{\sigma}_z = |\uparrow\rangle\langle\uparrow| - |\downarrow\rangle\langle\downarrow|$ is one of the Pauli matrix operators.

The second term of equation 2.1 expresses the interaction between the atom and the applied electric field, which can be written in the dipole approximation as

$$\hat{\mathcal{H}}_I = -\hat{\boldsymbol{d}} \cdot \hat{\mathrm{E}}., \tag{2.3}$$

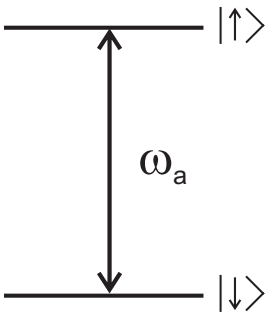

Figure 2.1: Level scheme of a two-level atom of ground state $|\downarrow\rangle$ and excited state $|\uparrow\rangle$, separated by the energy $\hbar\omega_a$.

where $\hat{\boldsymbol{d}} = -e\hat{\boldsymbol{r}}$ is the electric dipole operator of the atom and $\hat{\mathrm{E}}$ is the electric field operator.

The atomic dipole moment operator [67] can be written in terms of the raising and lowering Pauli operators $\hat{\sigma}^\dagger = |\uparrow\rangle\langle\downarrow|$ and $\hat{\sigma} = |\downarrow\rangle\langle\uparrow|$, respectively, as

$$\hat{\boldsymbol{d}} = -[(\hat{\sigma}^\dagger + \hat{\sigma})D_{\downarrow\uparrow}]\boldsymbol{d}_\downarrow^\uparrow. \tag{2.4}$$

Here, $\boldsymbol{d}_\downarrow^\uparrow$ is a vector expressing the direction of the dipole moment and with amplitude given by the Clebsch-Gordan coefficient associated to the transition $|\downarrow\rangle \leftrightarrow |\uparrow\rangle$ [68]. The parameter [69]

$$D_{\downarrow\uparrow} = \frac{1}{2\pi}\sqrt{3\hbar\varepsilon_0\lambda^3\gamma_{\downarrow\uparrow}} \tag{2.5}$$

is the reduced electric dipole moment of this transition, where $\gamma_{\downarrow\uparrow}$ and λ are the transition's half linewidth and wavelength, respectively, and ε_0 stands for the vacuum permittivity.

Considering a plane wave of frequency ω, wavevector $\boldsymbol{k}$ and amplitude E_0, the electric field operator at a position $\boldsymbol{r}$ and a time t can be written in the following quantized way

$$\hat{\mathrm{E}}(\boldsymbol{k}, \boldsymbol{r}, t) = \mathrm{E}_0[\hat{a}e^{-i(\omega t - \boldsymbol{k}\cdot\boldsymbol{r})} + \hat{a}^\dagger e^{i(\omega t - \boldsymbol{k}\cdot\boldsymbol{r})}]\boldsymbol{\epsilon}. \tag{2.6}$$

The parameters $\hat{a}^\dagger$ and $\hat{a}$ are the photon creation and annihilation operators and $\boldsymbol{\epsilon}$ is the unitary vector representing the direction of polarization of the electric field. The amplitude of the electric field can be written in terms of the quantization volume V and the field angular frequency ω as

$$\mathrm{E}_0 = \sqrt{\frac{\hbar\omega}{2\varepsilon_0 V}}. \tag{2.7}$$

The electric field applied to the atom is here attributed to two possible sources:

an optical cavity and a laser. The appropriate theoretical treatment of each case is provided in the next subsections.

2.1.1 Electric field of a single cavity mode

The field inside a cavity forms a standing wave, which can be described by the sum of two counter-propagating plane waves of equal amplitude and frequency. Based on equation 2.6, the cavity electric field operator, $\hat{\mathrm{E}}_{\mathrm{cav}}$, can be written as

$$\begin{aligned}\hat{\mathrm{E}}_{\mathrm{cav}}(\boldsymbol{k},\boldsymbol{r},t) &= \hat{\mathrm{E}}(\boldsymbol{k},\boldsymbol{r},t)+\hat{\mathrm{E}}(-\boldsymbol{k},\boldsymbol{r},t)\\ &= \mathrm{E}_0\cos(\boldsymbol{k}\cdot\boldsymbol{r})(ae^{-i\omega t}+\hat{a}^{\dagger}e^{i\omega t})\boldsymbol{\epsilon}. \end{aligned} \tag{2.8}$$

For a cavity length L and a Gaussian mode of waist w_0 and volume $V = L\pi w_0^2/4$ we have[1]

$$\mathrm{E}_{0\mathrm{cav}} = \sqrt{\frac{2\hbar\omega}{\varepsilon_0 L\pi w_o^2}}. \tag{2.9}$$

The Hamiltonian representing the resonant interaction between the atom and the cavity field then reads

$$\begin{aligned}\hat{\mathcal{H}}_{\mathrm{Icav}} &= -\hat{\boldsymbol{d}}\cdot\hat{\mathrm{E}}_{\mathrm{cav}}\\ &= D_{\downarrow\uparrow}\sqrt{\frac{2\hbar\omega}{\varepsilon_0 L\pi w_o^2}}\cos(\boldsymbol{k}\cdot\boldsymbol{r_0})\cdot(\hat{\sigma}^{\dagger}+\hat{\sigma})(\hat{a}e^{-i\omega t}+\hat{a}^{\dagger}e^{i\omega t})\boldsymbol{\epsilon}\cdot\boldsymbol{d}_{\downarrow}^{\uparrow}\end{aligned} \tag{2.10}$$

The term [2]

$$g = D_{\downarrow\uparrow}\sqrt{\frac{2\omega}{\hbar\varepsilon_0 L\pi w_o^2}}\cos(\boldsymbol{k}\cdot\boldsymbol{r_0}) \tag{2.11}$$

can be identified as half of the Rabi frequency of the resonant cavity field. The Rabi frequency represents the rate at which the transition is coherently driven between the two atomic levels. The cosine dependence of g on the position r_0 of the atom in the cavity standing wave indicates a maximum coupling between atom and cavity at the cavity field antinode ($\cos(\boldsymbol{k}\cdot\boldsymbol{r_0}) = 1$) and a minimum coupling at the cavity

[1] In reality, for the experimental situation this value is only valid at the center of the cavity. As the cavity configuration is close to concentric (see section 4.2), the amplitude of the electric field has a tight focus and the field distribution is that of a Gaussian beam [70].

[2] Following the comment on footnote 1, this value is only valid when the ion is positioned around the cavity center. The cavity-ion coupling is in fact dependent on z and therefore varies along the cavity axis.

field node ($\cos(\boldsymbol{k}\cdot\boldsymbol{r_0})=0$). The maximum value of g is thus

$$g_0 = \sqrt{\frac{3c\lambda^2\gamma_{\downarrow\uparrow}}{\pi^2 L w_0^2}}. \tag{2.12}$$

A single mode of the cavity field can be represented by a harmonic oscillator [71], with the following bare Hamiltonian

$$\hat{\mathcal{H}}_{0\text{cav}} = \hbar\omega_c \hat{a}^\dagger \hat{a}, \tag{2.13}$$

where $\hbar\omega_c$ is the energy difference between two consecutive harmonic oscillator levels, as shown in figure 2.2, and $\hat{a}^\dagger$ and $\hat{a}$ are the creation and annihilation operators of the cavity field, respectively.

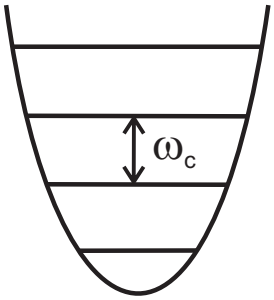

Figure 2.2: Harmonic oscillator representing a single mode of the cavity.

The overall Hamiltonian of the cavity-atom system is a sum of the bare cavity and atom and the interaction Hamiltonians as follows

$$\hat{\mathcal{H}} = \hbar\omega_a\hat{\sigma}_z + \hbar\omega_c\hat{a}^\dagger\hat{a} + \hbar g(\hat{\sigma}^\dagger + \hat{\sigma})(\hat{a}e^{-i\omega t} + \hat{a}^\dagger e^{i\omega t})\boldsymbol{\epsilon}\cdot\boldsymbol{d}_{\downarrow}^{\uparrow}. \tag{2.14}$$

This is the so-called Jaynes-Cummings Hamiltonian [72].

Using the rotating wave approximation [73] to eliminate the fast oscillating terms, this Hamiltonian assumes the simpler form

$$\hat{\mathcal{H}} = \hbar\omega_a\hat{\sigma}_z, + \hbar\omega_c\hat{a}^\dagger\hat{a} + \hbar g(\hat{\sigma^\dagger}\hat{a} + \hat{\sigma}\hat{a}^\dagger). \tag{2.15}$$

The term $\boldsymbol{\epsilon}\cdot\boldsymbol{d}_{\downarrow}^{\uparrow}$ is here considered equal to one due to the parallel alignment of the atomic dipole moment vector along the direction of the applied electric field and also assuming a fictitious Clebsch-Gordan coefficient of one[3].

Now the exchange of energy between atom and cavity field becomes more intuitive. The term $\hbar g\hat{\sigma^\dagger}\hat{a}$ represents an atom absorbing a photon (the atom gains a

[3]This approximation is used throughout the rest of this chapter. More realistic values of the term $\boldsymbol{\epsilon}\cdot\boldsymbol{d}_{\downarrow}^{\uparrow}$ are considered in chapter 3.

quantum of energy, $\hat{\sigma}^\dagger$ brings it to the upper energy state) from the cavity field (the cavity loses one photon, $\hat{a}$ lowers its photon number). The term $\hbar g\hat{\sigma}\hat{a}^\dagger$ represents the emission of a photon by the atom (the atom loses a quantum of energy, $\hat{\sigma}$ brings it to the lower energy state) into the cavity field (the cavity gains a photon, $\hat{a}^\dagger$ raises its photon number).

2.1.2 Electric field of a laser

The interaction of a two-level atom with a laser field resembles the interaction of the two-level atom with a cavity field presented in the last section. In the case of the laser, however, we assume that the loss and gain of photons by the laser field remains small and therefore does not influence the overall laser field (no bare field Hamiltonian required). This way, a semi-classical approximation of the Jaynes Cummings Hamiltonian is used, where the electric field operator $\hat{\mathrm{E}}_{\mathrm{laser}}$ is replaced by its expectation value $\mathrm{E}_{\mathrm{laser}}$, given by

$$\mathrm{E}_{\mathrm{laser}}(\boldsymbol{k},\boldsymbol{r},t) = \mathrm{E}_{0\mathrm{laser}}\cos(\omega t - \boldsymbol{k}\cdot\boldsymbol{r})\boldsymbol{\epsilon}. \tag{2.16}$$

The Hamiltonian describing the resonant interaction between the atom and the laser reads

$$\hat{\mathcal{H}}_{\mathrm{Ilaser}} = -\hat{\boldsymbol{d}}\cdot\hat{\mathrm{E}}_{\mathrm{laser}} \quad = \quad D_{\downarrow\uparrow}\mathrm{E}_{0\mathrm{laser}}\cos(\omega t - \boldsymbol{k}\cdot\boldsymbol{r})\cdot(\hat{\sigma}^\dagger + \hat{\sigma}). \tag{2.17}$$

Using the rotating wave approximation and assuming that the motion of the ion can be neglected ($z_0 k \ll 1$, which allows us to set $r = 0$), the previous interaction Hamiltonian can be rewritten as

$$\hat{\mathcal{H}}_{\mathrm{Ilaser}} \quad = \quad \frac{D_{\downarrow\uparrow}\mathrm{E}_{0\mathrm{laser}}}{2}\cdot(\hat{\sigma}^\dagger e^{-i\omega t} + \hat{\sigma}e^{i\omega t}).$$

From the expression above, the Rabi frequency of the laser field, Ω_{laser}, can be identified as

$$\Omega_{\mathrm{laser}} = \frac{D_{\downarrow\uparrow}\mathrm{E}_{0\mathrm{laser}}}{\hbar} = \sqrt{\frac{3\varepsilon_0\lambda^3\gamma_{\downarrow\uparrow}}{4\pi^2\hbar}}\mathrm{E}_{0\mathrm{laser}}. \tag{2.18}$$

When the laser is continuously applied on resonance with the two-level system, the atomic population undergoes an oscillation between the two levels at a frequency given by Ω_{laser}. If the atom is initially in the $|\downarrow\rangle$ state, after a time interval given by $t_\pi = \pi/\Omega_{\mathrm{laser}}$ the atomic population is completely transferred to the upper state

$|\uparrow\rangle$. This time interval t_π is called π-time and a laser pulse of area $\int \Omega_{\text{laser}}(t)dt = \pi$ is called a π-pulse. Experimental results in section 7.2 demonstrate this oscillatory behavior in the case of a quadrupole atomic transition.

2.2 Three-level atom interacting with lasers and a cavity

This section extends the two-level atom theory presented in the previous section to a three-level atom interacting with both laser and cavity fields. The situation described here is constructed to resemble the experiment, in which two lasers and a cavity interact with the atom as depicted in figure 2.3.

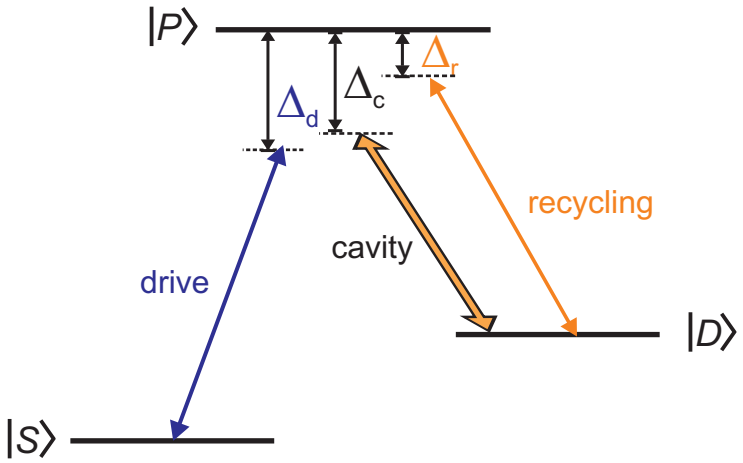

Figure 2.3: Three-level atom interacting with two lasers (drive and recycling) and a cavity.

In this system, the cavity interacts with the atomic transition $|P\rangle \leftrightarrow |D\rangle$ with a resonant atom-cavity coupling rate of $2g$ and a detuning of Δ_c from it. The drive laser addresses the atomic transition $|S\rangle \leftrightarrow |P\rangle$ with a resonant Rabi frequency Ω_d and a detuning Δ_d. The recycling laser acts on the transition $|P\rangle \leftrightarrow |D\rangle$ with a resonant Rabi frequency Ω_r and is detuned from it by Δ_r.

In the experiments, the drive laser and the cavity together form a Raman transition, which is responsible for transferring the atomic population from the $|S\rangle$ to the $|D\rangle$ state. During this process, the atom absorbs one photon from the drive laser and emits one photon into the cavity. The physics of Raman transitions is discussed in the last section of this chapter. The task of the recycling laser is to excite the atom to the state $|P\rangle$, from which it decays 92 % of the time to the initial state $|S\rangle$. Once back to this initial state, the atom can again be addressed by the drive laser and undergo the same cycle, creating cavity photons.

Considering the necessary interactions between atom and fields, this system can be described by the following Hamiltonian

$$\hat{\mathcal{H}} = \hat{\mathcal{H}}_0 + \hat{\mathcal{H}}_{\text{Icav}} + \hat{\mathcal{H}}_{Id} + \hat{\mathcal{H}}_{Ir}, \tag{2.19}$$

where

$$\begin{aligned} \hat{\mathcal{H}}_0 &= \hat{\mathcal{H}}_{0\text{atotm}} + \hat{\mathcal{H}}_{0\text{cav}} && (2.20)\\ &= E_S\hat{\sigma}_{SS} + E_P\hat{\sigma}_{PP} + E_D\hat{\sigma}_{DD} + \hbar\omega_c\hat{a}^\dagger\hat{a} && (2.21) \end{aligned}$$

is the joint Hamiltonian of the bare atom and the bare cavity,

$$\hat{\mathcal{H}}_{\text{Icav}} = \hbar g(\hat{\sigma}_{DP}\hat{a}^\dagger + \hat{\sigma}_{PD}\hat{a}) \tag{2.22}$$

is the Hamiltonian representing the interaction between the atom and the cavity field,

$$\hat{\mathcal{H}}_{Id} = \frac{\hbar\Omega_d}{2}(\hat{\sigma}_{SP}e^{i\omega_d t} + \hat{\sigma}_{PS}e^{-i\omega_d t}) \tag{2.23}$$

is the Hamiltonian representing the interaction between the atom and the drive laser field and

$$\hat{\mathcal{H}}_{Ir} = \frac{\hbar\Omega_r}{2}(\hat{\sigma}_{DP}e^{i\omega_r t} + \hat{\sigma}_{PD}e^{-i\omega_r t}) \tag{2.24}$$

is the Hamiltonian representing the interaction between the atom and the recycling laser field. In the bare atom and bare cavity Hamiltonians, E_S, E_P and E_D are the energies of the levels $|S\rangle$, $|P\rangle$ and $|D\rangle$, respectively, $\hat{\sigma}_{SS} = |S\rangle\langle S|$, $\hat{\sigma}_{PP} = |P\rangle\langle P|$ and $\hat{\sigma}_{DD} = |D\rangle\langle D|$ are their respective projection operators and $\hbar\omega_c$ is the energy of the cavity photons. In the remaining Hamiltonians, $\hat{\sigma}_{SP} = |S\rangle\langle P|$ and $\hat{\sigma}_{DP} = |D\rangle\langle P|$ are the lowering operators of the atom, $\hat{\sigma}_{PS} = |P\rangle\langle S|$ and $\hat{\sigma}_{PD} = |P\rangle\langle D|$ are the raising atomic operators, ω_c, ω_d and ω_r are the angular frequencies of the cavity, drive laser and recycling laser fields and Ω_d and Ω_r are the drive and recycling lasers resonant Rabi frequencies, respectively.

2.3 Dissipation mechanisms and the master equation

In this subsection the dissipative processes are included in the description of the system using the density matrix formalism. References [66, 74, 75] present a more detailed explanation of this subject.

Three dissipation processes are considered here:

- spontaneous emission: the ion looses a photon via spontaneous emission from the $P_{1/2}$ manifold to either the $S_{1/2}$ or the $D_{3/2}$ manifolds at rates $2\gamma_{PS}$ and $2\gamma_{PD}$, respectively;
- cavity decay: the cavity looses a photon to the environment at rate 2κ;
- laser linewidths: a phase noise is introduced due to the finite linewidths of the drive ($2\delta_d$) and recycling ($2\delta_r$) lasers.

Figure 2.4 depicts these dissipation processes, expressed as full linewidths, in a simplified three-level scheme of the atom.

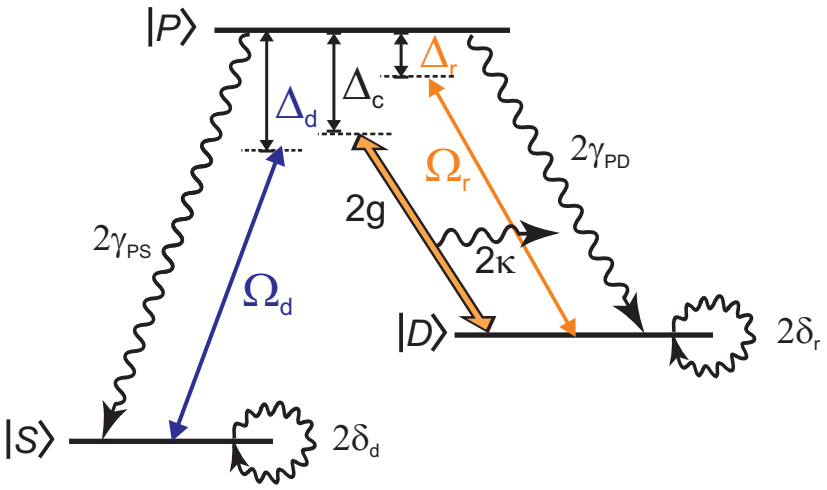

Figure 2.4: Dissipation mechanisms in the three-level atom: spontaneous emission rates from the $P_{1/2}$ manifold to the $S_{1/2}$ ($2\gamma_{PS}$) and to the $D_{3/2}$ ($2\gamma_{PD}$) manifolds; cavity decay rate (2κ) and linewidths of the drive ($2\delta_d$) and recycling lasers ($2\delta_r$). All quantities here are expressed in terms of their full linewidths.

The master equation of the system is given by

$$\frac{d\hat{\rho}}{dt} = -\frac{i}{\hbar}[\hat{\mathcal{H}}, \hat{\rho}] + \mathcal{L}_{diss}(\hat{\rho}) = \mathcal{L}(\hat{\rho}), \tag{2.25}$$

where $[\hat{\mathcal{H}}, \hat{\rho}] = \hat{\mathcal{H}}\hat{\rho} - \hat{\rho}\hat{\mathcal{H}}$ and $\mathcal{L}_{diss}(\hat{\rho})$ is the Liouvillian representing the dissipation mechanisms of the system. This Liouvillian is written in the Lindblad form [76] as

$$\mathcal{L}_{diss}(\hat{\rho}) = \frac{1}{2}\sum_m (2C_m\rho\hat{C}_m^\dagger - \rho\hat{C}_m^\dagger\hat{C}_m - \hat{C}_m^\dagger\hat{C}_m\hat{\rho}), \tag{2.26}$$

with $\hat{C}_m$ representing collapse operators associated to the dissipative processes. These operators are introduced in the next chapter, where a detailed model of the system is presented.

2.4 Raman transition: effective two-level atom

In the usual treatment of Raman transitions, two laser fields of angular frequencies ω_1 and ω_2 and detuned by Δ from an intermediate state $|i\rangle$ coherently couple the states $|g\rangle$ and $|f\rangle$ as depicted in figure 2.5(a). The parameters Ω_1 and Ω_2 shown in this figure are the resonant Rabi frequencies associated with the laser fields 1 and 2, respectively. The intermediate level $|i\rangle$ acts in this process as a virtual level and is only weakly populated. The energy associated with each of these levels is $\hbar\omega_g$ for the initial state, $\hbar\omega_i$ for the intermediary state and $\hbar\omega_f$ for the final state.

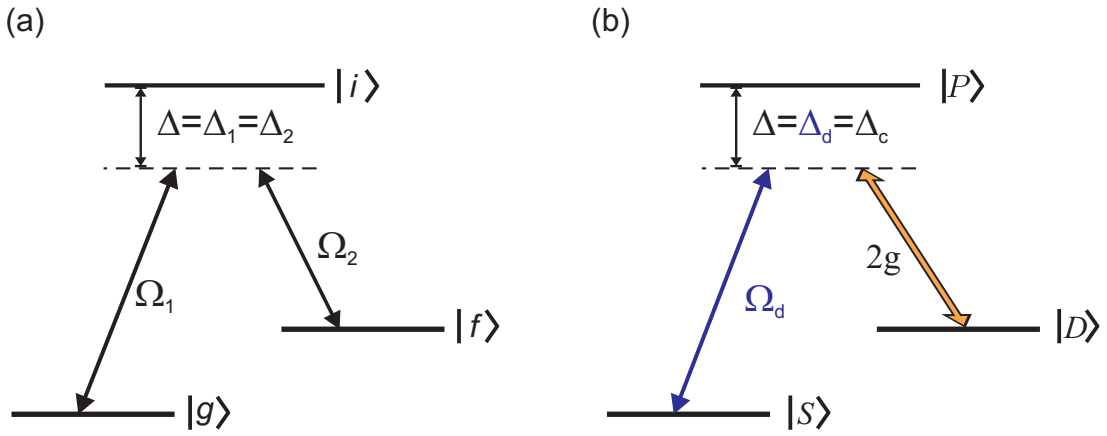

Figure 2.5: (a) Raman transitions represented by two laser fields and (b) by a laser and a cavity field similarly to the experimental system, in a three-level atomic model.

The Raman resonance condition states that the difference in energy between the two fields is similar to the energy difference between the initial and final atomic levels, that is

$$\delta E = (\omega_1 - \omega_2) - (\omega_f - \omega_g) \approx 0. \tag{2.27}$$

Additionally, to avoid populating the intermediate level, it is important that the detuning $\Delta = (\omega_i - \omega_g) - \omega_1$ of the applied field from the intermediary state is large ($|\delta E| \ll |\Delta|$). Based on the simplified treatment of Raman transitions presented in [77], we can define an effective Rabi frequency of the Raman transition, Ω_{eff}, as

$$\Omega_{\text{eff}} = \frac{\Omega_1 \Omega_2}{2\Delta}. \tag{2.28}$$

In a case that resembles the experimental situation, shown in figure 2.5(b), field 1 corresponds to the drive laser and field 2 corresponds to the cavity. Therefore, in the experimental system the effective Rabi frequency of the Raman transition reads[4]

$$\Omega_{\text{eff}} = \frac{\Omega_d(2g)}{2\Delta}. \tag{2.29}$$

More detailed and involved calculations on effective two-level systems and Raman transitions can be seen in [65, 78–81].

Coherent versus incoherent coupling

When studying the interaction between a single atom and an electromagnetic field inside a resonator, it is very important to consider the decoherence of the system. This section presents an analysis of the comparison between the coherent atom-cavity coupling and the incoherent cavity decay and spontaneous emission processes.

The cavity decay rate 2κ is a characteristic of the cavity and depends only on parameters related to it, as demonstrated later on in section 4.2. The spontaneous emission rate, however, depends on the atom species and also on the amount of population present in the excited state, which varies according to the interaction with the applied field. When this applied field is not resonantly exciting the atom, an effective spontaneous emission rate, Γ_{eff}, can be attributed to the system. For the case in which $2g\sqrt{1+\bar{n}_{\text{cav}}} \ll \Omega_d$, where $\bar{n}_{\text{cav}}$ represents the mean number of photons in the cavity mode, this effective spontaneous emission rate can be written as [75]

$$\Gamma_{\text{eff}} = 2\gamma_{\text{eff}} = 2\gamma \left(\frac{\Omega_d}{2\Delta}\right)^2, \tag{2.30}$$

where $2\gamma = 2\gamma_{PS} + 2\gamma_{PD}$.

The comparison between the ion-cavity coupling and the dissipation mechanisms of the system draws a line between different regimes of operation. When

[4] Note that this expression has an extra factor of 2 in the numerator when compared to reference [65]. This factor originates from the comparison of only full linewidths (FWHM), which is the case of Ω_d and $2g$.

$\Omega_{\text{eff}} \gg (\Gamma_{\text{eff}}, 2\kappa)$ the system is said to operate in the strong coupling regime whereas when $\Omega_{\text{eff}} \ll (\Gamma_{\text{eff}}, 2\kappa)$ the system is said to operate in the weak coupling regime [10]. In usual quantum optics experiments, the goal is to explore coherent effects in atom-cavity coupling and thus the strong coupling regime is aimed for.

When comparing equations 2.29 and 2.30, the ratio between the coherent and incoherent processes $\Omega_{\text{eff}}/\Gamma_{\text{eff}}$ is directly proportional to the detuning Δ of the Raman transition from the upper level $|P\rangle$. Unlike for Raman transitions with lasers, this ratio does not increase for increasing detuning if Ω_{eff} is kept constant. For a fixed value of Ω_d, however, this ratio increases and the effective spontaneous emission rate decreases at a faster pace than the effective ion-cavity coupling for larger values of Δ. Therefore, the variation of the parameter Δ allows us to tune the regime of operation at will. In practice, a limit of minimum Ω_{eff} is set by the dark count rates of the avalanche photodiodes (APDs) used to detect the cavity photons.

In the setup used in this work, it is possible to operate near the border to the strong coupling regime, as has been shown in references [65, 82]. Nonetheless, the experiments shown here operate farther from the strong coupling regime compared to earlier work to favor the number of cavity photons.

3 Detailed theoretical model of the system

This chapter is dedicated to a more realistic theoretical model of the atom-cavity system, used to simulate experimental results presented in chapters 5 and 6. More precisely, the calcium ion is described using eight atomic levels and the cavity field as being composed of two orthogonally polarized modes. The density matrix formalism is employed to approach the problem similarly to reference [75]. Most of the contents of this chapter are based on the theory developed in chapter 3 of reference [65].

The manifold $D_{3/2}$ is considered to have infinite lifetime (its actual lifetime is on the order of a second [83]), which is a valid approximation considering the microsecond timescales of the atomic and cavity dynamics. It is assumed that the recycling laser on the $D_{3/2} \leftrightarrow P_{1/2}$ is not seen by the cavity due to its perpendicular direction of propagation with respect to the cavity axis. Laser linewidths have been included by introducing appropriate collapse operators [66]. Spontaneous emission from the $P_{1/2}$ manifold to both $S_{1/2}$ and $D_{3/2}$ as well as the cavity decay are dissipation mechanisms also considered.

The motion of the ion is not described in this model, which is a valid approximation only for a strongly localized ion wavepacket, that is, $z_0 k \ll 1$, where z_0 is the size of the wavepacket of the ion in the ground state of the trap and k is the wave number of the light field. However, the fact that the ion is not perfectly cold is partially included in the simulations via the utilization of an effective ion-cavity maximum coupling rate $2g_{0\text{obs}}$, which accounts for an imperfect localization of the ion on the cavity standing wave. The negligence of the motional sidebands associated to the ion's motion in the trap is discussed in section 5.3.

3.1 Level structure of $^{40}Ca^{+}$

A simplified level scheme of the calcium ion is shown in figure 3.1. In this figure, the different transitions are indicated by arrows together with their associated wavelengths. From these wavelengths, only lasers at 397 nm, 866 nm, 854 nm and 729 nm

are used to perform the experiments exhibited in this thesis.

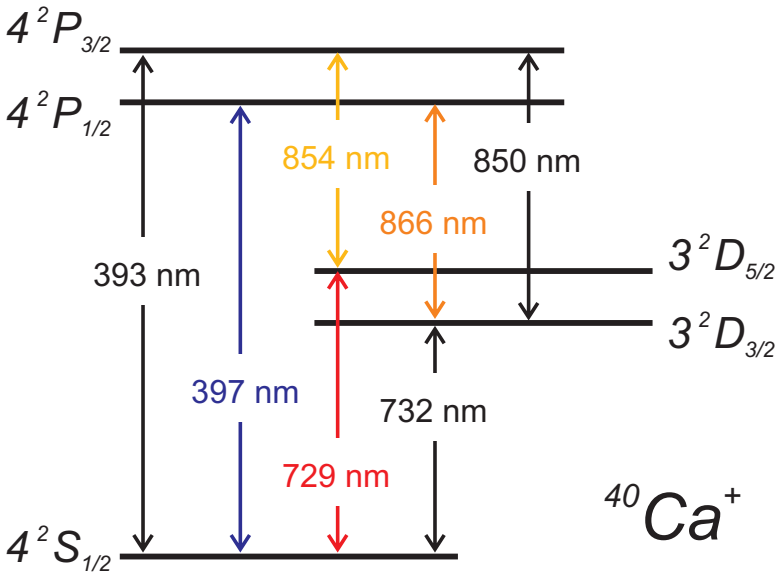

Figure 3.1: Simplified level scheme of the $^{40}Ca^{+}$ ion, including the transitions' wavelengths.

The level scheme of figure 3.1 reveals the basic structure of the calcium ion. However, a more detailed level scheme containing also the Zeeman sublevels is required for understanding the system under the circumstances of this work. Each Zeeman sublevel $|L_J, m_J\rangle$ is designated by the orbital angular momentum L, the total angular momentum J , and its projection m_J onto the quantization axis, coincident to the magnetic field direction. In the absence of a magnetic field, the Zeeman sublevels with the same orbital angular momentum are degenerate in energy. A magnetic field breaks the degeneracy of magnetic sublevels with the same angular momentum, which is the so-called Zeeman effect. The energy shift acquired by each of the $|L_J, m_J\rangle$ sublevels with respect to the zero-magnetic field line due to a static magnetic field B is given by

$$\Delta E_{L_J,m_J} = -m_J g_{L_J} \mu_B B, \tag{3.1}$$

where g_{L_J} is the Landé g-factor of the level $|L_J\rangle$ and μ_B is Bohr's magneton. The inclusion of these sublevels in our model is essential, as the presence of a static magnetic field allows us to address each of these sublevels individually.

Simulations including interactions with lasers and cavity fields are performed in the $S_{1/2}$, $P_{1/2}$ and $D_{3/2}$ manifolds. Figure 3.2 shows the relevant eight-level structure of the calcium ion with a magnetic field present.

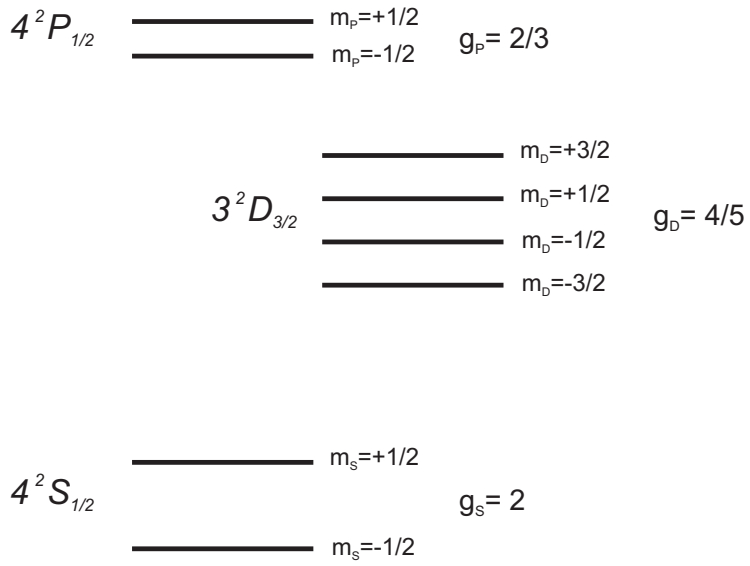

Figure 3.2: Relevant eight-level structure of the calcium ion used in the model describing the system. The Landé g-factors of each manifold are indicated.

3.2 Electric dipole transitions in the eight-level atom

In section 2.1 of the previous chapter, the dipole interaction between two- and three-level atoms with an electric field has been presented. Here, this description is expanded to an eight-level atomic system. The atomic dipole moment operator is given by [67]

$$\hat{\boldsymbol{d}} = -\sum_{L_{J_1},L_{J_2}} \sum_{m_{J_1},m_{J_2}} [(\hat{\sigma}_{L_{J_2},m_{J_2};L_{J_1},m_{J_1}} + \hat{\sigma}_{L_{J_1},m_{J_1};L_{J_2},m_{J_2}}) D_{L_{J_1},L_{J_2}}] \boldsymbol{d}^{L_{J_2},m_{J_2}}_{L_{J_1},m_{J_1}} \tag{3.2}$$

for all dipole-allowed values of L_J and m_J. The operators

$$\begin{aligned} \hat{\sigma}_{L_{J_2},m_{J_2};L_{J_1},m_{J_1}} &= |L_{J_2},m_{J_2}\rangle \langle L_{J_1},m_{J_1}| \quad \text{and} \\ \hat{\sigma}_{L_{J_1},m_{J_1};L_{J_2},m_{J_2}} &= |L_{J_1},m_{J_1}\rangle \langle L_{J_2},m_{J_2}| \end{aligned} \tag{3.3}$$

correspond to the transitions between Zeeman sublevels $|L_{J_1},m_{J_1}\rangle \rightarrow |L_{J_2},m_{J_2}\rangle$ and $|L_{J_2},m_{J_2}\rangle \rightarrow |L_{J_1},m_{J_1}\rangle$, respectively. The reduced dipole moment $D_{L_{J_1},L_{J_2}}$ is associated to transitions between two manifolds and is given by the formula 2.5 from chapter 2.

The geometric term $\boldsymbol{d}^{L_{J_2},m_{J_2}}_{L_{J_1},m_{J_1}}$ is a vector represented by:

$$\boldsymbol{d}^{L_{J_2},m_{J_2}}_{L_{J_1},m_{J_1}} = G_{L_{J_1},m_{J_1};L_{J_2},m_{J_2}} \cdot \begin{cases} \boldsymbol{u_+} & , \text{ if } m_{J_2} = m_{J_1}+1 \\ \boldsymbol{u_0} & , \text{ if } m_{J_2} = m_{J_1} \\ \boldsymbol{u_-} & , \text{ if } m_{J_2} = m_{J_1}-1 \\ 0 & , \text{ otherwise} \end{cases} . \tag{3.4}$$

The amplitude terms $G_{L_{J_1},m_{J_1};L_{J_2},m_{J_2}}$ are the Clebsch-Gordan coefficients and originate from a basis transformation [65, 68]. Table 3.1 shows the Clebsch-Gordan coefficients related to all possible dipole transitions between the manifolds $S_{1/2}$ and $P_{1/2}$, and $D_{3/2}$ and $P_{1/2}$, together with the corresponding difference in energy shift $\Delta E_{L_{J_2},L_{J_1}}$ between the two-levels involved in the transition, given by

$$\Delta E_{L_{J_2},L_{J_1}} = -(m_{J_2} g_{L_{J_2}} - m_{J_1} g_{L_{J_1}})\mu_B B. \tag{3.5}$$

The orthonormal vectors $\boldsymbol{u_\pm} = (\boldsymbol{u_x} \pm i\boldsymbol{u_y})/\sqrt{2}$ and $\boldsymbol{u_0} = \boldsymbol{u_z}$ express the direction of the dipole vector as a function of the cartesian coordinates x, y and z, respectively. The magnetic field is here assumed to point along the z-axis ($\boldsymbol{B} = B\boldsymbol{u_z}$).

Manifolds	Clebsch-Gordan coeff.	$\Delta E_{L_{J_2},L_{J_1}}/(\mu_B B)$
$S_{1/2}$ and $P_{1/2}$	$G_{S_{1/2},-1/2;P_{1/2},-1/2} = -\sqrt{\frac{1}{3}}$	$-\frac{2}{3}$
	$G_{S_{1/2},-1/2;P_{1/2},-+1/2} = -\sqrt{\frac{2}{3}}$	$-\frac{4}{3}$
	$G_{S_{1/2},+1/2;P_{1/2},-1/2} = \sqrt{\frac{2}{3}}$	$\frac{4}{3}$
	$G_{S_{1/2},+1/2;P_{1/2},+1/2} = \sqrt{\frac{1}{3}}$	$\frac{2}{3}$
$D_{3/2}$ and $P_{1/2}$	$G_{D_{3/2},-3/2;P_{1/2},-1/2} = \sqrt{\frac{1}{2}}$	$-\frac{13}{15}$
	$G_{D_{3/2},-1/2;P_{1/2},-1/2} = -\sqrt{\frac{1}{3}}$	$-\frac{1}{15}$
	$G_{D_{3/2},-1/2;P_{1/2},+1/2} = -\sqrt{\frac{1}{6}}$	$-\frac{11}{15}$
	$G_{D_{3/2},+1/2;P_{1/2},-1/2} = \sqrt{\frac{1}{6}}$	$\frac{11}{15}$
	$G_{D_{3/2},+1/2;P_{1/2},+1/2} = \sqrt{\frac{1}{3}}$	$\frac{1}{15}$
	$G_{D_{3/2},+3/2;P_{1/2},+1/2} = -\sqrt{\frac{1}{2}}$	$\frac{13}{15}$

Table 3.1: Clebsch-Gordan coefficients of the allowed dipole transitions between the manifolds $S_{1/2}$ and $P_{1/2}$, and $D_{3/2}$ and $P_{1/2}$, and difference in energy shift associated to them.

3.3 Hamiltonians of the system

This subsection introduces the bare Hamiltonians of the eight-level atom and of the two-mode cavity.

3.3.1 Bare eight-level atom Hamiltonian

All eight Zeeman sublevels, grouped in the manifolds $S_{1/2}$, $P_{1/2}$ and $D_{3/2}$, are now included in the theory. Each of these manifolds have their sublevels shifted due to the constant applied magnetic field B according to equation 3.1. The Hamiltonian of the bare ion is related to the Hamiltonian of each of these manifolds as [66]

$$\hat{\mathcal{H}}_{0a} = \hat{\mathcal{H}}_{0S} + \hat{\mathcal{H}}_{0P} + \hat{\mathcal{H}}_{0D}. \tag{3.6}$$

Following similar steps performed in chapter 2 and considering the manifold $P_{1/2}$ at no magnetic field as the zero of energy, each of these Hamiltonians can be written in the interaction picture as:

$$\hat{\mathcal{H}}_{0S} = \sum_{m_S=-1/2}^{1/2} \hbar(\Delta_d + m_S g_S \mu_B B)\hat{\sigma}_{S,m_S;S,m_S}, \tag{3.7}$$

$$\hat{\mathcal{H}}_{0P} = \sum_{m_P=-1/2}^{1/2} \hbar m_P g_P \mu_B B \hat{\sigma}_{P,m_P;P,m_P} \quad \text{and} \tag{3.8}$$

$$\hat{\mathcal{H}}_{0D} = \sum_{m_D=-3/2}^{3/2} \hbar(\Delta_r + m_D g_D \mu_B B)\hat{\sigma}_{D,m_D;D,m_D}. \tag{3.9}$$

The terms proportional to $\Delta_d = (E_S - E_P)/\hbar - \omega_d$ and $\Delta_r = (E_D - E_P)/\hbar - \omega_r$ appear due to the transformation to the interaction picture [65].

3.3.2 Bare cavity Hamiltonian

The cavity field is considered to have two orthogonal modes, designated here by the subscripts 1 and 2. The bare cavity Hamiltonian is then given by

$$\hat{\mathcal{H}}_{0\text{cav}} = \hbar(\Delta_c - \Delta_r)(\hat{a}_1^\dagger \hat{a}_1 + \hat{a}_2^\dagger \hat{a}_2), \tag{3.10}$$

where $\Delta_c = [(E_D - E_P)/\hbar] - \omega_c$ and $\hat{a}_n^\dagger$ and $\hat{a}_n$ are the creation and annihilation operators of the nth cavity mode, respectively.

3.3.3 Cavity-ion interaction

As mentioned in section 2.1 of chapter 2, the dipole approximation is used to describe the interaction between atom and electric fields. Considering the possible dipole transitions $\left|D_{3/2}, m_D\right\rangle \leftrightarrow \left|P_{1/2}, m_P\right\rangle$ through which the cavity field and the ion interact and generalizing the treatment developed in the previous chapter, the interaction Hamiltonian between the cavity field n and the ion at the position $\boldsymbol{r_0}$ near the cavity center is given by

$$\begin{aligned}\hat{\mathcal{H}}_{\mathrm{Icav},n} &= \hbar g \sum_{m_D=-3/2}^{3/2} \sum_{m_P=m_D-1}^{m_D+1} \boldsymbol{\epsilon_n} \cdot \boldsymbol{d}_{D_{3/2},m_D}^{P_{1/2},m_P} \\ &\cdot(\hat{\sigma}_{P_{1/2},m_P;D_{3/2},m_D}\hat{a}^\dagger e^{i\omega t} + \hat{\sigma}_{D_{3/2},m_D;P_{1/2},m_P}\hat{a}e^{-i\omega t}).\end{aligned} \tag{3.11}$$

The coupling rate $2g$ (full linewidth) describing the interaction between ion and cavity field is given by equation 2.11 of chapter 2. The inner product $\boldsymbol{\epsilon_n} \cdot \boldsymbol{d}_{D_{3/2},m_D}^{P_{1/2},m_P}$ can be written as

$$\boldsymbol{\epsilon_n} \cdot \boldsymbol{d}_{D_{3/2},m_D}^{P_{1/2},m_P} = G_{L_{J_1},m_{J_1};L_{J_2},m_{J_2}} \cos\alpha, \tag{3.12}$$

where α is the angle between the dipole vector and the vector indicating the polarization of the cavity electric field.

Taking into account the two orthogonal cavity modes (as in subsection 3.3 designated by the subscripts 1 and 2), the interaction Hamiltonian between the cavity field and the ion is given by

$$\hat{\mathcal{H}}_{\mathrm{Icav}} = \hat{\mathcal{H}}_{\mathrm{Icav},1} + \hat{\mathcal{H}}_{\mathrm{Icav},2}. \tag{3.13}$$

3.3.4 Laser-ion interaction

Generalizing the treatment developed in chapter 2 and considering all allowed dipole transitions between the manifolds $|L_{J_1}, m_{J_1}\rangle$ and $|L_{J_2}, m_{J_2}\rangle$, the Hamiltonian of interaction between the laser field and the ion can be written as

$$\begin{aligned}\hat{\mathcal{H}}_{\mathrm{Ilaser}} &= \frac{\hbar\Omega_{\mathrm{laser}}}{2} \sum_{m_{J_1}=-j_1}^{j_1} \sum_{m_{J_2}=m_{J_1}-1}^{m_{J_1}+1} \boldsymbol{\epsilon} \cdot \boldsymbol{d}_{L_{J_1},m_{J_1}}^{L_{J_2},m_{J_2}} \\ &\cdot(\hat{\sigma}_{L_{J_2},m_{J_2};L_{J_1},m_{J_1}} e^{-i\omega t} + \hat{\sigma}_{L_{J_1},m_{J_1};L_{J_2},m_{J_2}} e^{i\omega t}).\end{aligned} \tag{3.14}$$

The Rabi frequency Ω_{laser} is given by equation 2.18 of the previous chapter. This general expression is used for describing the influence of the drive and recycling lasers, applied between the manifolds $S_{1/2}$ and $P_{1/2}$, and $P_{1/2}$ and $D_{3/2}$, respectively. Similarly to the previous section, the term $\boldsymbol{\epsilon_n} \cdot \boldsymbol{d}^{P_{1/2},m_P}_{D_{3/2},m_D}$ reads

$$\boldsymbol{\epsilon_n} \cdot \boldsymbol{d}^{P_{1/2},m_P}_{D_{3/2},m_D} = G_{L_{J_1},m_{J_1};L_{J_2},m_{J_2}} \cos\beta, \tag{3.15}$$

where β is the angle between the dipole vector and the polarization vector of the laser field.

3.3.5 Overall Hamiltonian of the system

Following the same path presented in chapter 2, the final Hamiltonian describing the system can be written as a sum of all the bare and interaction Hamiltonians presented in this section:

$$\hat{\mathcal{H}} = \hat{\mathcal{H}}_{0S} + \hat{\mathcal{H}}_{0P} + \hat{\mathcal{H}}_{0D} + \hat{\mathcal{H}}_{\text{Icav},1} + \hat{\mathcal{H}}_{\text{Icav},2} + \hat{\mathcal{H}}_{Id} + \hat{\mathcal{H}}_{Ir}. \tag{3.16}$$

3.4 Dissipation

In section 2.3 of the previous chapter, dissipation mechanisms have been included in the theoretical description of the system by introducing a dissipative Liouvillian $\mathcal{L}_{diss}(\hat{\rho})$ in the master equation. The collapse operators composing this Liouvillian are provided in the next subsections.

3.4.1 Spontaneous emission

The collapse operators representing the spontaneous emission are divided according to the polarization of the emitted photon, which can be circular ($\sigma^{\pm}$, represented by the unitary vector $\boldsymbol{\epsilon}_{\pm}$) or linear ($\pi$, represented by the unitary vector $\boldsymbol{\epsilon_0}$), as follows:

$$C^{\pm}_{spont} = \sum \sqrt{2\gamma_{L_{J_1},L_{J_2}}(\boldsymbol{\epsilon}_{\pm} \cdot \boldsymbol{d}^{L_{J_2},m}_{L_{J_1},m\mp1})}\hat{\sigma}_{L_{J_1},m\mp1;L_{J_2},m} \quad \text{(circ. pol.)} \tag{3.17}$$

$$C^{0}_{spont} = \sum_{m} \sqrt{2\gamma_{L_{J_1},L_{J_2}}(\boldsymbol{\epsilon_0} \cdot \boldsymbol{d}^{L_{J_2},m}_{L_{J_1},m})}\hat{\sigma}_{L_{J_1},m;L_{J_2},m}. \quad \text{(linear pol.)} \tag{3.18}$$

3.4.2 Cavity decay

Each cavity mode n has a corresponding collapse operator representing its decay rate, which can be written as

$$C_{cav}^{n} = \sqrt{2\kappa}\hat{a}_n, \quad n = 1,\ 2. \tag{3.19}$$

3.4.3 Laser linewidths

Considering a full laser linewidth $2\delta_{\text{laser}}$, we can write the general expression for the collapse operator associated to it as

$$C_{\text{laser}} = \sum_{m_J} \sqrt{2\delta_{\text{laser}}}\hat{\sigma}_{L_J,m;L_J,m}, \tag{3.20}$$

where for the drive laser $|L_J\rangle = \left|S_{1/2}\right\rangle$ and for the recycling laser $|L_J\rangle = \left|D_{3/2}\right\rangle$.

3.5 Important numbers

Table 3.2 summarizes the important parameters (in full linewidths) used for the numerical simulations throughout this thesis.

Parameter	Numerical values
$P_{1/2} \rightarrow S_{3/2}$ spontaneous emission rate	$2\gamma_{PS} = 2\pi \times 20\,\text{MHz}$
$P_{1/2} \rightarrow D_{3/2}$ spontaneous emission rate	$2\gamma_{PD} = 2\pi \times 1.69\,\text{MHz}$
Cavity decay rate	$2\kappa = 2\pi \times 0.108\,\text{MHz}$
Ion-cavity maximum coupling rate	$2g_{0\text{max}} = 2\pi \times 3.2\,\text{MHz}$
Ion-cavity maximum effective coupling rate	$2g_{0\text{obs}} = 2\pi \times 2.8\,\text{MHz}$

Table 3.2: Important system parameters (in full linewidths) used in the simulations.

Note that this table presents two ion-cavity maximum coupling rates, $2g_{0\text{max}}$ and $2g_{0\text{obs}}$. The first coupling rate corresponds to the case in which the ion is in the motional ground state, not corresponding to the experimental situation. To partially mimic the motion of the ion, an effective maximum coupling rate $2g_{0\text{obs}}$ is introduced in the calculations, simulating the delocalization of the ion in the cavity standing wave. Further discussion on this subject can be found in subsection 5.2.2 of chapter 5.

The value of the cavity decay rate shown in table 3.2 is calculated in the next chapter, in section 4.2.

3.6 Raman transitions

As mentioned in the previous chapter, the Raman transitions considered in this work are performed by the drive laser and the cavity arranged in a lambda scheme connecting the manifolds $S_{1/2}$ and $D_{3/2}$. These vacuum-stimulated (empty cavity) Raman transitions address individual sublevels of these manifolds, which can be distinguished for sufficiently high magnetic fields, as exemplified in figure 3.3. Both drive laser and cavity are detuned, respectively, by Δ_d and Δ_c from the upper manifold $P_{1/2}$, whose sublevels are used as virtual levels. The Raman resonance occurs when these detunings coincide ($\Delta_d = \Delta_c$).

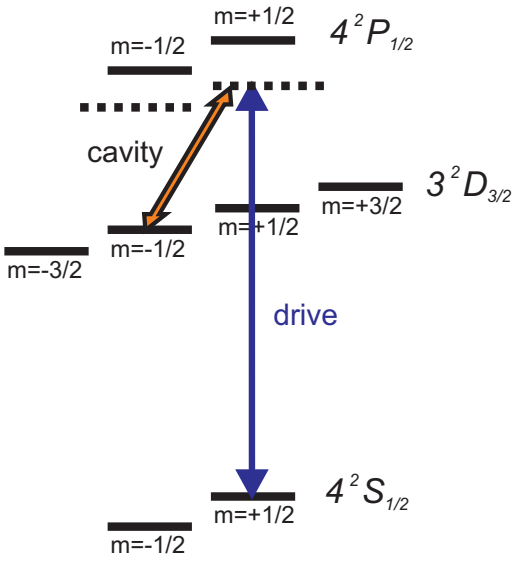

Figure 3.3: Eight-level structure of the calcium ion; a Raman transition composed of a π-polarized drive laser photon and a cavity photon originating from a $\Delta m_{PD} = -1$ transition is depicted.

The allowed Raman transitions obey the dipole transition selection rules between the initial ($\left|S_{1/2}, m_S\right\rangle$) and virtual ($\left|P_{1/2}, m_P\right\rangle$) sublevels, and the virtual and final ($\left|D_{3/2}, m_D\right\rangle$) sublevels. There exist six Raman transitions for π-polarized drive laser, divided equally between the initial sublevels $\left|S_{1/2}, m_S = +1/2\right\rangle$ and $\left|S_{1/2}, m_S = -1/2\right\rangle$, associated with particular cavity photon polarizations. Figure 3.3 shows the case of π-polarized drive laser ($\Delta m_{SP} = 0$) and a cavity photon originating from a $\Delta m_{PD} = -1$ transition. There are also three possible transitions for each of the σ polarizations of the drive laser (σ^+ originating from the $\left|S_{1/2}, m_S = -1/2\right\rangle$ and σ^- from the $\left|S_{1/2}, m_S = +1/2\right\rangle$ sublevel), again each of them creating a cavity photon with different polarization. The strength of all Raman transitions is presented in the next subsection.

3.6.1 Line strengths of the Raman transitions

The maximum line strength associated with the Raman transitions is given by the square of the product of the Clebsch-Gordan coefficients (see table 3.1) corresponding to the $|S_{1/2}, m_S\rangle \leftrightarrow |P_{1/2}, m_P\rangle$ and $|P_{1/2}, m_P\rangle \leftrightarrow |D_{3/2}, m_D\rangle$ transitions. [1]

Figure 3.4(a) shows, for the case in which the drive laser is π-polarized, the existing Raman transitions, individually labeled with letters.

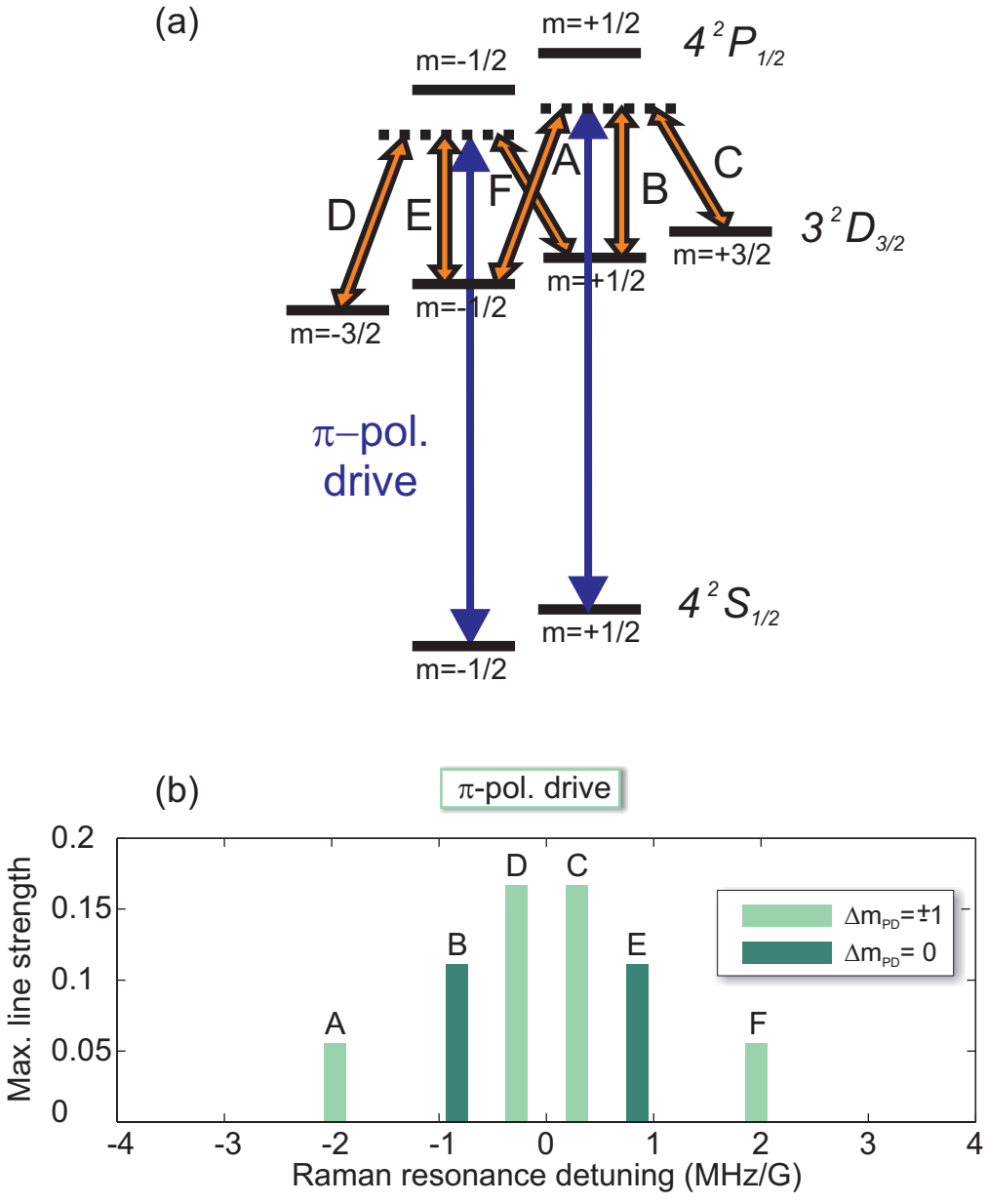

Figure 3.4: (a) Possible Raman transitions and (b) corresponding maximum transition strengths for π polarization of the drive laser.

[1] In this case, the terms $\cos\alpha$ and $\cos\beta$ of equations 3.12 and 3.15 are considered to assume the maximum value of one. The actual values of these angles are taken into account in chapter 5 for a particular geometry configuration.

Figure 3.4(b) presents the maximum line strengths of the corresponding Raman transitions as a function the detuning from the zero magnetic field line in units of MHz/G. The dark green bars (B and E) show the maximum line strengths of transitions with $\Delta m_{PD} = 0$ whereas the remaining bars (A, C, D and F) represent the maximum line strengths of $\Delta m_{PD} = \pm 1$ transitions.

The equivalent pictures for transitions with σ-polarized drive laser are shown in figure 3.5.

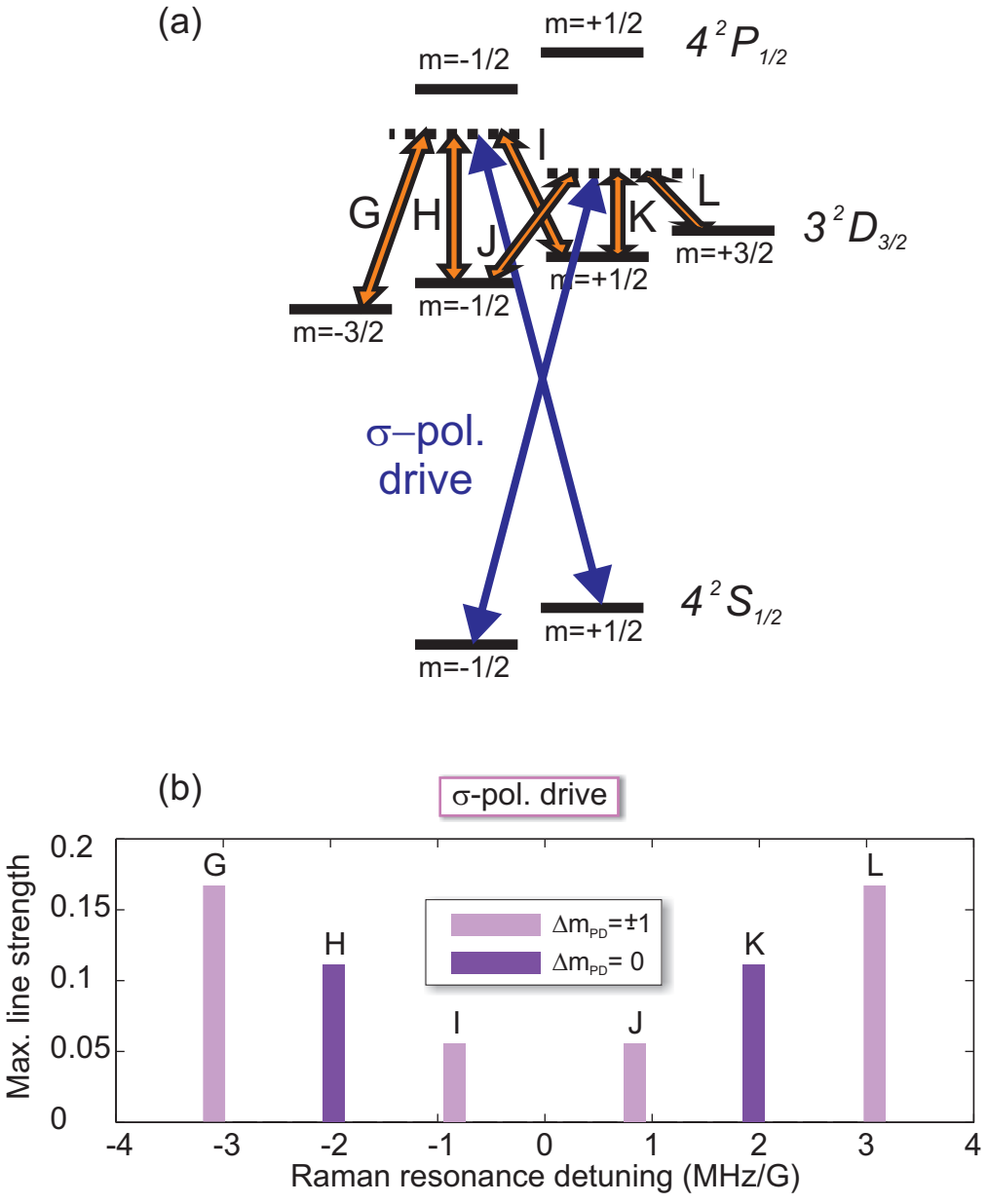

Figure 3.5: (a) Possible Raman transitions and (b) corresponding maximum transition strengths for σ^+ and σ^- drive polarizations.

In this configuration, bars H and K (dark purple) correspond to transitions

with $\Delta m_{PD} = 0$ whereas bars G, I, J and L (violet) correspond to transitions with $\Delta m_{PD} = \pm 1$. All Raman transitions are summarized in table 3.3, together with their maximum line strengths.

Line	From $\lvert S_{1/2}, m_S\rangle$	Via virtual $\lvert P_{1/2}, m_P\rangle$	To $\lvert D_{3/2}, m_D\rangle$	Δm_{SP}	Δm_{DP}	$\frac{\Delta E_{SD}}{\mu_B B}$	Max. line strength
A	+1/2	+1/2	-1/2	0	+1	-7/5	1/18
B	+1/2	+1/2	+1/2	0	0	-3/5	1/9
C	+1/2	+1/2	+3/2	0	-1	+1/5	1/6
D	-1/2	-1/2	-3/2	0	+1	-1/5	1/6
E	-1/2	-1/2	-1/2	0	0	+3/5	1/9
F	-1/2	-1/2	+1/2	0	-1	+7/5	1/18
G	+1/2	-1/2	-3/2	-1	+1	-11/5	1/3
H	+1/2	-1/2	-1/2	-1	0	-7/5	2/9
I	+1/2	-1/2	+1/2	-1	-1	-3/5	1/9
J	-1/2	+1/2	-1/2	+1	+1	+3/5	1/9
K	-1/2	+1/2	+1/2	+1	0	+7/5	2/9
L	-1/2	+1/2	+3/2	+1	-1	+11/5	1/3

Table 3.3: Spectral lines associated with the vacuum-stimulated Raman transitions. Raman resonances from $\lvert S_{1/2}\rangle$ to $\lvert D_{3/2}\rangle$ via a virtual $\lvert P_{1/2}\rangle$ state for different drive and cavity-field polarizations are considered. The initial, intermediate (virtual) and final states are indicated, as well as the photon polarizations of the absorbed drive photon (Δm_{SP}) and the emitted cavity photon (Δm_{DP}).

3.7 Simulation of measured quantities

The quantities we can measure are called observables and are represented by the operator $\hat{\mathcal{O}}$. The measured quantity is the expectation value of this observable at the measured time t given by

$$\bar{\mathcal{O}}(t) = \left\langle \hat{\mathcal{O}}(t) \right\rangle = \mathrm{Tr}[\hat{\mathcal{O}}\hat{\rho}(t)]. \tag{3.21}$$

Calculating measured quantities thus involves solving the master equation 2.25. For very long times ($t \to \infty$), we obtain the steady-state solution

$$\bar{\mathcal{O}}_{ss}(t) = \lim_{t\to\infty} \left\langle \hat{\mathcal{O}}(t) \right\rangle = \mathrm{Tr}[\hat{\mathcal{O}}\hat{\rho}_{ss}]. \tag{3.22}$$

The theoretical simulations of the experimental results are performed numerically using home-developed programs based on the Quantum Optics Toolbox package [84] for the MATLAB®programming environment. In the following, the simulation of the different observables experimentally measured in this thesis is described.

Cavity photon number

The cavity photon number is represented by the operator $\hat{n}_{\mathrm{cav}} = \hat{a}^{\dagger}\hat{a}$. The steady-state number of photons in the cavity is then given by $\bar{n}_{\mathrm{cav}_{ss}} = \mathrm{Tr}[\hat{a}^{\dagger}\hat{a}\hat{\rho}_{ss}]$. It is important to point out that throughout this thesis the simulations were performed by truncating the Fock state basis to $n = 0,\ 1,\ 2$. This is valid due to the very low intracavity photon numbers produced here.

Temporal pulse shape of the cavity photon

The temporal pulse shape of the cavity photon gives the probability of detecting a cavity photon as a function of time. As it does not represent a steady-state situation, the equations of motion are numerically integrated using the overall Liouvillian and an initial density matrix ρ_0 to obtain a solution to the master equation. The simulated temporal pulse shape is then obtained by multiplying the expectation value of the number of photons created inside the cavity, $\bar{n}_{\mathrm{cav}}(t) = \mathrm{Tr}[\hat{a}^{\dagger}\hat{a}\hat{\rho}(t)]$, by the cavity decay rate 2κ and the detection efficiency η_{det} (explained in the next chapter).

Second-order correlation function

The second-order correlation function, represented by $G^{(2)}(t,\tau)$ [85, 86], is a statistical function that correlates field intensities at time instances separated by a delay time τ. It can be written as

$$G^{(2)}(t,\tau) = \langle : \mathrm{E}^{*}(t)\mathrm{E}^{*}(t+\tau)\mathrm{E}(t+\tau)\mathrm{E}(t) : \rangle = \langle I(t)I(t+\tau)\rangle\,, \tag{3.23}$$

where the symbol : represents normal ordering, $\mathrm{E}(t)$ represents the time-varying electric field at a fixed position in space and $I(t)$ its intensity. In a continuous measurement, the normalized form of this correlation function reads

$$g^{(2)}(t,\tau) = \frac{G^{(2)}(t,\tau)}{\langle I(t)\rangle^{2}}. \tag{3.24}$$

In the simulations, the second-order correlation function is obtained by convoluting the temporal pulse shape of the cavity photons and repeating this outcome according to the photon creation repetition rate used in the experiment. The normalization is performed by dividing this outcome by the square of the sum over all cavity photon temporal pulses.

Temporal evolution of populations

The same density matrix used to simulate the cavity photon temporal shape is used here to calculate the temporal evolution of the populations of the $S_{1/2}$ and $D_{3/2}$ sublevels. The expectation value of the corresponding diagonal density matrix elements gives these populations as a function of time.

4 Experimental setup

All the experiments shown in this thesis make use of a complex setup, involving eight laser systems, a great amount of optics and electronics as well as vacuum components and computer software, among others. This chapter presents part of this apparatus and more details about it can be found in [65].

The first two sections introduce the ion trap and the high-finesse optical cavity, followed by a description of the laser and of the transfer lock systems in the third and fourth sections, respectively. Section 4.5 presents the geometry of the setup and section 4.6 lays out the detection systems. Finally, the hardware and software involved in the experimental control system are described in section 4.7.

4.1 Linear Paul trap

Consider an electrostatic harmonic potential given by $\phi = ax^2 + by^2 + cz^2$, where x, y and z represent the variables of position in three-dimensional space and a, b and c are constants. The force exerted by this potential on a particle of charge q can be written as $\overrightarrow{F} = -q\overrightarrow{\nabla}\phi = -2q(ax\hat{x} + by\hat{y} + cz\hat{z})$. In order to provide confinement in all three directions, this equation requires that a, b and c have all the same sign. Laplace's equation ($\nabla^2\phi = 0$), however, demands that $a + b + c = 0$, which leads to a saddle shaped potential in which movement in one of the directions becomes unstable. Hence, an electrostatic harmonic potential can not, alone, trap a charged particle in three dimensions.

One solution to this problem is to replace the electrostatic potential in one or more of these directions by a time-dependent fast-oscillating saddle potential, which behaves as a pseudo-potential confining the particle in the corresponding directions in a dynamic way. Based on this principle, in 1953 Wolfgang Paul has developed a two-dimensional trap for charged particles [87]. On the original design, four hyperbolic electrodes are aligned around an axis as shown in figure 4.1. In this trap, the particles are confined along a central line perpendicular to the x and y directions, at a distance of r_0 from the electrodes. Two of the electrodes are set to ground and the remaining two are provided with a radio-frequency field.

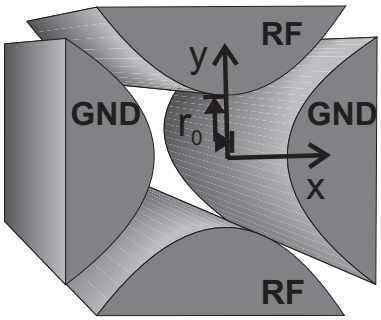

Figure 4.1: Two-dimensional Paul trap consisting of four hyperbolic electrodes, two of them connected to a radio-frequency (RF) and two of them connected to ground (GND).

The two-dimensional time-dependent trapping potential on such a quadrupole mass filter can be written as follows

$$\phi = \frac{x^2 - y^2}{2r_0^2} U(t), \tag{4.1}$$

where $U(t) = U_1 \cos(\omega_{rf} t)$ is the time dependent potential with oscillating frequency ω_{rf}. The motion of a particle of charge q when submitted to this potential can be obtained from the Lorentz force, $m\ddot{\vec{r}} = -q\vec{\nabla}\phi$, which leads to the equations of motion

$$\frac{d^2x}{dt^2} = \frac{-qU_1}{mr_o^2} \cos(\omega_{rf} t)x \tag{4.2}$$

$$\frac{d^2y}{dt^2} = \frac{qU_1}{mr_o^2} \cos(\omega_{rf} t)y \tag{4.3}$$

for the x and y directions, respectively. Making the following transformation of variables $\tau = \frac{\omega_{rf} t}{2}$ and $q' = \frac{2qU_1}{mr_0^2 \omega_{rf}^2}$ we obtain [88]

$$\frac{d^2x}{d\tau^2} + 2q' \cos(2\tau)x = 0 \tag{4.4}$$

$$\frac{d^2y}{d\tau^2} - 2q' \cos(2\tau)y = 0. \tag{4.5}$$

These second-order differential Mathieu equations have two types of solutions:

- stable: the particle oscillates in the $x - y$ plane with limited amplitude;
- unstable: the motion of the particle grows exponentially in the x, y or both directions, which leads to an escape of the particle from this two-dimensional potential.

The choice of the parameter q' will determine the stability of the particle motion on the potential. For the particular case in which $q' \ll 1$, the motion is stable and the solutions for equations 4.4 and 4.5 can be written as

$$x(t) \approx x_0 \left[1 + \frac{q'}{2}\cos(\omega_{rf} t)\right] \cos(\omega t + \varphi_x) \tag{4.6}$$

and

$$y(t) \approx y_0 \left[1 - \frac{q'}{2}\cos(\omega_{rf} t)\right] \cos(\omega t + \varphi_y). \tag{4.7}$$

where $\omega = \sqrt{\frac{q'}{m}}$.

In these solutions two different types of motion can be identified, characterized by the motional frequencies ω_{rf} and ω. The micromotion is the fastest of the two and drives the particle at the frequency ω_{rf} of the radio-frequency field applied to the trap electrodes. The secular motion is slower and makes the particle oscillate around the trap center at a frequency given by ω. For further details on trapping charged particles see [88–91].

Based on this quadrupole mass filter from Wolfgang Paul, the Linear Paul trap was invented. It consists of a three-dimensional version of this original idea where a quadrupole field is used to confine the particle in two of the three dimensions and an electrostatic field is used in the remaining direction. In our experiment, we use a special design of a linear Paul trap developed in our group [92, 93] to confine a single $^{40}Ca^{+}$ ion. A picture of our trap can be seen in figure 4.2.

Our trap consists of four blades, two opposite to each other are kept at ground and to the other two we apply a radio-frequency field at 23.44 MHz with a power of approximately 5 W. These four blades are responsible for the radial confinement of the ion. For the axial confinement, two tip electrodes are used, to which we apply about 950 V each. These trapping parameters yields motional frequencies of approximately 1.1 MHz in the axial direction and 2.9 MHz in the radial direction. The two radial modes of motion are not perfectly degenerate but rather differ by approximately 60 kHz (experimental evidence is shown in chapter 7, figure 7.4). Additionally to these six elements, two pairs of micromotion compensation electrodes are included in the setup in order to optimize the minima position of both axial and radial confining potentials and thus reduce the micromotion on the ion. These electrodes are visible in figure 4.2.

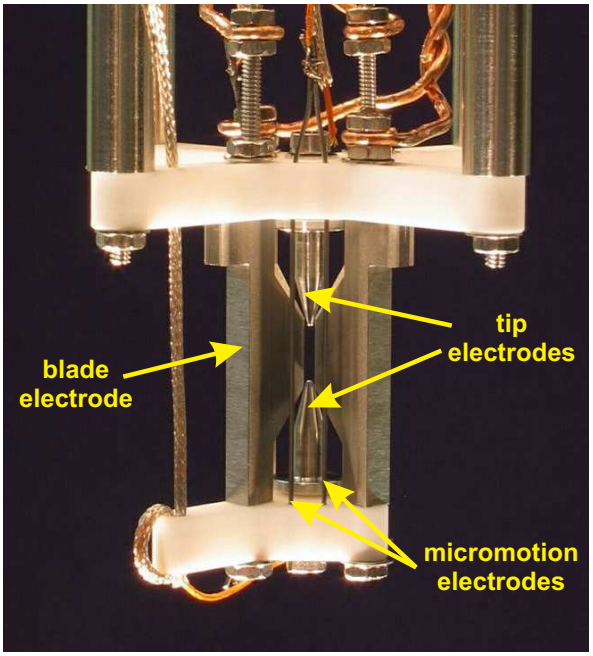

Figure 4.2: Linear Paul trap used in our experiment. Here, two of the four blade electrodes are visible as well as one of the two pairs of micromotion compensation electrodes and both tip electrodes.

4.2 High-finesse optical cavity

When designing a high-finesse optical cavity, details like geometry, mirror specifications and tunability have to be carefully considered in order to achieve the aimed regime of operation. The history of the design and construction of the high-finesse cavity used in the experiments of this thesis as well as its characterization is carefully detailed in the work of Carlos Russo [65]. Here, its main characteristics are presented and also some of the important parameters to be considered are reviewed.

Our high-finesse optical cavity is approximately 19.92 mm long and was built in a near-concentric configuration, that is, the cavity length is approximately equal to the sum of the mirrors' focal lengths. The cavity was designed to operate in an intermediary coupling regime in which the atom-cavity field maximum coupling rate, $2g_0$, depends on the cavity length L and on the cavity field mode waist w_0 according to the formula

$$g_0 = \sqrt{\frac{3c\lambda^2\gamma_{PD}}{\pi^2 L w_0^2}} \tag{4.8}$$

derived in chapter 2 (equation 2.12). Just as a reminder, $2\gamma_{PD}$ is the atom decay rate on the transition $P_{1/2} \leftrightarrow D_{3/2}$ in which the cavity operates ($2\gamma_{PD} = 2\pi \times 1.69$ MHz in table 3.2) and λ is the cavity operating wavelength (866.215 nm). Expression 4.8 indicates that a smaller mode waist and a shorter cavity length contribute to a

higher atom-cavity coupling. Having a TEM_{00} mode waist of 13.4 μm, the maximum coupling rate achieved in our work is $2g_{0max} = 2\pi \times 3.2\,\text{MHz}$ (see table 3.2).

The cavity finesse at this operating wavelength is measured to be 70 000 and is defined as the free spectral range ($\nu_{FSR} = c/2L$) divided by the FWHM of the resonance peak ($\delta\omega$), as shown in the following formula

$$\mathcal{F} = \frac{\nu_{FSR}}{\delta\omega}. \tag{4.9}$$

The finesse of a cavity also reflects the quality of the mirrors (see reference [70]) as it can be written as a function of the mirrors' transmission coefficients ($\Im_1$ and $\Im_2$) and the overall losses ($\mathfrak{L}$) as follows (for the case of high reflectivity mirrors)

$$\mathcal{F} \approx \frac{2\pi}{\Im_1 + \Im_2 + \mathfrak{L}}. \tag{4.10}$$

The cavity decay rate, 2κ, is related to the finesse and to the cavity length by

$$2\kappa = \frac{\pi c}{\mathcal{F} L}. \tag{4.11}$$

Substituting the parameters on the formula above we obtain a cavity decay rate of $2\kappa = 2\pi \times 108\,\text{kHz}$, which leads to a cavity decay time, $\tau_c = 1/(2\kappa) = 1.5\,\mu\text{s}$.

The parameters mentioned in this section as well as the mirrors' characteristics are summarized in table 4.1 (information obtained from [65]). It is important to emphasize that these parameters were all measured with 866.215 nm light. Information about 854.209 nm light can be found in [65].

Parameter	**Value**
Cavity length	$L = (19.9159 \pm 0.0005)\,\text{mm}$
Mode waist (TEM_{00})	$w_0 = (13.4 \pm 0.2)\,\mu\text{m}$
Finesse	$\mathcal{F} = 70\,000 \pm 1\,000$
Transmission coeff. of input mirror	$\Im_1 = (1.9 \pm 0.4)\,\text{ppm}$
Transmission coeff. of output mirror	$\Im_2 = (17 \pm 3)\,\text{ppm}$
Total internal losses	$\mathfrak{L} = (71 \pm 3)\,\text{ppm}$

Table 4.1: List of the relevant cavity characteristics, measured with light at 866.215 nm.

As can be seen in table 4.1, the mirrors' reflectivities are not equal, which leads to a preferred output channel for the cavity photons. Each of these mirrors sits on a piezo stage, one of them being of fast but short range (called here fast piezo) and the other one of slower but longer range (called here slow piezo). The first is used

as feedback element of the Pound-Drever-Hall lock of the cavity length (see section 4.4). The latter can either be used to change the distance between the two mirrors (for example when scanning through cavity modes) or to move the cavity around the ion once its length is locked (for instance when mapping the standing wave of the light field inside the cavity).

These mirrors are mounted in a U-shaped metallic piece that then sits on a stack of piezo electric stages. This piezo stack is remotely controlled and moves the whole cavity assembly by millimeters horizontally (in the laboratory reference frame), perpendicularly and parallel to the cavity axis (x and y directions in figures 4.5.1 and 4.5.2).

Additionally, three micrometer screws located underneath the vacuum chamber and reachable by feedthroughs from the outside can be used for the vertical and tilt alignments of this U-shaped piece. This way, the cavity can be carefully positioned around the ion and the coupling between the two can be optimized. Figure 4.3 shows a picture of the trap-cavity setup, where this U-shaped mount is visible, as well as some pieces that form the cavity and the trap. In this picture two lenses located at the input and output of the cavity can be seen, placed there for collimation of light entering and exiting the cavity.

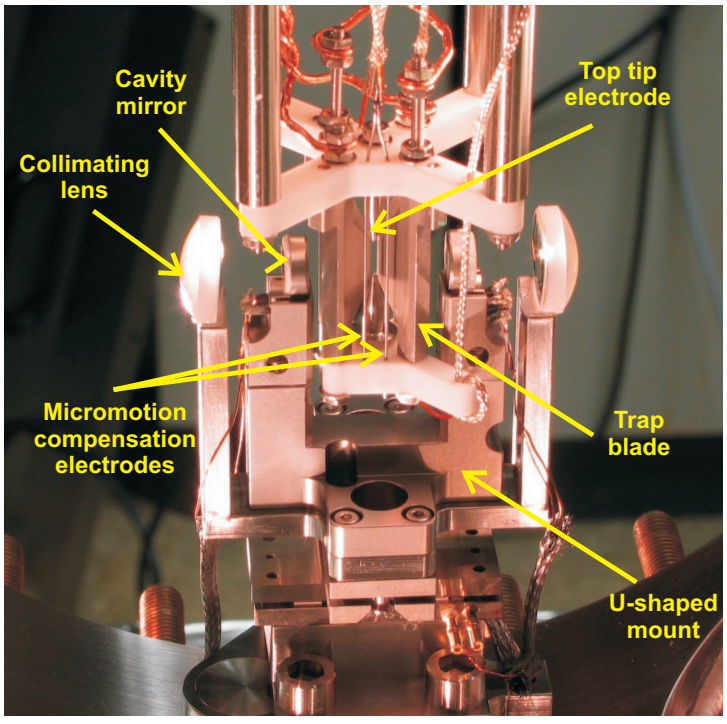

Figure 4.3: Setup of linear Paul trap plus high-finesse cavity used in our experiment. The cavity mirrors as well as the collimating lenses and the U-shaped mount can be seen.

4.3 Lasers

In this section, the laser systems used in our experiments are described. Except for the photoionization lasers, all laser systems have their frequencies stabilized to an external cavity using the Pound-Drever-Hall technique [94–97]. Also, all but the 375 nm photoionization laser have their wavelengths monitored by WS-/7 wavelength meter from Toptica.

4.3.1 Photoionization of calcium

The neutral calcium atoms are provided by an oven located below the input cavity mirror and whose output points towards the center of the trap at a 45° angle with both trap and cavity axis in the plane containing both axes (direction $\mathbf{v} = (x = 1, y = 0, z = 1)$ in figure 4.11). In order to ionize these atoms, two photoionization lasers (Toptica DL-100 series) at 422 nm and 375 nm are directed to the middle of the trap from above the cavity, perpendicular to the direction of propagation of the atomic beam (direction $\mathbf{v} = (0, -1, -1)$ in figure 4.11). The first of these lasers resonantly excites the outer shell electron to the high energy state $4p^1P_1$. The second laser extracts the electron from the neutral atom. The typical oven current used to load one ion is around 4.75 A and this process takes about 15 minutes, limited by the thermalization time of the oven.

4.3.2 Doppler cooling, detection and optical pumping laser at 397 nm

This laser excites the calcium ion from the $S_{1/2}$ to the $P_{1/2}$ manifolds and is responsible for Doppler cooling [98, 99], detection and optical pumping. The 397 nm light comes from a frequency doubled 794 nm Ti:Sapphire laser (Coherent CR-899-21), which is pumped by a Verdi V10 (532 nm), also from Coherent. The frequency doubler Wavetrain (Spectra Physics LAS) employs an LBO crystal to convert 794 nm light into 397 nm light. The 794 nm laser has its frequency stabilized to a reference cavity using home-built electronics, achieving a linewidth of around 300 kHz.

The laser light after the doubler is divided into two paths leading to the experiment, one is used for Doppler cooling and detection and the other for optical pumping. The path of the corresponding beams are depicted in figure 4.4, which sketches both laser and experiment table setups.

In the current setup, the laser frequency of both beams can be tuned simultaneously by the use of a double-pass acousto-optical modulator (AOM) operating on

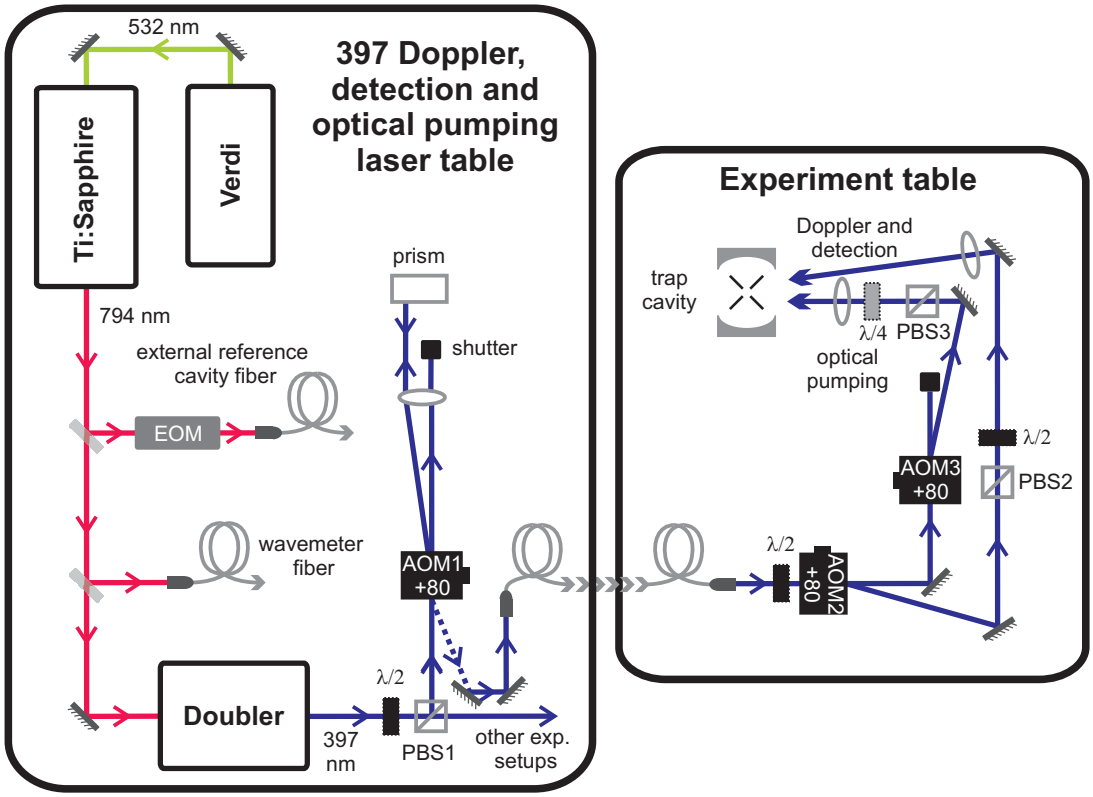

Figure 4.4: Schematic drawing of the 397 Doppler, detection and optical pumping laser setup. Details of this setup are explained in the text of subsection 4.3.2.

the laser table (AOM1) at the central frequency of +80 MHz, driven by home-made radio-frequency driver and amplifier. The double-pass light exiting the fiber on the experimental table is about 80 MHz red detuned from the $S_{1/2} \leftrightarrow P_{1/2}$ transition and the typical power at this point is approximately 1 mW.

When the AOM1 is turned off, the zero-order light coming from it can be sent through the fiber (the shutter has to be set accordingly) to perform far-detuned cooling of the ion during the loading process. The two beams are separated at AOM2 placed after the output of this optical fiber. The +1-order beam of this single-pass AOM constitutes the cooling and detection beam, which, from below, crosses the vacuum chamber through the $\mathbf{v} = (0, 1, 1)$ direction in figure 4.11. This beam has two separate RF power levels that can be alternated in pulse sequences to provide either Doppler cooling (lower power setting) or ion detection (higher power setting).

The optical pumping beam is formed by the zero-order of AOM2, which is directed to another +80 MHz single-pass AOM (AOM3) and traverses the setup through the $\mathbf{v} = (0, 1, -1)$ direction on figure 4.12, coming from above. The po-

larization of this beam is chosen to be σ^+ and its role is therefore to eliminate population from the state $|S_{1/2}, -1/2\rangle$, as shown in the level scheme of figure 4.5. This beam is only applied in the experiments of chapters 6 and 7 and in these cases the magnetic field direction has been changed to match this beam's direction, according to the geometric configuration 2 described in subsection 4.5.2.

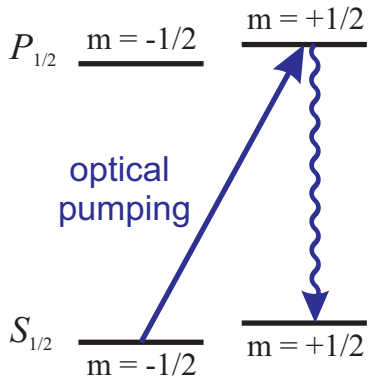

Figure 4.5: Level scheme displaying the role of the optical pumping.

4.3.3 Recycling lasers at 866 nm and 854 nm

Recycling laser on the $D_{3/2} \leftrightarrow P_{1/2}$ transition

The recycling laser at 866 nm operates on the $D_{3/2} \leftrightarrow P_{1/2}$ transition of the $^{40}Ca^+$ ion (see level scheme of figure 3.1) and is present in all of our experiments. Its main task in this work is to recycle the atomic population from the metastable $D_{3/2}$ manifold to the $P_{1/2}$ manifold. This beam is aligned along the direction $\mathbf{v} = (0, -1, 1)$ (see figure 4.11), originating from below.

A secondary beam of this laser is set to be 320 MHz red detuned from resonance with the $D_{3/2} \rightarrow P_{1/2}$ transition and works as reference to roughly adjust the cavity length to the Raman transition. This Raman transition reference beam is sent through the cavity in the direction $\mathbf{v} = (1, 0, 0)$ from the cavity incoupling side. It is only used in the stage where we are locking the cavity length and searching for the correct 866 nm cavity mode (see subsection 4.4).

The 866 nm laser light originates from a Toptica diode laser (model DL-100), stabilized to a cavity with a linewidth of around 150 kHz. The schematic setup of this laser is shown together with the setup of the 854 nm recycling laser in figure 4.6.

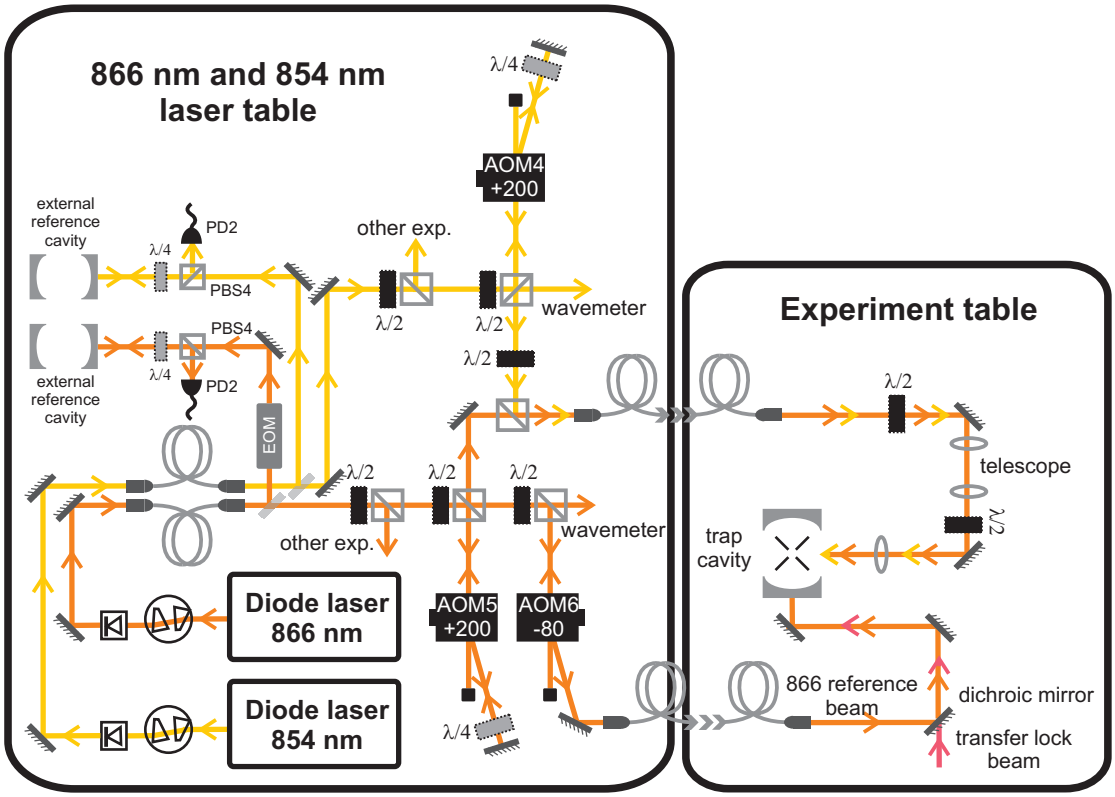

Figure 4.6: Schematic drawing of the 866 and 854 laser setups. Both 866 reference beam as well as the recycling beam are sketched here. Details of this setup are described in the text of subsection 4.3.3.

Recycling laser on the $D_{5/2} \leftrightarrow P_{3/2}$ transition

The recycling laser at 854 nm addresses the transition from the $D_{5/2}$ to the $P_{3/2}$ manifolds. Its unique purpose in this thesis is to prevent population from being trapped in the metastable $D_{5/2}$ manifold. It is a Toptica DL-100 diode laser and it is stabilized to an external cavity, reaching a linewidth of a few hundreds of kHz. This laser beam is overlapped with the 866 nm recycling laser and is carried to the experiment table through the same optical fiber, as shown in the schematic drawing of figure 4.6. Its use becomes necessary once the 729 nm laser is present, in chapter 7.

4.3.4 Quadrupole transition laser (729 nm)

The $S_{1/2} \leftrightarrow D_{5/2}$ quadrupole transition is addressed by a Verdi-pumped (also V10 from Coherent) Ti:Sapphire laser (CR-899-21 from Coherent) working at 729 nm. The frequency of this laser is stabilized to an external resonator to achieve a linewidth of a few Hz (details described in reference [97]).

The light exiting the Ti:Sapphire laser passes through an AOM working at -80 MHz (AOM7) which is used as feedback for intensity stabilization. Seed light of about 10 mW is sent from the Ti:Sapphire laser to a tapered amplifier (TA100 from Toptica), which in turn provides circa 500 mW (at 1.5 A operating current). This output light is divided between two experimental setups and sent through a single-pass AOM +80 MHz (AOM8) and a double-pass +270 MHz AOMs (AOM9) so that each experiment has individual control of the laser frequency. The beam path can be seen in the schematic drawing of figure 4.7.

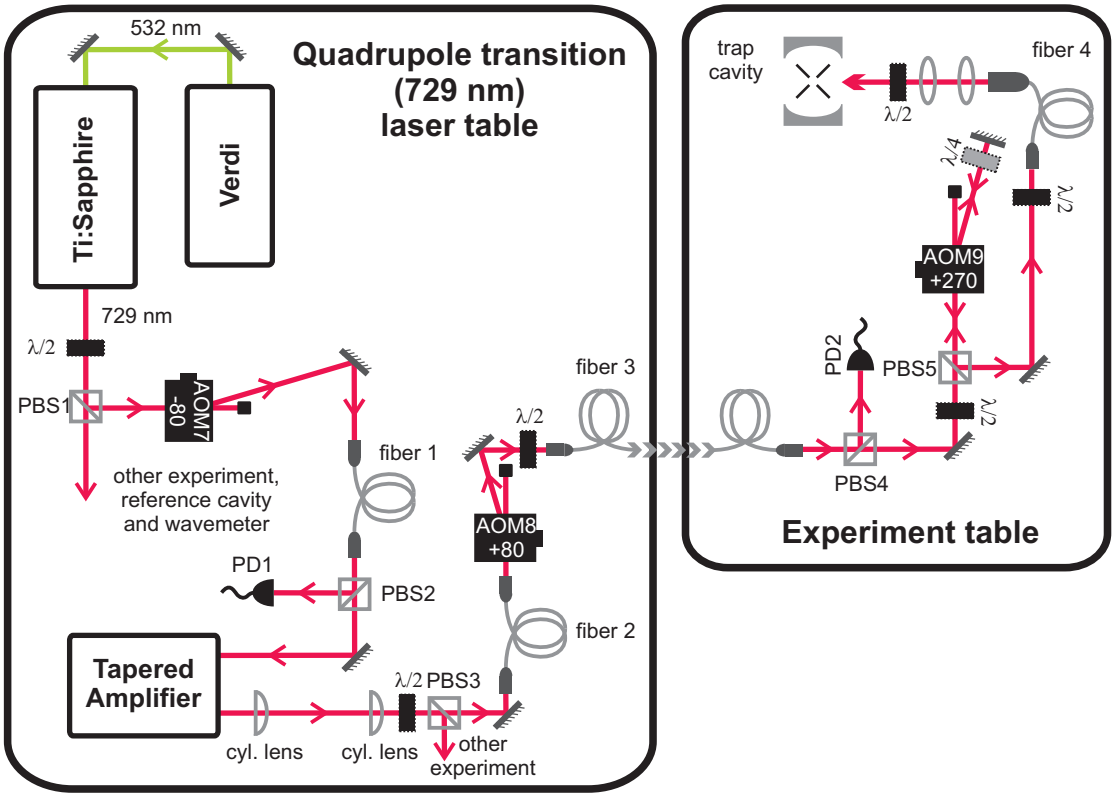

Figure 4.7: Schematic drawing of the quadrupole (729 nm) laser setup. Details of this setup are described in the text of subsection 4.3.4.

At the output of the fiber (fiber 3) we can achieve approximately 10 mW of 729 nm light going to the ion. This beam is focused down using a fiber collimator (Schaefter und Kirchhoff, 60FC-T-4-M75-37) and two lenses (of focal lengths 300 mm and 500 mm), reaching at the ion a waist on the order of 200 µm for most experiments. It comes from above and traverses the vacuum chamber in the $\mathbf{v} = (-1, 0, -1)$ direction.

Two intensity stabilization schemes are installed for this laser. The first, composed of a polarizing beam splitter (PBS1), a photodiode (PD1) and a Stanford Research PID controller, ensures that the amount of light entering the tapered am-

plifier does not exceed its maximum allowed value. The second, composed of the polarizing beam splitter PBS4, the photodiode PD2 and home-built sample-and-hold intensity stabilization electronics, stabilizes the light intensity at the experiment table, reducing the intensity fluctuations to around 1 %.

Short-term stability of the laser is provided by the lock to the reference cavity. For long-term stability, the laser can be stabilized to the ion by the use of special pulse sequences involving Ramsey experiments. More details on this long-term lock can be found in sections 7.3 and 7.4.

4.3.5 Raman transition laser (397 nm)

This laser's wavelength is also 397 nm but it performs a different task as the one mentioned in subsection 4.3.2: it is used for driving the Raman transition together with the cavity. The major advantage of this laser when compared to the previously mentioned one is its narrow linewidth of around 30 kHz, which improves the Raman transition efficiency, discussed in chapter 6 of this thesis.

The laser light at 397 nm originates from a frequency doubled 794 nm Coherent 899-21 Ti:Sapphire ring laser pumped by a Coherent Verdi V10. The different frequency lock stages performed in the 794 nm Ti:Sapphire laser are depicted in figure 4.8.

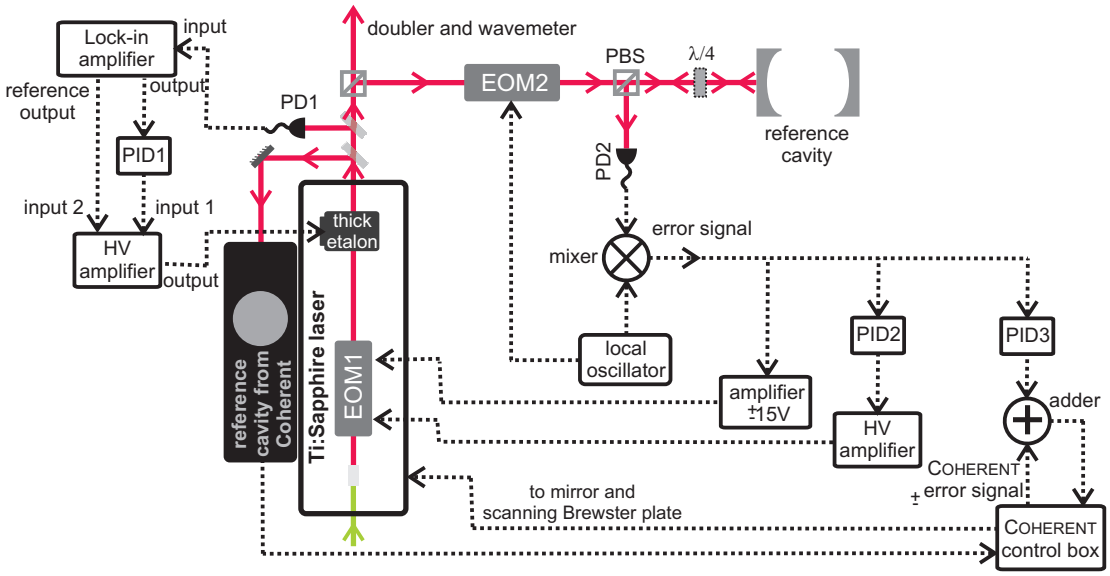

Figure 4.8: Schematic drawing of the Raman laser lock. Details of this setup are described in the text of subsection 4.3.5.

For the first lock stage, which uses the thick etalon inside the laser cavity, the Coherent control box was bypassed and an external modulation of the light

amplitude at 2 kHz was created using a lock-in amplifier. A photodiode (PD1) detects part of the laser light and its signal is input to the same lock-in amplifier, which creates an error signal. This error signal is sent to a home-built PID circuit (PID1 in figure 4.8) and, after passing through a home-built high-voltage amplifier, is fed back to the thick etalon.

The second lock stage consists of an internal Coherent lock to its own reference cavity. It feeds back to a piezo-mounted mirror (tweeter) and a scanning Brewster plate located inside the T:Sapphire laser cavity.

Another error signal, now generated by coupling the laser light into an external high-finesse reference cavity [100], is used for the additional frequency lock stages of this Ti:Sapphire laser. The first branch of this error signal goes into a SRS digital PID box (PID3) whose output is added to the internal Coherent lock setup to drive some of the laser intracavity elements.

A narrow linewidth is achieved through an intracavity electro-optical modulator (EOM1 in figure 4.8), which suppresses high-frequency phase noise on the laser. A home-built PID controller (PID2) followed by a home-built high-voltage amplifier receives part of the external cavity error signal and its output goes to one of this EOM's electrodes, providing a large-amplitude (±400 V) medium-speed feedback to the laser. The second EOM electrode receives a signal coming from a fast high-voltage amplifier (HVA-10M-60-B amplifier from FEMTO), whose input is also the external cavity error signal. This last branch provides a fast short-range (±15 V) feedback to the frequency lock of the Ti:Sapphire laser.

An MBD 200 frequency doubler from Coherent converts the light to 397 nm and when optimized can operate at a doubling efficiency of 12 % (60 mW output for 500 mW input). The light generated by the doubler is divided in two beams, one of which is red detuned by around 320 MHz from resonance with the $S_{1/2} \leftrightarrow P_{1/2}$ transition and is used for driving the Raman transition. The second beam is set to be resonant with this transition and is only used for calibration purposes, as mentioned in section 5.1. A sketch of these beams paths is shown in figure 4.9.

The frequency tuning of both beams is realized by the use of two double-pass AOMs, one working at +80 MHz (AOM12, constitutes the resonant calibration beam) and at -80 MHz (AOM13, constitutes the Raman drive beam). These AOMs are controlled using an RF output from a pulse sequencer hardware (described in section 4.7). These two beams have orthogonal linear polarizations and are overlapped in a polarizing beam splitter (PBS6) and then sent through a polarization-maintaining single-mode optical fiber to the experiment. At the output of this fiber, a $\lambda/2$ waveplate and a polarizing beam splitter (PBS7) select one of the two beams

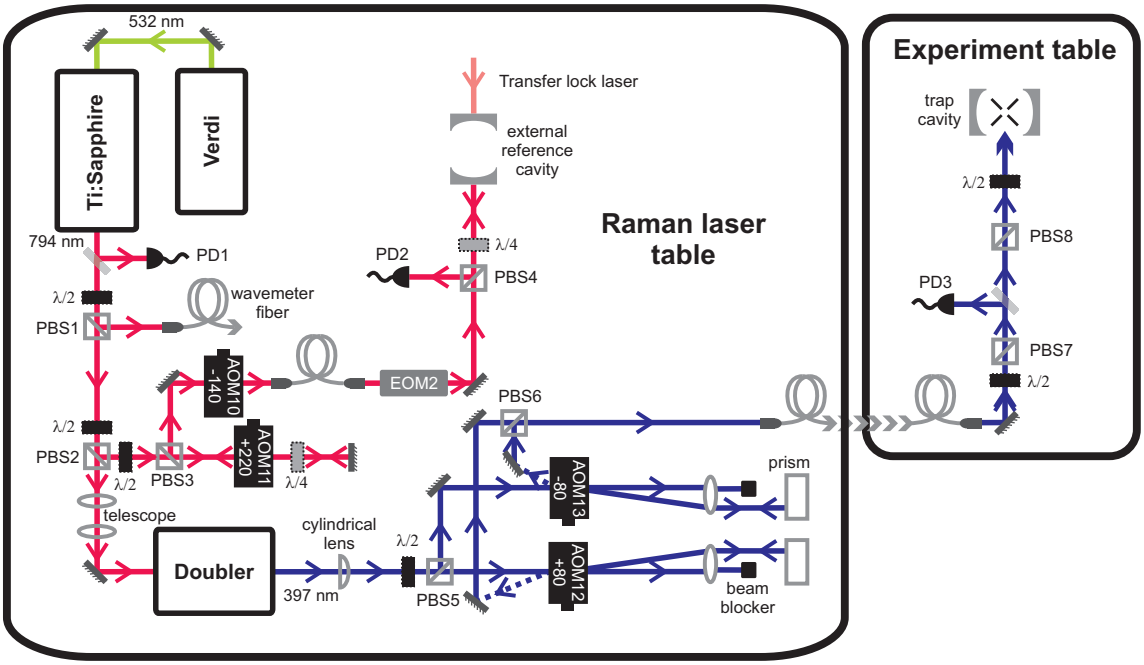

Figure 4.9: Schematic drawing of the 397 nm Raman laser setup. Details of this setup are described in the text of subsection 4.3.5.

needed in the current experiment. After that, another pair of beam splitter (PBS8) and $\lambda/2$ waveplate is used to adjust the polarization of the chosen beam going to the ion. The beam originates from below and crosses the chamber in the $\mathbf{v} = (-1, 0, 1)$ direction.

4.4 Transfer lock

The cavity length stabilization is realized by the use of a transfer lock laser at around 785 nm. It is a Toptica DL-100 diode laser and has a Toptica PID control (PID 110). Additionally to this Toptica PID locking stage, we also use a home-made PID box to improve the lock stability. The error signal used here is generated using the same external cavity used for the Raman transition laser, to which both lasers can be locked simultaneously coming from opposite sides and with orthogonal polarizations without disturbing each other significantly.

The transfer lock of the trap cavity is described in [65] and a schematic drawing of the laser path is shown in figure 4.10. In brief, 785 nm frequency stabilized laser light is coupled to the high-finesse cavity. A Pound-Drever-Hall error signal is generated from its reflection off the incoupling cavity mirror and fed back to the fast piezo sitting under one of the cavity mirrors. This lock stage is also performed using home-built PID electronics.

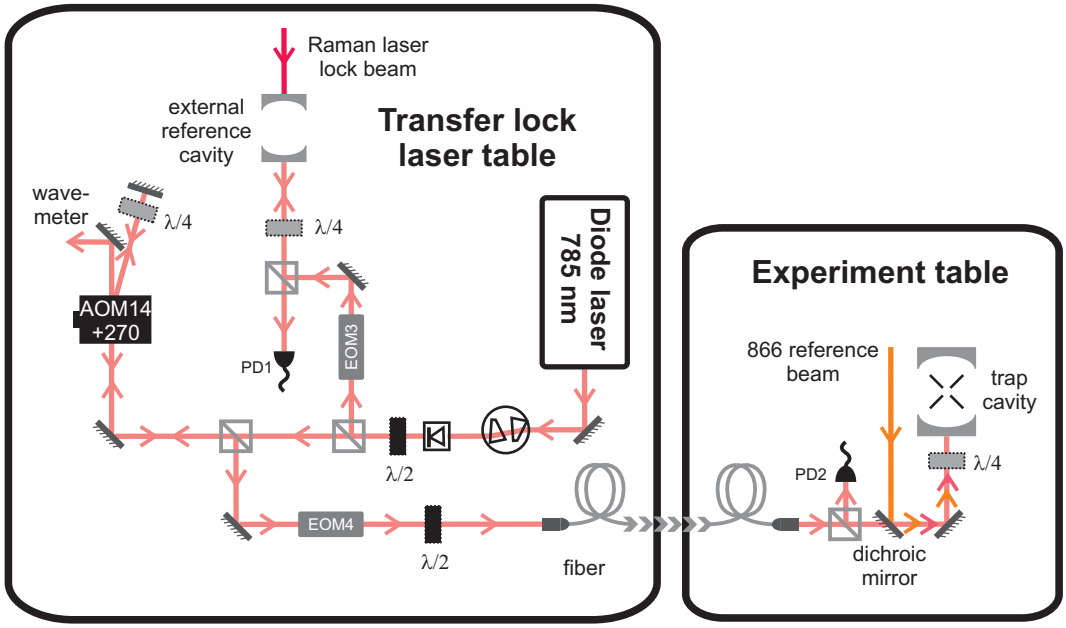

Figure 4.10: Schematic drawing of the transfer lock laser setup. Details of this setup are described in the text of subsection 4.4.

The length of the trap cavity, and hence the resonance to Raman transitions, can be tuned by changing a +270 MHz double-pass AOM (AOM14) frequency located in the 785 laser path going to the trap-cavity. A sweep through cavity modes can be conveniently done in small steps (50 kHz) while the trap cavity's length is continuously stabilized.

4.5 Geometry of the setup

The geometric configuration of laser beam directions and polarizations with respect to the magnetic field vector as well as cavity axis are essential for determining which atomic transitions are allowed and what are their strengths. Also, the relative direction of the trap axis with respect to laser beams and the cavity axis is essential for the understanding of excitation of motional sidebands. This section shows the two setup geometries used in the experiments presented in this thesis.

The orientation of the reference axis x, y and z presented in the figures of this section are arranged with respect to the apparatus as follows: the z axis corresponds to the trap axis, the x axis lies along the cavity axis, pointing towards the cavity output mirror, and the y axis is set perpendicular to the plane formed by trap and cavity axis. In the laboratory frame of reference, the z axis (trap axis) is vertical and points towards the ceiling.

It is important to point out that the coordinate axes described in this section

do not correspond to the ones described in the theoretical model of chapter 3. That is, in order to apply the model to the geometry configurations, it is necessary to rotate the coordinate axis of this section to align the magnetic field to the z axis.

4.5.1 Configuration 1

The configuration of the beams and of the magnetic field used for obtaining the results presented in chapter 5 is shown in figure 4.11.

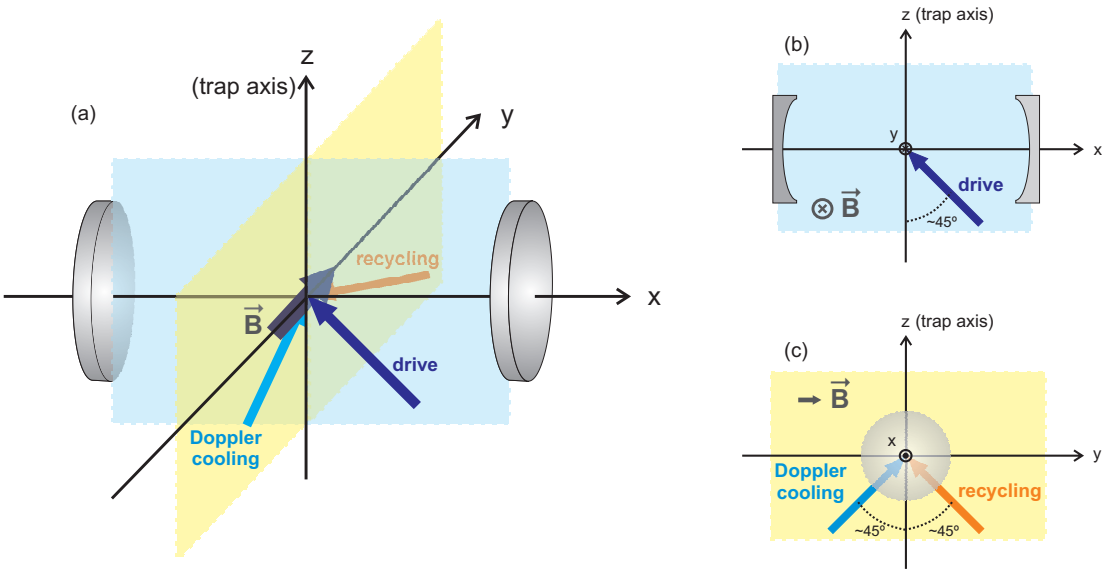

Figure 4.11: Setup configuration for the experiments presented in chapter 5. (a): Full setup; (b): plane xz; (c): plane yz.

In this configuration, the magnetic field is oriented along the y axis (direction determined by the vector $\mathbf{v} = (0, 1, 0)$) and thus perpendicular to both cavity and trap axis. The drive beam (direction determined by the vector $\mathbf{v} = (-1, 0, 1)$) comes from below the output cavity mirror, at 45° with the cavity axis and perpendicular to the magnetic field. The 866 recycling beam (direction $\mathbf{v} = (0, -1, 1)$) enters the trap perpendicularly to the cavity axis and at 45° with the magnetic field, from below the apparatus. The Doppler cooling beam (direction $\mathbf{v} = (0, 1, 1)$) propagates at 45° with the magnetic field and at 90° with both the cavity axis and the 866 recycling laser, incident from below.

4.5.2 Configuration 2

This second geometric configuration is used in the experiments of chapters 6 and 7. It is similar to the configuration 1 but the magnetic field direction is rotated by approximately 45° around the cavity axis (direction determined by the vector $\mathbf{v} =$

(0, 1, −1)) in order to be parallel to the optical pumping beam, which comes from above and is directed along the vector $\mathbf{v} = (0, 1, -1)$. Additionally, the quadrupole 729 laser beam is introduced in the direction $\mathbf{v} = (-1, 0, -1)$, crossing the apparatus from the top of the cavity output mirror, at 45° with both trap and cavity axis in the plane formed by these two axis. The drive and recycling beams remain in the same direction, as can be observed in figure 4.12, depicting this configuration.

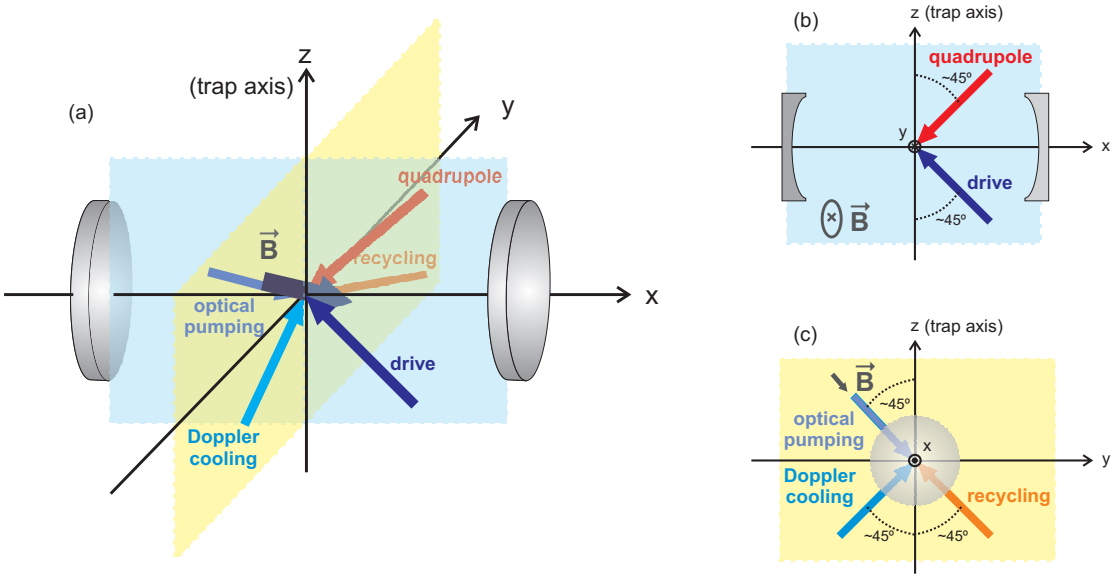

Figure 4.12: Setup configuration used in chapters 6 and 7. (a): Full setup; (b): plane xz; (c): plane yz.

4.6 Detection systems

4.6.1 Detection of the $P_{1/2} \rightarrow S_{1/2}$ ion fluorescence

The ion's presence is usually monitored by collecting the fluorescence emitted when the ion decays from the $P_{1/2}$ to the $S_{1/2}$ manifolds perpendicularly to the cavity axis (along the direction $\mathbf{v} = (0, -1, 0)$). An objective lens (photographic objective from Nikon, magnification ≈ 7, working distance $\approx 55\,\text{mm}$) is used for this collection and the signal is measured with a PMT (photomultiplier tube, with specified quantum efficiency $\approx 26.5\,\%$). The maximum overall estimated detection efficiency for this channel is $1.8\,\%$ [65].

This fluorescence can also be detected by a CCD camera (Andor IXon DV860 AC-BV) on the other side of the chamber and is useful to visualize the ion crystal and confirm the number of trapped ions. The achromat lens used to collect the light

emitted by the ion provides a magnification of approximately 20. The schematic drawing of figure 4.13 pictures these detection systems.

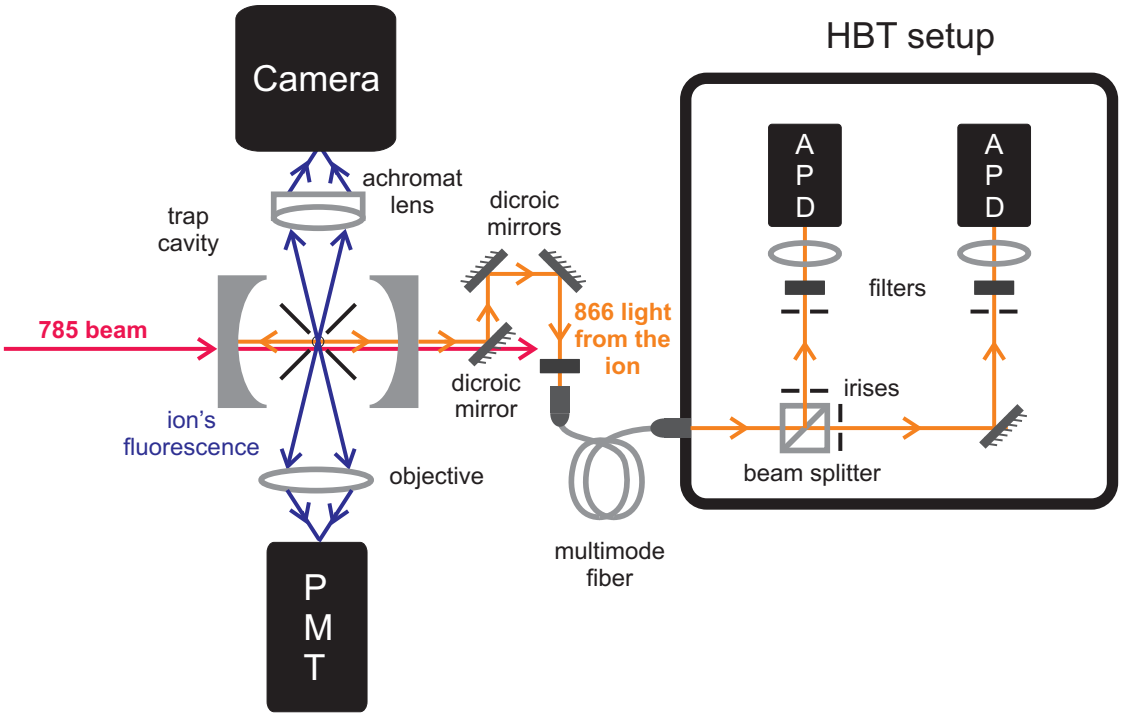

Figure 4.13: Schematic drawing of the detection systems. Details of this setup are provided in the text of section 4.6.

4.6.2 Detection of the cavity photons

The photons produced in the cavity are directed from the preferred cavity output channel to a multimode fiber, which guides them to a Hanbury Brown and Twiss (HBT) setup. In the path to the fiber, three dichroic mirrors and one low-pass optical filter are used to separate the cavity photons from both background light and 785 nm light from the transfer lock laser.

As seen in figure 4.13, the HBT setup is composed of irises, filters, lenses, a non-polarizing beam splitter and two avalanche photodiodes (APDs). The irises have the purpose of reducing the amount of light that is reflected back to the APDs and originates from an APD detection event (known phenomenon described in reference [101]). The filters in front of the APDs (band-pass filters Omega Optical 866DF25) complement the filter at the input of the multimode fiber on the task of eliminating ambient and 785 nm light from the transfer lock laser, leaving the light at 866 nm to be detected. The HBT setup is enclosed in a black box to shield the APDs from undesired ambient light.

The APDs (model SPCM-AQR-15 from Perkin Elmer) have dead times of (88 ± 4) ps. Their quantum efficiencies were measured to be $\eta_{APD1} = (41 \pm 2)\%$ for one of them and $\eta_{APD2} = (42 \pm 2)\%$ for the other. One of the APDs has a dark count rate of approximately 80 counts/s. The other APD had initially a dark count rate of around 100 counts/s; however a bi-stability behavior appeared and this APD currently presents dark count rates that jump from the normal 100 counts/s to a higher 180 counts/s and back in an erratic fashion. New, fiber-coupled, APDs were purchased and shall be implemented in the setup in the near future.

The single-photon events detected by the APDs are counted using a Picoharp counter from PicoQuant. The events on each APD are organized in lists and transmitted to the computer, where they are monitored and stored using our control software (see section 4.7.3).

We have observed that our APDs experience after-pulsing, i.e., one detection event creates an electronic signal that presents a tail extending to a couple of µs. This phenomenon is detailed in Appendix A.

In order to calculate the overall detection efficiency of this channel, it is necessary to obtain the transmission efficiencies of the cavity preferred output channel and of the optical elements in the path as well as the APD quantum efficiencies.

The cavity output channel transmission efficiency is given by [65]

$$\eta_{cav} = \frac{\Im_2 \mathcal{F}}{2\pi} = (19 \pm 3)\%. \tag{4.12}$$

The values of $\Im_2$ and $\mathcal{F}$ used are obtained from table 4.1.

The transmission efficiency of the optical path was obtained by measuring the power in different points of the path from the cavity output toward the APDs. In this process, we also obtained the efficiency of individual elements in the path of the cavity photons, listed in table 4.2.

Optical element	Efficiency
Dichroic mirror before fiber	$(100 \pm 4)\,\%$
Filter before fiber (high λ pass)	$(96 \pm 2)\,\%$
Fiber	$(84 \pm 1)\,\%$
Beam splitter inside HBT box in reflection	$(52 \pm 1)\,\%$
Beam splitter inside HBT box in transmission	$(42 \pm 1)\,\%$
Mirror inside HBT box (path to APD2)	$(98 \pm 3)\,\%$
Band-pass filter in front of APD1	$(79 \pm 2)\,\%$
Band-pass filter in front of APD2	$(84 \pm 2)\,\%$

Table 4.2: Efficiencies of transmission and reflection of different optical elements present in the path of the cavity photons to the APDs.

The global optical path efficiency obtained is $\eta_{opt} = \eta_{opt1} + \eta_{opt2} = (65 \pm 5)\%$, where η_{opt1} and η_{opt2} are the efficiencies of the optical paths going to APDs 1 and 2, respectively. The overall detection efficiency of cavity photons can thus be calculated as follows:

$$\eta_{det} = \eta_{cav}(\eta_{opt1}\eta_{APD1} + \eta_{opt2}\eta_{APD2}) = (5.1 \pm 1)\%. \tag{4.13}$$

Table 4.3 summarizes the global efficiencies involved in the calculation of the overall detection efficiency of the cavity photons.

Global	Efficiencies
Cavity output coupling	$\eta_{cav} = (19 \pm 3)\%$
Optical path to APD1	$\eta_{opt1} = (35 \pm 2.9)\%$
Optical path to APD2	$\eta_{opt2} = (30 \pm 2.5)\%$
Total optical path	$\eta_{opt} = (65 \pm 5)\%$
APD1 quantum efficiency	$\eta_{APD1} = (42 \pm 2)\%$
APD2 quantum efficiency	$\eta_{APD2} = (41 \pm 2)\%$
Overall efficiency	$\eta_{det} = (5.1 \pm 1)\%$

Table 4.3: Cavity output coupling, transmission efficiencies of the optical paths to the APDs and APDs quantum efficiencies of detection. The overall efficiency (η_{det}) of detecting a cavity photon is also calculated.

4.7 Experiment control

The main hardware and software elements used to remotely control our experiment are introduced in this section. The user communicates via a Labview user front end developed in our group (see section 4.7.3) with the hardware elements presented here.

4.7.1 Pulse sequencer hardware

A pulse sequencer hardware FPGA-based developed by Paul Pham and further improved by Philipp Schindler is used to generate fast sequences of RF pulses with frequency, phase and amplitude control. Also, it provides digital outputs that can be used to switch external hardware on time scales of a few tens of nanoseconds.

4.7.2 National Instruments cards

Besides the pulse sequencer hardware, two National Instruments (NI) cards are used to control other electronic devices in our setup. The NI 6703 card is used for

digital and analog outputs; the NI 6711 card has a counter which is used for the photomultiplier and also has analog and digital output channels. Both are controlled via the Labview based software, described in the next subsection.

4.7.3 Control software

A Labview 8.0 program is used to control the experiment, changing parameters, making scans and collecting data. The latest version was developed by Timo Körber in 2007 [102] and was modified to meet our needs. It produces code in a meta-language closely related to Python. The code is interpreted by a server, converted into machine code and sent to the FPGA board via ethernet. In essence, this program controls power, frequency and switching of most of our laser beams and, as mentioned, executes pulse sequences and collects data from both PMT and APDs.

5 Raman spectroscopy

This chapter is dedicated to the study of Raman spectroscopy measurements realized in our system. It begins with a brief introduction to the calibration technique, used to obtain most experimental parameters. The following section addresses the spatial localization of the ion with respect to the cavity by means of probing its position in the standing wave of the cavity field, where the influence of Doppler cooling becomes visible. The final section presents spectroscopy measurements on the Raman transition, where Doppler cooling turns out to be essential to identify the expected transitions and quantify their strength. Experiments with different drive field polarizations are studied. Furthermore, the selection of a particular cavity photon polarization facilitates the observation of the ion motional sidebands in the cavity spectra, which can potentially be used for cavity-assisted sideband cooling. Most of the work presented in this chapter has been published in reference [29].

5.1 Calibration procedure

The correct values of the experimental parameters such as detunings, linewidths and resonant Rabi frequencies of lasers are obtained using a calibration procedure. This technique has already been discussed in [65] and is therefore briefly summarized here.

The calibration experiments consist on continuously applying both 397 calibration and 866 recycling beams and observing the fluorescence from the $P_{1/2} \rightarrow S_{1/2}$ transition as a function of the frequency of the recycling laser for a series of different powers of both beams. Although the 397 calibration beam is used during this procedure, parameters for the drive beam can also be extracted, once both beams originate from the same laser, are guided through the same path to the ion and have their relative frequency difference known. One of these calibration measurements can be seen in figure 5.1 together with the fitted theoretical curve obtained using the model presented in chapter 3.

This calibration experiment reveals four dips on the left side of the fluorescence curve, known as dark resonances [103]. Dark resonances appear due to the creation

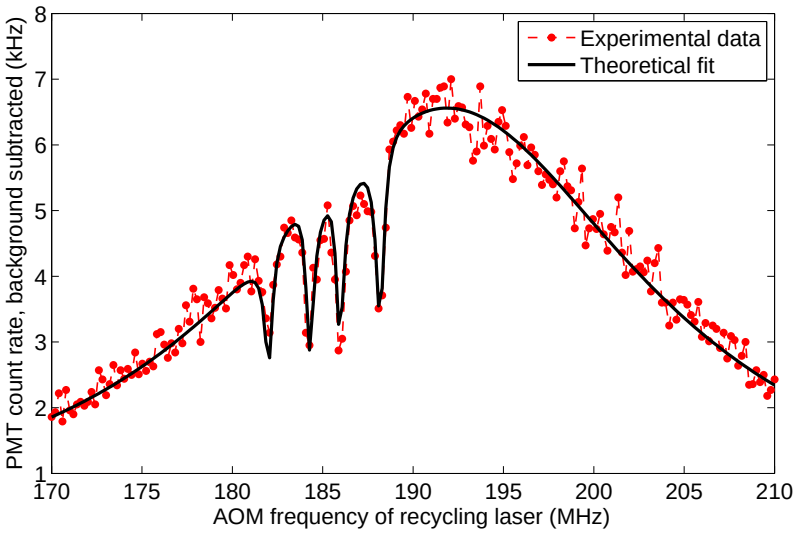

Figure 5.1: Calibration experiment: ion's fluorescence as function of the 866 nm recycling laser frequency. Dark resonances are apparent.

of a dark state when the 397 calibration and the recycling lasers are in resonance with one of the S-D transitions. When this happens, the population is directly transferred from the D to the S state, avoiding populating the P state and therefore preventing the emission of fluorescence. The presence of these dark resonances is essential for this calibration process.

The fit to a series of such experiments, performed using the 8-level atomic model described in chapter 3, allows us to extract the amplitude of the magnetic field acting on the ion as well as the linewidths, detunings and power calibration curves for both lasers involved in these measurements. During all experiments presented in this chapter, the 397 calibration and drive beams and the 866 recycling beam have their intensity stabilized.

The calibration measurements are usually executed before and after the experiments of interest to correct for slow frequency drifts of the lasers involved. Although reliable, the calibration procedure has an error bar of around 25%, revealing the uncertainties in the fitting procedure, performed manually, and also small fluctuations in power and drifts in frequency. The parameters extracted from such experiments are used, within their error bars, as inputs to the theoretical model that overlaps with the corresponding experimental data in the next sections as well as in the next chapter.

5.2 Ion localization in the standing wave

The goal of the experiments presented in this section is to map the interaction between the ion and the cavity field at different positions of the cavity field standing wave.

5.2.1 Cavity standing wave experiments

In this experiment, the cavity position is varied along its axis by changing an offset voltage to the slow piezo under one of the cavity mirrors while the cavity length is actively stabilized through the other cavity mirror piezo. A Raman transition is driven and photons emitted into the cavity are detected. By monitoring these cavity photons, the interaction between the ion and the cavity field is probed for different positions of the ion in the cavity standing wave profile. As the ion's position in the standing wave varies, Ω_{eff} is altered and the number of produced cavity photons changes. This experiment can be performed either in a continuous or a pulsed scheme as follows.

Continuous scheme

A typical standing wave pattern on the continuous scheme can be seen in figure 5.2. In this experiment, both drive and 866 recycling lasers are continuously on and the signal of cavity photons on both APDs are added and plotted as a function of the position of the cavity around the ion.

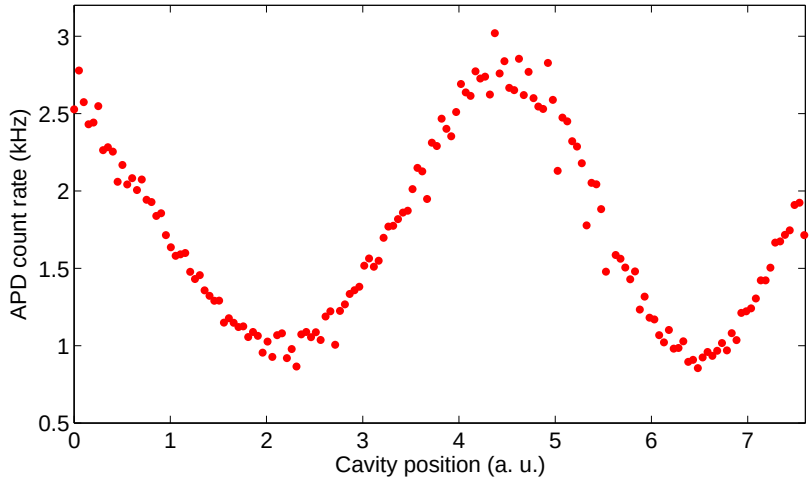

Figure 5.2: Cavity standing wave measurements in the continuous scheme.

As can be seen in this figure, the cavity photon production is correlated

with the position of the ion in the cavity field standing wave, being maximum at its antinodes and minimum at its nodes. The visibility V of such curves can be calculated from the maximum ($I_{\max}$) and minimum ($I_{\min}$) intensities as $V = (I_{\max} - I_{\min})/(I_{\max} + I_{\min})$. In an ideal situation in which the ion is a point-like particle and the relative position between cavity and ion is fixed for each data point, the visibility of this curve should be 100 %. However, in our experiment both cavity and ion move, smearing out the standing wave pattern and decreasing its contrast to around 59 % [104]. This issue is discussed in more detail in the subsection 5.2.2, where Doppler cooling is applied to the ion to decrease its motional contribution to its uncertainty in position.

Pulsed scheme

The experiment can also be performed in a pulsed fashion in order to prevent the Doppler cooling beam from competing with the Raman transition. The corresponding pulse sequence is depicted in Figure 5.3. The drive beam is in this case π-polarized and tuned to one of the Raman transitions.

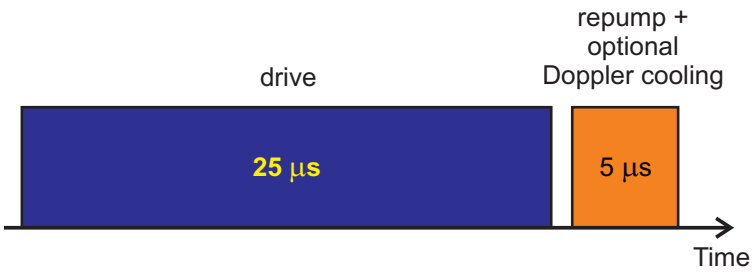

Figure 5.3: Pulse scheme used on the pulsed standing wave measurements.

The sequence starts with a 25 µs drive laser pulse, followed by a 1 µs wait time. After a 5 µs recycling pulse with the 866 nm laser, followed by another 1 µs wait time, the sequence is repeated. During the recycling stage, a near-resonant cooling laser can be applied to the ion for Doppler cooling. We have confirmed that this time is sufficient to reach steady-state conditions. During the whole sequence, we detect if a photon has been emitted by the cavity with the APDs. Each data point consists of the integration over 24000 sequence repetitions. Changing the offset voltage of one of the two cavity piezos allows us to move the cavity field with respect to the ion for each data point. The other piezo is locked to stabilize the cavity length and follows the displacement of the first piezo. Experimental results of the cavity standing wave in this pulsed scheme are presented in the next subsection.

5.2.2 Influence of the Doppler cooling on the cavity standing wave

As mentioned in the previous subsection, the interaction between the cavity field and the ion can be disturbed by mechanical noise in the cavity as well as by the delocalization of the ion due to its finite temperature. The influence of this second perturbation becomes clear in the experimental results of figure 5.4, where measurements of the cavity standing wave in the pulsed scheme are shown for the cases with (blue dots) and without (red squares) Doppler cooling.

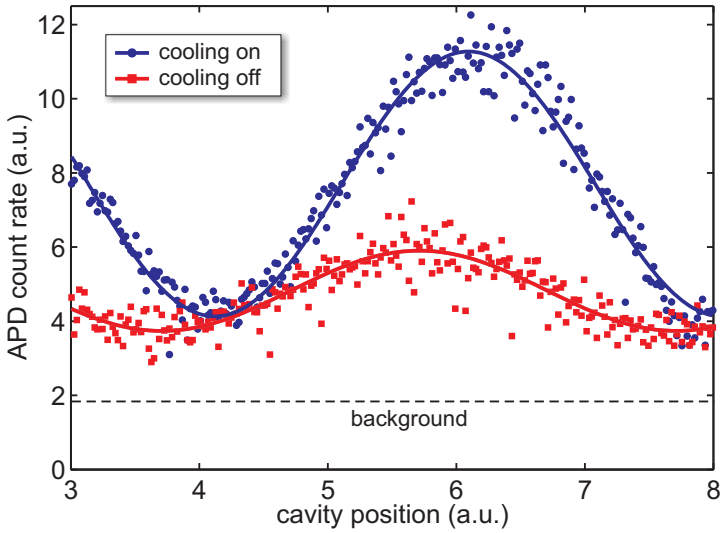

Figure 5.4: Cavity standing wave for the cases with (blue dots) and without (red squares) Doppler cooling.

The standing wave visibilities obtained from the fits (solid lines in figure 5.4) are $V_{\mathrm{cool}} = 60\,\%$ and $V_{\mathrm{no\,cool}} = 35\,\%$ with and without Doppler cooling, respectively. The root-mean-square size σ of a Gaussian wavepacket describing the localization of the ion is related to the observed visibility by the relation $V = \exp(-2(\kappa\sigma)^2)$, where $\kappa = 2\pi/(866\,\mathrm{nm})$ is the wavenumber of the cavity field [22, 104]. This leads to a relative localization of the ion wavepacket with respect to the cavity field of $\sigma_{\mathrm{cool}} = 70\,\mathrm{nm}$ and $\sigma_{\mathrm{no\,cool}} = 100\,\mathrm{nm}$. The comparably large ion delocalization in the absence of the Doppler cooling beam is an indication of insufficient cooling by the far-detuned drive laser. Although additional Doppler cooling improves the observed localization, the theoretical limit of $\sigma_{\mathrm{theory}} \approx 18\,\mathrm{nm}$ is not reached. We attribute this discrepancy mostly to center-of-mass vibrations of the U-shaped cavity mirror mount. This is supported by an interferometric measurement of the cavity's motion, presented in Appendix B.

Another consequence of the ion's delocalization is a reduced atom-cavity cou-

pling strength g. From a localization of 70 nm, we derive that g_0 is reduced from $g_{0\max} = 1.6\,\mathrm{MHz}$ (see table 3.2) to $g_{0\mathrm{obs}} = 1.4\,\mathrm{MHz}$. This is confirmed in section 5.3 by quantitative agreement between the observed spectra and the numerical simulations, in which we use $g_{0\mathrm{obs}}$ as one of the calibrated input parameters.

The horizontal offset between the two curves is due to a hysteresis of the cavity piezos, which also induces a small distortion on the $\sin^2$ pattern. During such experiments, we have also discovered an astonishing slow time scale necessary for the cavity slow piezo to move after a voltage was applied to it. According to our investigation, a maximum rate of approximately 1 V/s has been established above which the slow cavity piezo lags behind the applied voltages, which leads to a stretching of the horizontal axis scale.

5.3 Spectra of the Raman transition

This section contains spectroscopy results on the Raman transition obtained by looking at the cavity output signal as a function of the frequency of the drive laser. The experiments presented here were performed in the continuous scheme in order to obtain a higher signal at the APDs. The drive and 866 recycling lasers as well as a weak Doppler cooling beam (used only in some experiments) were set on throughout the whole experiment while scanning the drive laser frequency and looking at the added signal of the two APDs.

5.3.1 Raman transition strengths for a particular experiment configuration

A discussion of the different Raman transitions was performed in section 3.6.1. However, for a particular experiment configuration, polarizations and projections of the electric fields onto the quantization axis need to be taken into account, that is, the angles α and β of equations 3.12 and 3.15 have to be considered.

According to the geometry configuration 1 presented in subsection 4.5.1, the drive laser is incident to the ion in a direction perpendicular to the magnetic field. This way, if it is linearly polarized parallel to the magnetic field vector (π-configuration, $\beta = 0$), its light can excite π transitions ($\Delta m_{PS} = 0$). However, if its polarization is linear and perpendicular to the magnetic field vector (σ-configuration), it can be decomposed into a sum of σ^+ and σ^- components with respect to the quantization axis, determined by the magnetic field vector. Since only one of the σ^+/σ^- components of the drive field couples to the ion, i.e., $\cos\beta = 0$ for

one component and $\cos\beta = 1$ for the other, the respective effective line strengths are reduced by a factor of 2. That is, the line strengths of transitions G, H, I, J, K and L provided in table 3.3 are decreased to half of their maximum values.

Furthermore, the cavity axis is perpendicular to the quantization axis, which restricts the geometric overlap between the electric field projections of the σ^+/σ^- polarized Stokes photons ($\Delta m_{PD} = \pm 1$) onto the modes supported by the cavity. In this case, the σ^+/σ^- polarized Stokes photons can be decomposed in terms of vectors parallel ($\cos\alpha = 0$) and perpendicular ($\cos\alpha = 1$) to the cavity axis. This geometry mismatch cuts downs the line strength of transitions with $\Delta m_{PD} = \pm 1$ by a factor of 2. This way, lines A, C, D and F assume half their maximum values and lines G, I, J and L are further brought down by a factor of 2. The projection of the emitted photon's electric field onto the mode of the cavity field results in horizontally (vertically) polarized cavity photons for π (σ^+/σ^-) transitions.

Table 5.1 summarizes the effective line strengths for this geometry configuration.

Line	From $\lvert S_{1/2}, m_S\rangle$	Via virtual $\lvert P_{1/2}, m_P\rangle$	To $\lvert D_{3/2}, m_D\rangle$	Δm_{SP}	Δm_{DP}	Eff. line strength
A	+1/2	+1/2	-1/2	0	+1	1/36
B	+1/2	+1/2	+1/2	0	0	1/9
C	+1/2	+1/2	+3/2	0	-1	1/12
D	-1/2	-1/2	-3/2	0	+1	1/12
E	-1/2	-1/2	-1/2	0	0	1/9
F	-1/2	-1/2	+1/2	0	-1	1/36
G	+1/2	-1/2	-3/2	-1	+1	1/12
H	+1/2	-1/2	-1/2	-1	0	1/9
I	+1/2	-1/2	+1/2	-1	-1	1/36
J	-1/2	+1/2	-1/2	+1	+1	1/36
K	-1/2	+1/2	+1/2	+1	0	1/9
L	-1/2	+1/2	+3/2	+1	-1	1/12

Table 5.1: Effective line strengths of the possible Raman transitions. The projection of the emitted photon's electric field onto the mode of the cavity field results in horizontally (vertically) polarized cavity photons for $\Delta m_{DP} = 0$ ($\Delta m_{DP} = \pm 1$).

Both effects are also depicted in figures 5.5(b) and 5.6(b), where the effective line strengths are depicted in full colored bars and compared with the maximum line strengths (dotted bars). The polarization of the cavity photons indicated in these figures is already its projection onto the cavity mode, as described previously in this subsection. The corresponding level schemes are shown in figures 5.5(a) and 5.6(a).

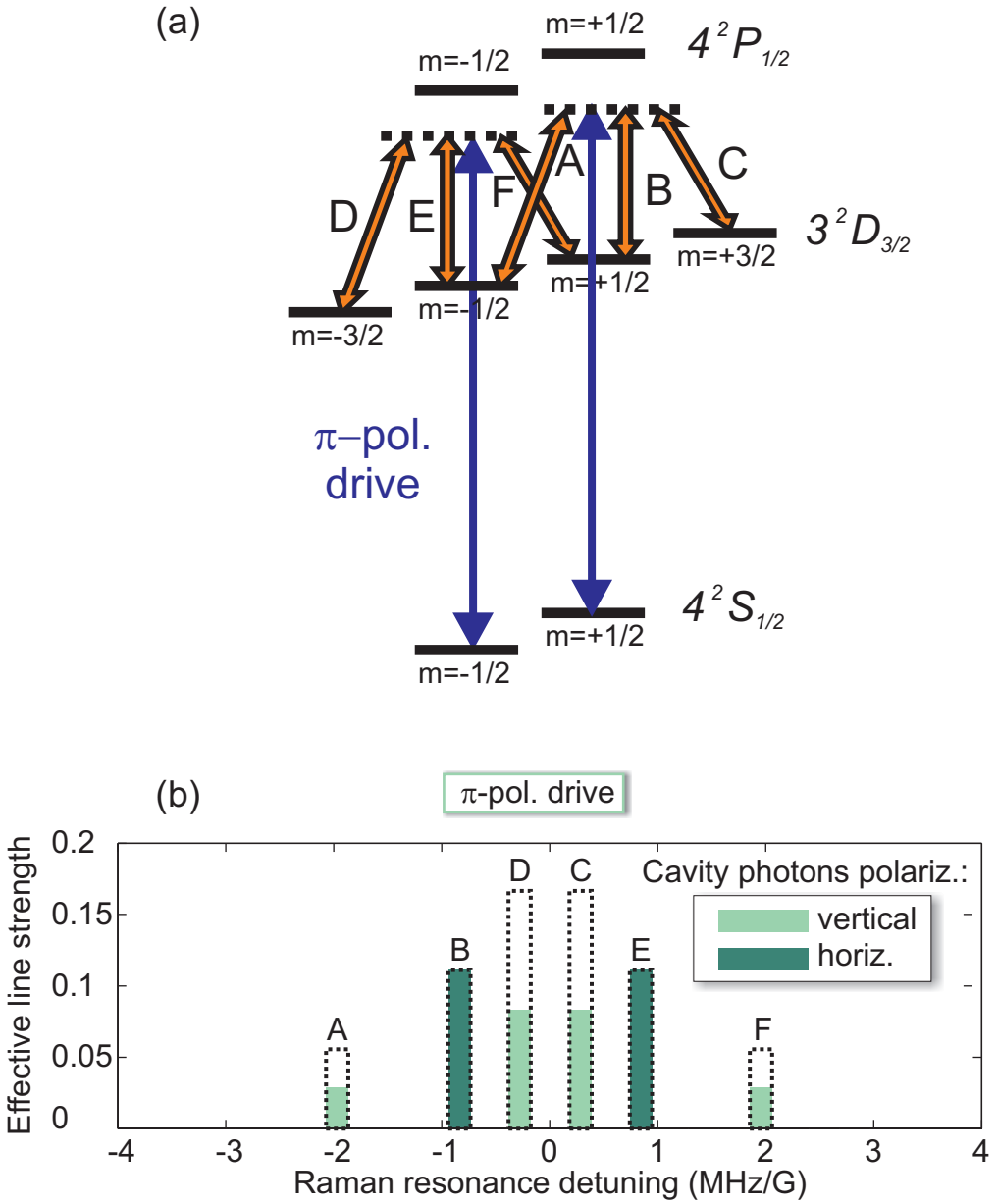

Figure 5.5: (a) Level scheme of possible Raman transitions with the cavity for a π-polarized drive laser. (b) Effective Raman transition strengths for a π-polarized drive laser when considering the geometry configuration presented in subsection 4.5.1. The dotted rectangles in (b) indicate the maximum line strengths from figure 3.4 and the full rectangles correspond to the effective line strengths for this geometry configuration.

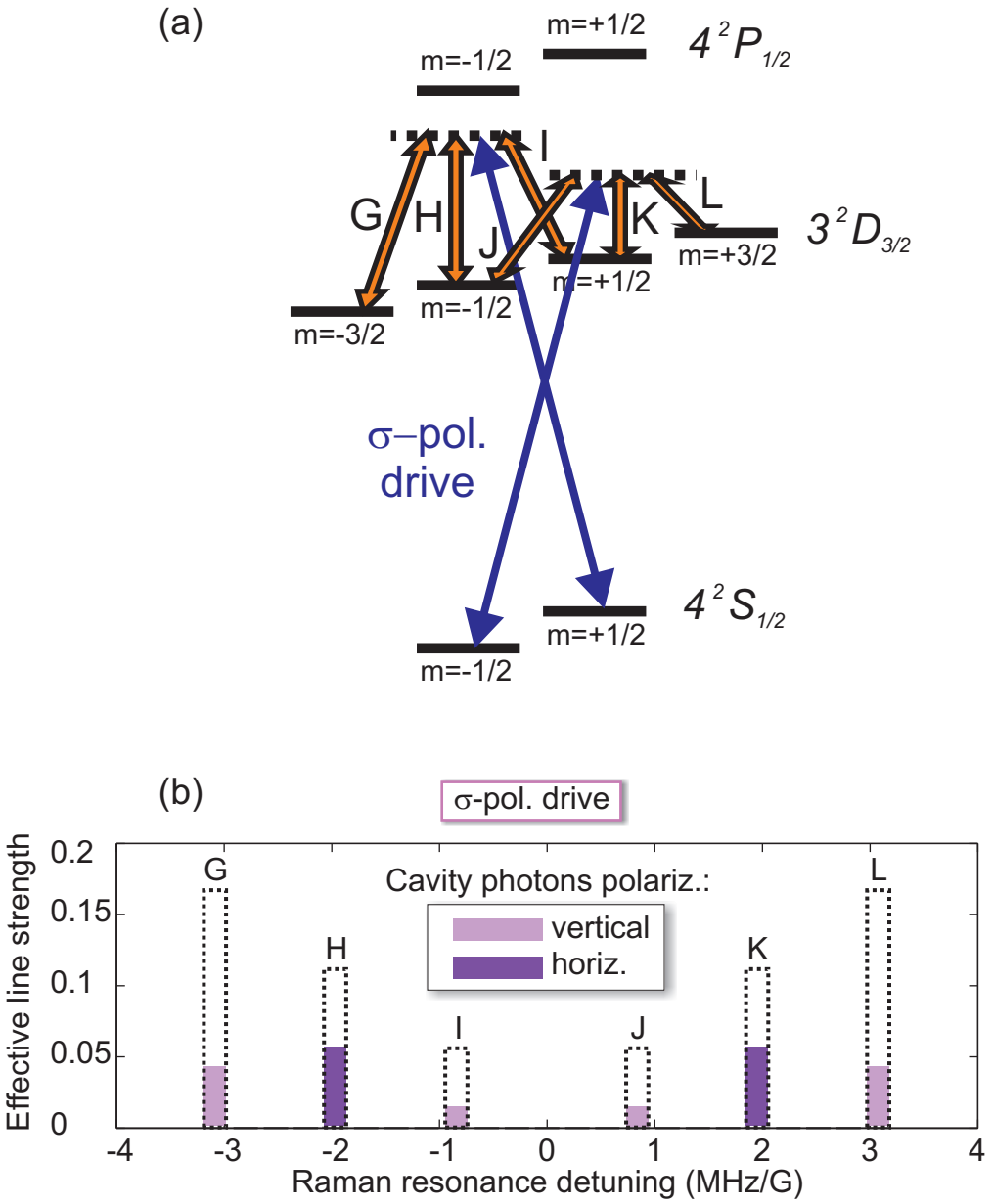

Figure 5.6: (a) Level scheme of possible Raman transitions with the cavity for σ-polarized drive laser. (b) Effective Raman transition strengths for a σ-polarized drive laser when considering the geometry configuration presented in subsection 4.5.1. The dotted rectangles in (b) indicate the maximum line strengths from figure 3.5 and the full rectangles correspond to the effective line strengths for this geometry configuration.

5.3.2 Effects of Doppler cooling on the Raman spectra

It was already shown in the cavity standing wave measurements of subsection 5.2.2 that the motion of the ion has an influence on the ion's interaction with the cavity field. The manifestation of this motion is also expected in spectroscopy measure-

ments of the Raman transition, once these are directly related to the ion-cavity interaction. These motional effects on the spectroscopy measurements become obvious in figure 5.7, where Raman spectra in the π drive laser configuration with (blue continuous line) and without (red dotted line) the Doppler cooling beam are shown for a magnetic field $B \approx 0.28\,\mathrm{mT}$.

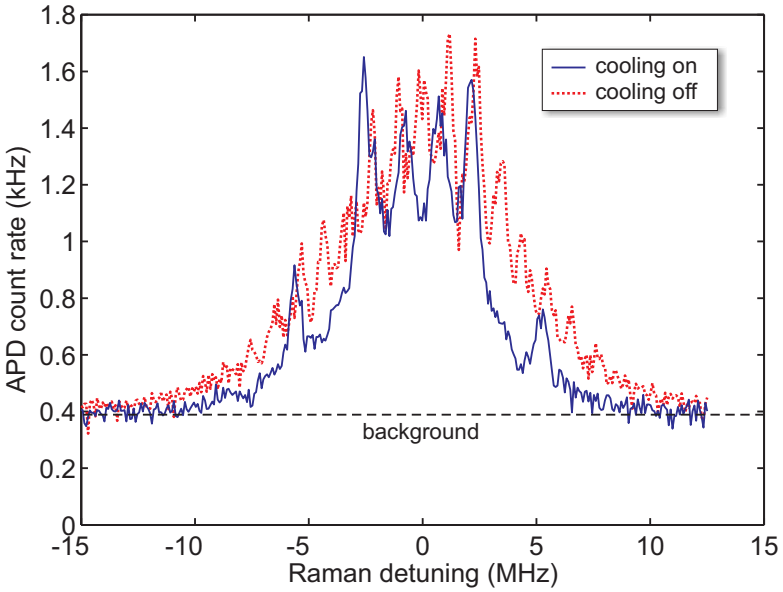

Figure 5.7: Spectrum of the Raman transition for a magnetic field of 0.28 mT and a π-polarized off-resonant drive beam for the cases with (blue continuous line) and without (red dotted line) extra Doppler cooling laser.

The spectrum without Doppler cooling exhibits no clearly identifiable carrier resonances but rather a series of resonances including carrier and motional sidebands. In this situation, it is only possible to obtain spectral information if the ion is sufficiently cold. This can be achieved by continuously applying a weak near-resonance Doppler cooling beam in addition to the far-detuned Raman drive laser, as it was done for the blue continuous line in figure 5.7. As this experiment was realized in a continuous fashion, it is important to set the Doppler cooling beam power high enough to provide good Doppler cooling and low enough not to compete too much with the Raman transition. For the chosen experimental parameters, no significant influence of the Doppler cooling beam on the Raman resonances has been observed.

5.3.3 Raman spectra for different drive polarizations

Theory predicts significant differences in the Raman spectrum depending on the drive laser polarization. Experimental Raman spectra for different drive polariza-

tions have been observed and the Raman transitions have been identified and quantified based on the effective line strengths presented in figures 5.5 and 5.6 and using the model of chapter 3.

In this series of experiments, the drive and recycling lasers are simultaneously and continuously applied with intensity-stabilized Rabi frequencies of $\Omega_1 = 82(8)\,\mathrm{MHz}$ and $\Omega_2 = 7.7(7)\,\mathrm{MHz}$, respectively. The recycling laser is detuned by $\Delta_2 = 0.5(2)\,\mathrm{MHz}$ to the low-frequency side of the $D_{3/2} \rightarrow P_{1/2}$ resonance. In addition, a near-resonant cooling laser with a detuning of $\approx 10\,\mathrm{MHz}$ below the $S_{1/2} \rightarrow P_{1/2}$ transition is continuously applied to the ion to perform efficient Doppler cooling. Since the cooling laser is operated well below saturation, it does not significantly reduce the Raman transition strengths. The number of photons detected by both APDs are counted in a time interval of 1 s for each data point as a function of the drive laser detuning from Raman resonance with the cavity. The degeneracy between the magnetic sublevels m_J is lifted by a magnetic field of $B \approx 0.28\,\mathrm{mT}$. Figure 5.8 shows experimental spectra (blue continuous lines) of all six Raman resonances in the ion-cavity system for σ (a) and π (b) polarizations of the drive laser.

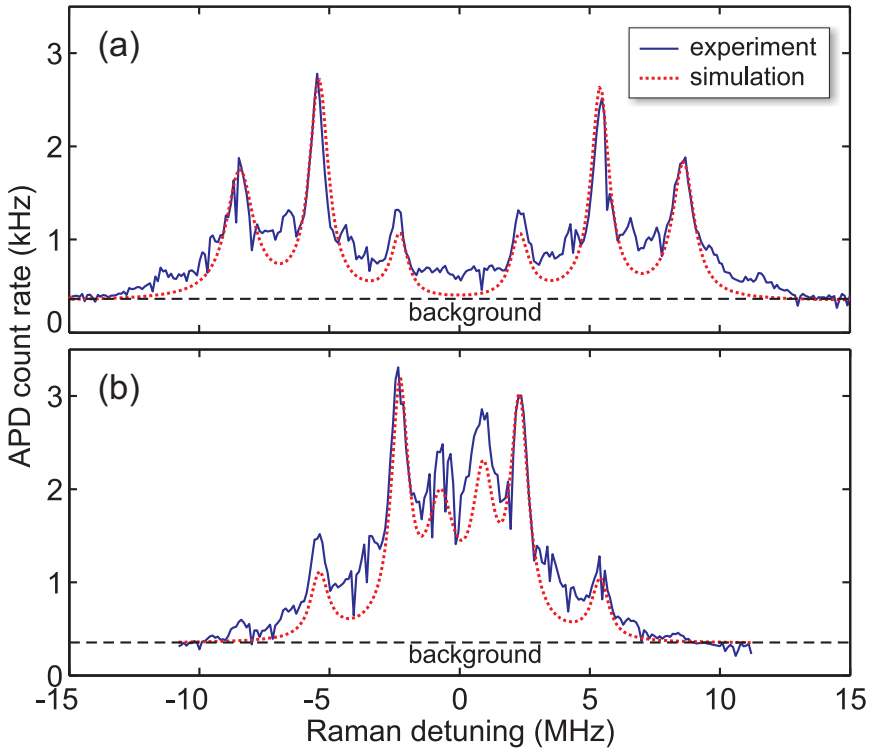

Figure 5.8: Raman spectra for different drive laser polarizations: (a) σ-polarized drive laser; (b) π-polarized drive laser. The blue continuous lines represent the experimental data and the red dotted lines the simulations.

The simulation curves, presented in this figure as red dotted lines, were ob-

tained from the model described in chapter 3. The parameters used were all independently calibrated (as described in Section 5.1) but adjusted within their calibration error to match the experimental data. The observed spectroscopic features are quantitatively reproduced by the simulation and agree with the effective line strengths and spectral separations as schematically depicted in figures 5.5 and 5.6. The line strengths presented in these figures show an asymmetry which we attribute to preferential optical pumping into the $|S_{1/2}, +1/2\rangle$ ground state by the recycling laser. This is supported by the master equation simulation of the experiment. Small deviations in the strength of the resonances between theory and experiment are attributed to weak additional optical pumping by the near-resonant Doppler cooling laser, which is not accounted for in the simulations. Structures appearing at both sides of the experimental Raman transition peaks are not observed in the simulations and are discussed in the next subsection.

5.3.4 Polarization of the cavity photons

According to figure 5.5, peaks in the Raman spectrum correspond to either horizontally (π) or vertically (σ) polarized cavity photons. This was confirmed by an experiment in which a polarizer was placed at the cavity output, allowing us to selectively detect the photon's polarization state.

The result of this measurement is shown in figure 5.9 for π drive laser configuration and a magnetic field of $B \approx 0.61\,\mathrm{mT}$. Again, the simulation agrees quantitatively with the experimental data. The asymmetry around zero Raman detuning and the discrete mismatch between theory and experiment in the line strengths in figure 5.9 have been already explained in the previous subsection.

The experimental data in figure 5.9(a) distinctly shows additional resonances with weaker strengths separated by approximately $\pm 1.1\,\mathrm{MHz}$ and $\pm 2.9\,\mathrm{MHz}$ from the main resonances, as can be seen more clearly in this figure's inset. These peaks are identified as motional sidebands of the axial and radial motion of the ion in the trap [105], described in section 4.1. This is a first proof-of-principle experiment showing that we can resolve and address the oscillation modes of the ion in the trap.

Since the sideband Rabi frequencies scale approximately as the square root of the number of motional excitations [90], the effect of motional sidebands on the spectrum is expected to become more pronounced if the ion is hot. This is exactly the effect seen in subsection 5.3.2, where the motional sidebands completely dominate the Raman spectrum.

The observation and distinction of the motional sidebands of the ion through Raman spectroscopy using an optical cavity suggests the use of the cavity for as-

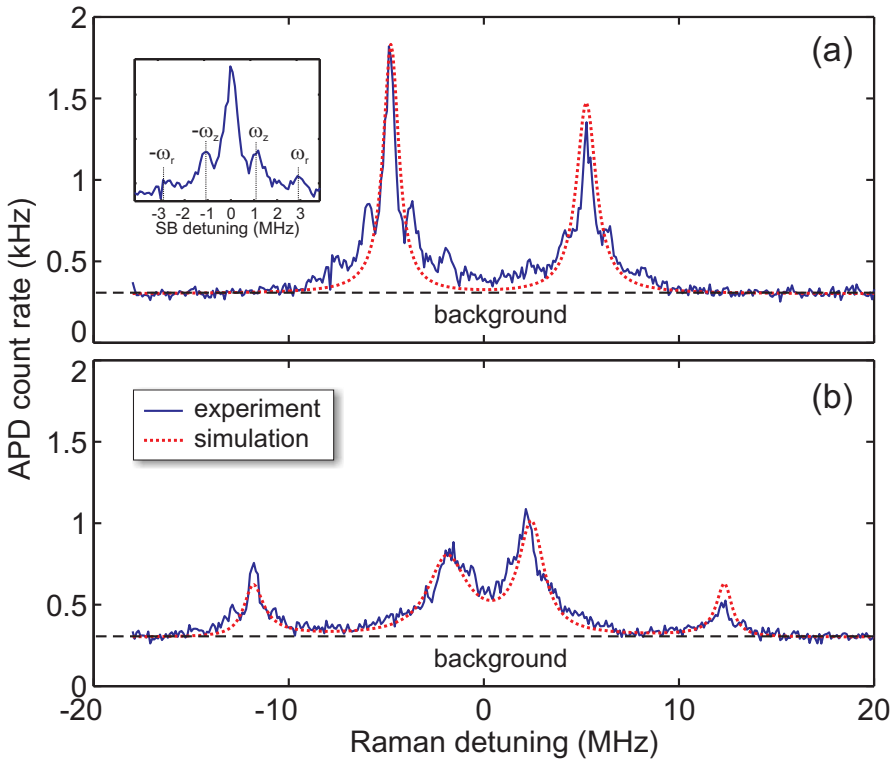

Figure 5.9: Raman spectra in the π drive laser configuration for different cavity photon polarizations: (a) horizontal; (b) vertical. The inset in (a) shows the axial (ω_z) and radial (ω_r) sidebands of secular motion of the ion in the trap.

sisted sideband cooling, with the cavity decay rate being the dominant channel for dissipation [106, 107]. Sideband cooling of ions has already been demonstrated [108] although not to the ground state of motion, which seems to be achievable with the setup presented here.

6 High-efficiency single-photon source

Results of a deterministic single-photon source from a single ion interacting with the cavity field are presented in this chapter. The high photon creation efficiency achieved here represents a threefold improvement over our previous measurements [65]. A description of the experiment is provided in the first section of this chapter. Results of the second-order correlation function are then shown, demonstrating a high suppression of two-photon events limited only by background counts. The cavity photon pulse shape is obtained, with good agreement between experiment and simulation. Moreover, theoretical analysis of the temporal evolution of the atomic populations provides relevant information about the dynamics of the process and opens the way to future investigations of a coherent atom–photon interface. The work presented in this chapter has been published in reference [64].

6.1 Description of the single-photon source experiment

In this experiment, a particular Raman transition of the drive laser σ-configuration is used to produce single photons in the cavity. The experiment is performed in a pulsed scheme and both laser and cavity are detuned from the $P_{1/2}$ manifold by $\Delta_d \approx \Delta_c \approx 335$ MHz. The actual values of these detunings are set to fulfill the selected $\left|S_{1/2}, +1/2\right\rangle \rightarrow \left|D_{3/2}, -1/2\right\rangle$ Raman resonance, as depicted in figure 6.1. To lift the Zeeman degeneracy, a magnetic field of $B = 0.2\,\mathrm{mT}$ is applied to the ion perpendicular to the cavity axis (see configuration 2 in subsection 4.5.2).

In order to achieve a high efficiency and guarantee the production of only one photon at a certain time interval, the experiment is realized in a pulsed fashion, with the pulse sequence depicted in figure 6.2. The cavity is kept resonant to the chosen Raman transition throughout the entire experiment. An initial drive laser pulse of 120 μs is responsible for generating a photon in the cavity, followed by a wait interval of 250 μs. This long wait time is not necessary but allows us to resolve the peaks

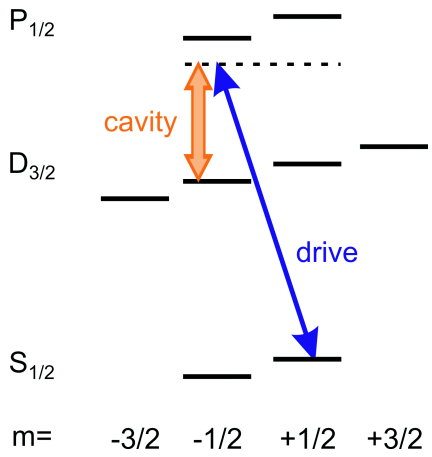

Figure 6.1: Raman transition selected for production of single photons.

in the photon correlation data easily. As the $D_{3/2}$ state is metastable, a laser pulse of 20 µs at 866 nm coupling the $D_{3/2}$ and $P_{1/2}$ manifolds is then applied to recycle the atomic population, in conjunction with a red-detuned beam for Doppler cooling on the $S_{1/2} \rightarrow P_{1/2}$ transition. This drive pulse sequence constitutes one trial and ends with a 20 µs optical pumping laser pulse, as can be seen in Figure 6.2(a). This optical pumping pulse acts on the $\left|S_{1/2}, -1/2\right\rangle \rightarrow \left|P_{1/2}, +1/2\right\rangle$ transition and, with the help of the recycling laser active during this stage, prepares the ion in the initial state $\left|S_{1/2}, +1/2\right\rangle$ with an efficiency $> 98\,\%$.

This 414.5 µs long sequence is repeated 100 times to complete one cycle, which ends with intensity stabilization for the drive and recycling lasers, as shown in figure 6.2(b). This cycle is then repeated 35 times within each run, as seen in figure 6.2(c). For the data exhibited in this chapter, we measured 4 102 runs comprehending 14 357 000 trials over the duration of three hours. Photon events are recorded in the two APDs with a resolution of 4 ps and an efficiency of $\eta_{det} = (5.1 \pm 1.0)\,\%$, where this number represents the probability that a photon created in the cavity will be detected by the APDs and is explained in subsection 4.6.2.

All data presented here were obtained with one and the same ion, its coupling to the mode of the cavity controlled precisely over the course of many hours. Sudden episodes in which the ion becomes heated are observable as brief dropouts of the signal from the cavity and were discarded from the data obtained, comprising 174 runs (eight minutes of data containing 609 000 trials). These dropouts are attributed to collisions of the ion with background gas, as also seen by other experiments in our group. In addition, 219 runs (ten minutes of data containing 766 500 trials) were discarded due to the onset of a rapid drift in the laser frequencies of the experiment. This drift has been observed in the form of a significant decrease in the

signal of cavity photons, which could be recover by proper adjustments of the laser frequencies.

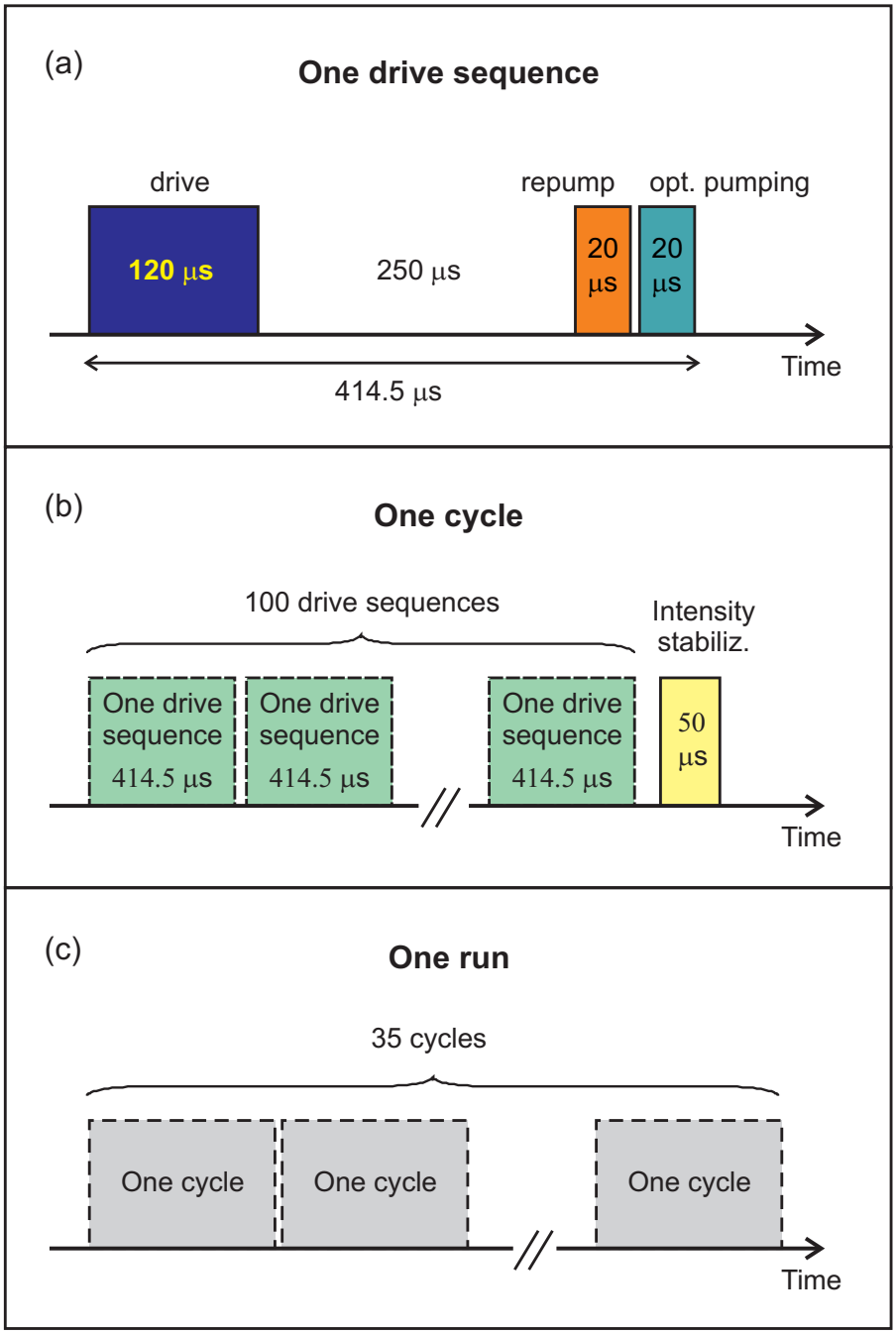

Figure 6.2: Pulse scheme used in the single-photon source experiment: (a) one drive pulse sequence; (b) one cycle; (c) one experimental run.

6.2 Single-photon source results

6.2.1 Experimental second-order photon correlation function

A theoretical description of the second order correlation function was provided in section 3.7 together with the method used for simulating it. The experimental second-order temporal correlation function $g^{(2)}(\tau)$ is obtained from cross-correlations between photon arrival times at the two APDs as a function of time delay τ between these detection events.

More precisely, we obtain a list of photon arrival times from each APD and we cross-correlate these lists and create a histogram $H(t_k, \Delta t_{\text{bin}})$ containing the number of correlation events as a function of the time delay ($\tau = t_k$) between them. The width of each histogram bar, Δt_{bin}, indicates the resolution we choose to process the data, which is only limited by the APDs' detection resolution of 4 ps. We then subtract the influence of the background in these correlations according to [63], that is, we eliminate background-signal and background-background correlations as follows

$$H_{\text{nobckgnd}}(t_k, \Delta t_{\text{bin}}) = H(t_k, \Delta t_{\text{bin}}) - (S_1 B_2 + S_2 B_1 + B_1 B_2)\Delta t_{\text{bin}} T, \tag{6.1}$$

where B_1 and B_2 are the total background counts in APDs 1 and 2, $S_1 = R_1 - B_1$ and $S_2 = R_2 - B_2$ are the background subtracted counts in each of these APDs and T is the total measurement time. This method assumes that the noise follows a Poissonian distribution, which is confirmed by a flat correlation function, measured without the influence of the ion. After a normalization procedure, we can write the normalized and background subtracted second order correlation function as

$$g^{(2)}(\tau = t_k) = \frac{H_{\text{nobckgnd}}(t_k, \Delta t_{\text{bin}})}{S_1 S_2 \Delta t_{\text{bin}}^2} \cdot \frac{1}{T \Delta t_{\text{bin}}}. \tag{6.2}$$

Figure 6.3 shows the experimental results of a second order correlation function (blue dots), overlapped with theoretical simulations (red line). The temporal structure of $g^{(2)}(\tau)$ reveals the characteristics of a pulsed source of light: the individual peaks are separated by the drive sequence (or trial) period of 414.5 µs (repetition rate of 2.4 kHz), and their width is given by the convolution of the waveform of two single pulses. The defining characteristic of a single-photon source is evident in the absence of a peak at $\tau = 0$, which reflects the probability of detecting two photons within the same drive sequence. The single-photon nature of the source is due to the fact that exactly one ion is trapped within the optical cavity. After emitting

a photon into the cavity mode, the ion occupies the metastable $D_{3/2}$ state with a one-second lifetime, ensuring no further coupling to the drive beam. The binning size used for this data plot was $\Delta t_{\text{bin}} = 10\,\mu\text{s}$.

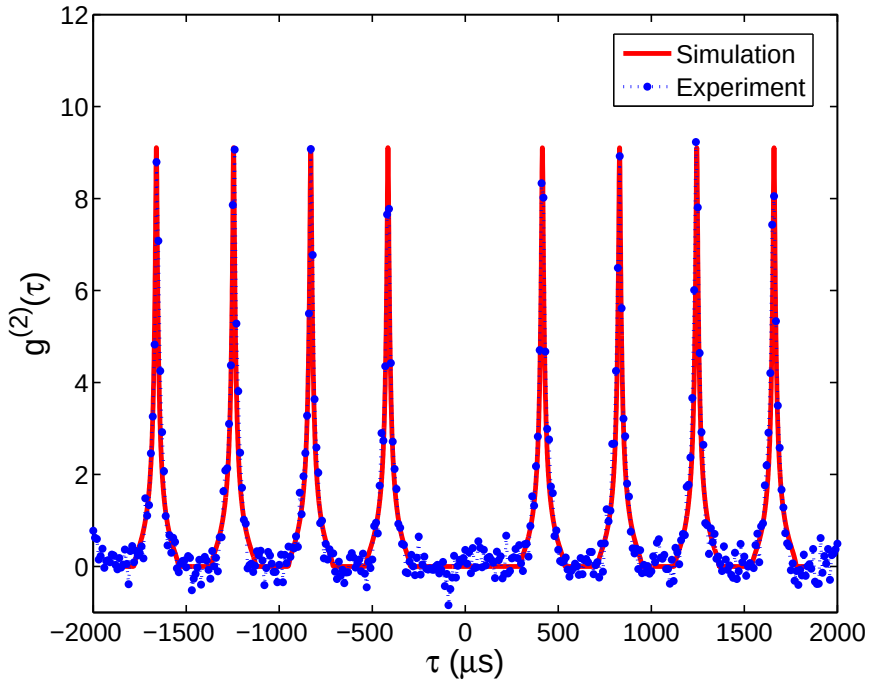

Figure 6.3: Second-order correlation function: experimental data (blue dots) and theoretical curve (red line). The absence of a peak at $\tau = 0$ confirms the single-photon character of our source.

For better inspection of the region around $\tau = 0$, a second plot of the same data is presented in figure 6.4 for a smaller bin size of $1\,\mu\text{s}$ and a shorter time window but this time without normalization and background subtraction. We observe a total of 150 ± 150 background-subtracted counts in a window of $\pm 207.25\,\mu\text{s}$ around $\tau = 0$. The suppression of two-photon events is thus limited entirely by background counts, which consist solely of APD dark counts. In comparison, we detect $581\,000 \pm 2\,000$ single photons over the entire measurement period.

In order to avoid spurious correlations due to the APDs afterpulsing, discussed in Appendix A, we have introduced in the data processing an artificial dead time of $2.5\,\mu\text{s}$, within which the after-pulsing occurs with $1.1\,\%$ probability. In addition, we observe two narrow peaks in cross-correlations at $\tau = \pm 125\,\text{ns}$ corresponding to a photon emitted by one APD during a detection event (a known property of these devices [101]), then reflected back from the cavity output mirror to the other

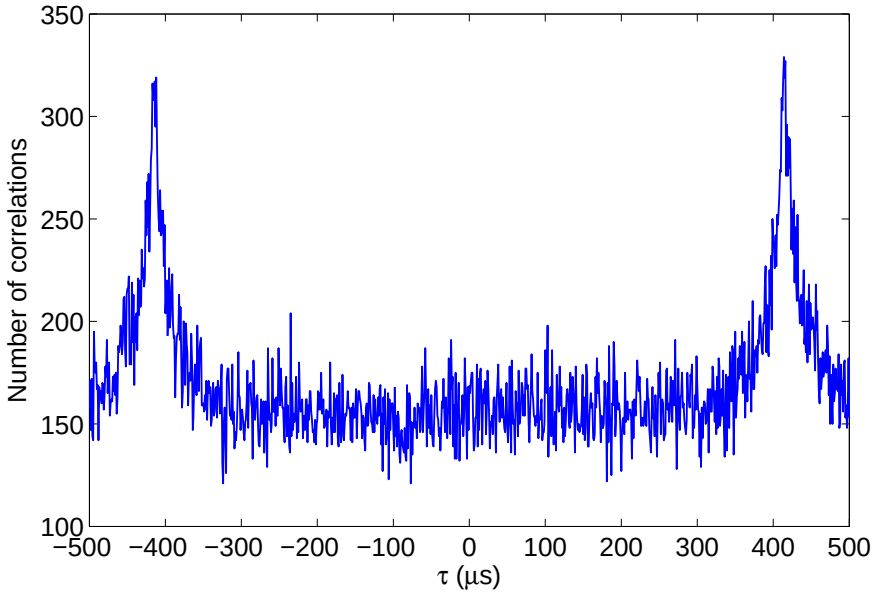

Figure 6.4: Histogram of correlations between photon detection events for the same data set used in figure 6.3 but without normalization and background subtraction and for a smaller bin size of 1 μs and a shorter time window.

detector. These reflected photons are confined to a 20 ns window, which is removed from the data and the empty window is replaced by an average over the values of the adjacent time windows [65].

6.2.2 Temporal pulse shape of the cavity photon

In order to evaluate the pulse shape of the photon exiting the cavity, we generate a histogram of the time intervals between the start of the drive pulse and detection of a photon. This histogram is then normalized by the number of trials, and the resulting probability distribution of photon arrival times per time bin is shown in figure 6.5. The total area of $\eta_{exp} = 0.045$ under the curve thus represents the probability to detect a photon in the course of a single trial. From our previous measurement of the detection efficiency, we calculate a photon creation efficiency of $\eta_c = \eta_{exp}/\eta_{det} = (88 \pm 17)\,\%$.

Also shown in figure 6.5 is the result of a master-equation simulation of the eight-level $^{40}Ca^{+}$ ion and two orthogonal cavity modes, each with a truncated basis of three Fock states. Linewidths of the atom, cavity and drive field are included as decoherence channels in the Liouvillian, as described in chapter 3. We perform independent calibration measurements for all parameters, including magnetic field

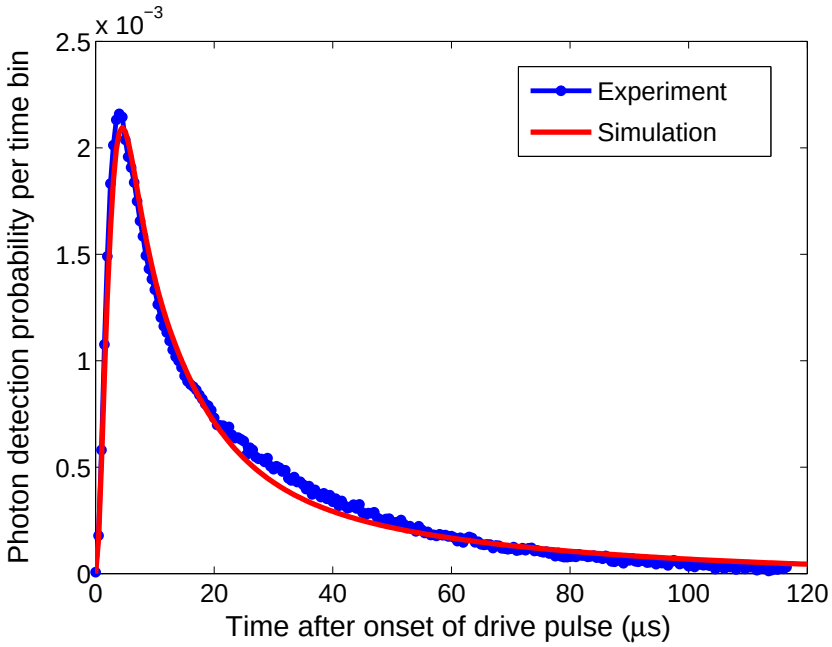

Figure 6.5: Temporal pulse shape of the cavity photons on the time window of the drive pulse: experimental data (blue dots) and theoretical prediction (red line). It represents the probability distribution of photon arrival times per time bin. The total area under this curve ($\eta_{exp} = 0.045$) provides the probability to detect a photon in a single trial.

and Rabi frequency, detuning and linewidth of the drive field, according to the calibration method described in section 5.1. In order to find the best agreement with the data, we then adjust three of these parameter values within the error range of their calibrated values.

Specifically, we use a Rabi frequency of the drive field $\Omega_d = 2\pi \times 30\,\mathrm{MHz}$, given our calibrated value of $2\pi \times (40 \pm 10)$ MHz. Second, the cavity and drive laser frequencies are initially set to meet the Raman resonance condition, but over the course of several hours of data acquisition, their relative detuning drifts by a few hundreds of kHz. It is not realistic to reproduce this drift in our simulations, and we instead use an average detuning value of $2\pi \times 60\,\mathrm{kHz}$. Finally, the measured probability to detect a photon in the course of one trial, given by $\eta_{exp} = 0.045$, is taken into account in the simulation result by appropriate scaling of the amplitude. This scaling allows us to infer an output path efficiency of 6.1 %, consistent with $\eta_{det} = (5.1 \pm 1.0)\,\%$ (derived in subsection 4.6.2). For the parameters used in figure 6.5, we extract a photon creation efficiency of 74 %, consistent with the experimentally determined value $\eta_c = (88 \pm 17)\,\%$.

This photon creation efficiency is approximately three times greater than our previously measured single photon creation efficiency of 32 % reported in [65]. This

improvement is mainly attributed to the narrower linewidth of the drive laser, which is here reduced by a factor of ten in comparison to our previous work. Furthermore, the current efficiency represents a tenfold improvement over previous cavity-ion sources reported in the literature [109].

The theoretical curve of the temporal pulse shape of the cavity photon is very sensitive to input parameters. The strong agreement between experiment and simulation thus suggests that the simulations provide a realistic model of the complex dynamics of the atom-cavity system. Consequently, we can use the simulations to gain insight about the rate of relative cavity stimulated and spontaneous photon emission.

Table 6.1 summarizes the mains characteristics of our highly-efficient single-photon source.

Characteristics	Value
Photon creation efficiency	$\eta_c = (88 \pm 17)\,\%$
Number of single-photon events	$581\,000 \pm 2\,000$
Number of two photon events	150 ± 150
Repetition rate	2.4 kHz

Table 6.1: Main characteristics of our high-efficiency single-photon source.

6.2.3 Temporal evolution of the atomic populations

The simulations also provide important information about the temporal evolution of the atomic populations. Before the photon generation sequence begins, we initialize the ion in the $\left|S_{1/2}, +1/2\right\rangle$ sublevel. We then introduce the drive pulse, which is tuned to Raman resonance with the sublevel $\left|D_{3/2}, -1/2\right\rangle$, in order to initiate population transfer between the two states. However, due to spontaneous scattering from the excited $P_{1/2}$ manifold to the $S_{1/2}$ and $D_{3/2}$ manifolds, and to a lesser extent to off-resonant Raman transfer, population also accumulates in the remaining four $S_{1/2}$ and $D_{3/2}$ sublevels. This process is shown in figure 6.6, which plots the $S_{1/2}$ and $D_{3/2}$ populations as a function of time during the interval when the drive pulse is active.

In figure 6.6(a), the population in the initial state $\left|S_{1/2}, +1/2\right\rangle$ is seen to decrease with time as expected. In addition, a small fraction of population is transferred to the $\left|S_{1/2}, -1/2\right\rangle$ state, reaching a maximum within approximately 20 µs, after which the state slowly depopulates. This population results from a Raman scattering process in which the excited state $P_{1/2}$ is off-resonantly driven. Rayleigh scattering back to the initial $\left|S_{1/2}, +1/2\right\rangle$ state is also possible, so that the intended

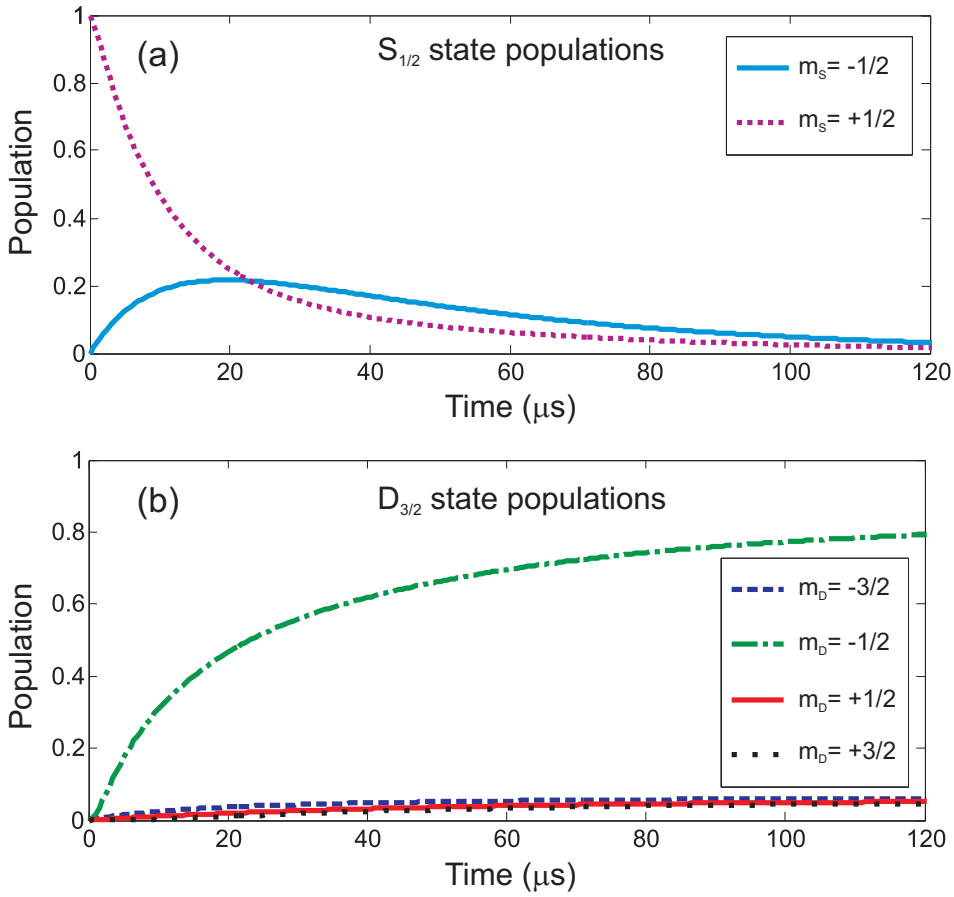

Figure 6.6: Temporal distribution of populations in the $S_{1/2}$ (a) and $D_{3/2}$ (b) manifolds in the time window of the drive pulse. The effects of the Raman process on the ion is here observed via a decrease on the population of the initial sublevel $\left|S_{1/2}, +1/2\right\rangle$ and an increase on the population of the final sublevel $\left|D_{3/2}, -1/2\right\rangle$. This figure also shows population in the other sublevels of the $S_{1/2}$ and $D_{3/2}$ manifolds, credited mainly to off-resonant scattering from the $P_{1/2}$ manifold.

process of Raman transfer to the $D_{3/2}$ manifold may only occur after multiple scattering events on the $S_{1/2} \leftrightarrow P_{1/2}$ transition.

In figure 6.6(b), the corresponding accumulation of population in the four $D_{3/2}$ sublevels is plotted. (Note that the fractional population in the two $P_{1/2}$ sublevels remains negligible, that is, on the order of 10^{-4} and is therefore not shown.) We emphasize that the laser-cavity Raman transition is indeed the dominant process, and the population of the $\left|D_{3/2}, -1/2\right\rangle$ state reaches approximately 80 % at the end of the pulse interval. The populations of the three remaining $D_{3/2}$ sublevels are primarily due to spontaneous decay from the upper state $P_{1/2}$. Also, the excited state decay to the target state $\left|D_{3/2}, -1/2\right\rangle$ is responsible for 6 % of its final population, in addition to the 74 % reported earlier, attributed to the photon generation process.

These dynamics are highly sensitive to input parameters and have thus guided our selection of appropriate experimental values as well as our understanding of the limits of the apparatus. For example, we have seen that the narrow linewidth of our drive field, a technical upgrade presented in this thesis, results in a significant improvement in photon generation efficiency. In addition, we have selected the Rabi frequency and detuning of our drive field in order to work in a regime of high photon generation efficiency. While in principle a smaller effective Rabi frequency for the Raman transition would further increase the efficiency, the process would in this case become too sensitive to previously mentioned frequency drifts in the laboratory.

6.3 Discussion

We have demonstrated a highly efficient ion-cavity single-photon source and characterized its output pulse shape and dark-count-limited suppression of two photon events. In comparison to state-of-the-art sources based on neutral atoms [61, 62], we operate at a slower repetition rate (2.4 kHz versus 100 kHz) due to a longer cavity and weaker coupling parameters; however, our photon generation efficiency of $(88 \pm 17)\,\%$ and detection efficiency of $(5.1 \pm 1.0)\,\%$ are comparable with the best reported values of $(115 \pm 18)\,\%$ and $(2.4 \pm 0.4)\,\%$ respectively [61]. For single-photon sources consisting of ions in free space [59, 60], the detection efficiency is significantly lower due to poor collection of the emitted photons. Furthermore, such systems rely on spontaneous emission and therefore can not generate single photons in a deterministic fashion.

The single-photon source presented in this chapter offers the prospect for coherent state transfer between atoms and photons within a quantum network. Nonetheless, the obstacles that realistic experimental parameters present for this transfer process must be considered. The simulations of section 6.2.3 represent an important step in this direction, as they allow us to analyze processes which would destroy coherence during photon generation. Consider, for example, the Raman and Rayleigh scattering processes which may occur between the $P_{1/2}$ and $S_{1/2}$ manifolds. The results presented on references [110, 111] have shown that while Raman scattering events introduce decoherence to the system, coherence may be preserved during Rayleigh scattering, which returns the atom to its initial state. From this perspective, it is interesting to evaluate the percentage of photons generated in the cavity without Raman scattering.

We can explore this situation by modifying our simulation to include an artificial, ninth atomic level, accessed only through rapid decay from the state

$\left|S_{1/2}, -1/2\right\rangle$; the new level thus functions as a dark state which collects any population that undergoes Raman scattering. By comparing the modified simulation to the original, we find that 70.3 % of cavity photons are produced without preceding Raman scattering event.

Moreover, we anticipate that we can increase this fraction by truncating the length of the drive pulse (for the same Rabi frequency). This is suggested by figure 6.6(a): the $\left|S_{1/2}, -1/2\right\rangle$ population accumulates slowly, and its long tail is due to events where the ion must wait for another scattering event before it can undergo Raman transfer from the $\left|S_{1/2}, +1/2\right\rangle$ state. Hence, by eliminating later events, we suppress the generation of photons for which the ion has undergone Raman scattering, at the cost of a reduction in photon generation efficiency. To confirm this, we truncate the drive pulse in our simulation by a factor of ten, so that it has a length of 12 µs. In this case, while the simulated photon generation efficiency drops from 74 % to 30 %, we find that 98.3 % of the cavity photons are created without Raman scattering. Although our current experiments do not involve coherence between initial states of the ion, we find these results promising for future efforts in which the ion is prepared in a superposition state, with the goal of deterministic state transfer to a photon.

7 Towards ground state cooling and coherent manipulation

This chapter is dedicated to the study of the ground state cooling and coherent manipulation of the $^{40}Ca^{+}$ ion using the quadrupole transition $S_{1/2} \leftrightarrow D_{5/2}$ [83]. The excited state is long-lived: the transition is narrow (lifetime of one second) and can be excited via the use of the few Hz linewidth laser described in section 4.3.4. This laser allows us to access not only carriers (electronic transitions that do not involve a change in the motional quantum number) but also the corresponding motional sidebands of the ion in the trap. This way, we can use this laser to sideband-cool the ion to lower motional states, ultimately achieving the ground state of motion.

This quadrupole transition has been extensively studied [92, 97, 112] in the context of Cirac-Zoller [113] based quantum computation experiments and is therefore not described in details here. This chapter is rather focused on the experimental results obtained with our system in a first step to combine quantum computing and cavity QED. In particular, the possible accessed transitions are identified using spectroscopy measurements. Rabi oscillations as well as Ramsey fringes are explored for different carrier transitions. Furthermore, preliminary results on sideband cooling using the 729 nm quadrupole laser are presented. The current problems encountered while exploring this transition are discussed as well as a description of how to stabilize the laser to the ion is given, followed by a brief summary and outlook of this chapter.

It is important to point out that all the results presented here were obtained when the high-finesse cavity around the ion was not locked. We believe that the cavity transfer-lock laser could ultimately cause an AC Stark shift and make the addressing of this quadrupole transition more challenging, although no such effect has been observed in the preliminary experiments performed so far.

7.1 Quadrupole transition spectrum

In chapters 2 and 3, the interaction of an electric dipole moment with an electric field was described, where the Hamiltonian of interaction is directly related to the electric field. In the case of a quadrupole moment Q, however, the interaction with an electric field occurs via its gradient ∇E as follows

$$\hat{\mathcal{H}}_{IQ} = Q\nabla\mathrm{E}. \tag{7.1}$$

For this quadrupole interaction, the selection rules allow transitions for which the change in the magnetic quantum number is $\Delta m = 0,\ 1,\ 2$.

The quadrupole transition can be investigated in a spectroscopy experiment in which the probability of excitation of the quadrupole transitions is observed as a function of the frequency of the 729 nm laser addressing these transitions. The experiment has been realized in a pulsed fashion using the pulse scheme drawn in figure 7.1.

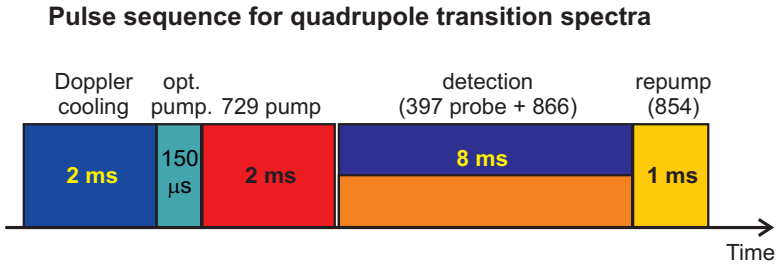

Figure 7.1: Pulse sequence used to obtain the quadrupole transition spectra presented in this section.

The sequence starts with a Doppler cooling pulse of 2 ms, which reduces the motion of the ion, followed by an optical pumping pulse of 150 µs to prepare the ion in the initial state $\left|S_{1/2}, +1/2\right\rangle$. A 2 ms long 729 nm pump pulse is then applied to excite the quadrupole transitions. The frequency of this laser is the parameter varied throughout the experiment to address different lines of the spectrum.

The ion's state is then read out by employing an electron shelving technique. Applying light at 397 nm and thereby driving the $S_{1/2} \leftrightarrow P_{1/2}$ transition causes a $S_{1/2} \leftrightarrow D_{5/2}$ superposition to collapse and project the ion onto either the $S_{1/2}$ or $D_{5/2}$ state. In case of projection onto the $S_{1/2}$ state, the ion interacts with the light at 397 nm and resonance fluorescence can be detected, while in the case of projection onto the $D_{5/2}$ state no fluorescence can be detected. Therefore by detecting the presence or absence of the strong fluorescence signal at 397 nm the ion's state after projection can be determined [92, 112]. During this detection process, an

866 recycling pulse is applied to repump the ion from the $D_{3/2}$ manifold.

After this detection stage, a 1 ms recycling pulse at 854 nm brings the population from the metastable $D_{5/2}$ manifold via the $P_{3/2}$ manifold back to the initial $S_{1/2}$ manifold. Repeating the experiment typically 100 times under the same condition establishes an excitation probability

Peaks in the spectrum can be understood using a simplified model in which the motion of a two-level atom (energy $\hbar\omega_a$ between the two levels) is described by a harmonic oscillator (quanta of energy $\hbar\omega_m$), as pictured in figure 7.2. In this model, carriers are transitions of the type $\left|S_{1/2}\right\rangle|n\rangle \leftrightarrow \left|D_{5/2}\right\rangle|n\rangle$, which preserve the number n of phonons in the system. First order sidebands are transitions changing the motional quantum number by one, being red sidebands if they subtract one phonon from the atom ($\left|S_{1/2}\right\rangle|n\rangle \leftrightarrow \left|D_{5/2}\right\rangle|n-1\rangle$) or blue sidebands if they add one phonon to the atom ($\left|S_{1/2}\right\rangle|n\rangle \leftrightarrow \left|D_{5/2}\right\rangle|n+1\rangle$).

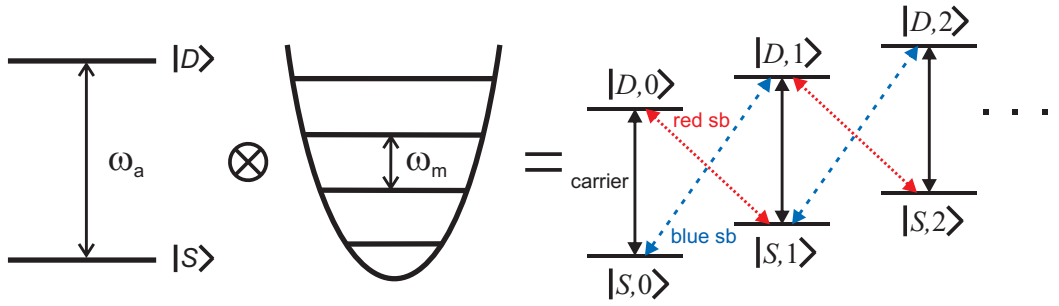

Figure 7.2: Picture describing a system composed of a two-level atom and quanta of motion represented by a harmonic oscillator. Arrows in the combined atom-phonon level system on the right side of this figure indicate carrier (black continuous arrows), red sideband (red dotted arrows) and blue sideband (blue traced arrows) transitions.

Selection rules allow ten possible quadrupole transitions between the $S_{1/2}$ and the $D_{3/2}$ manifolds, divided equally between the two initial $S_{1/2}$ sublevels. The energy separation between carriers can be calculated using the formula 3.5. The g-factor for the $S_{1/2}$ manifold is $g_S = 2$ and for the $D_{5/2}$ manifold is $g_{D_{5/2}} = 6/5$. Figure 7.3 shows the carrier and sidebands of the transition $\left|S_{1/2}, +1/2\right\rangle \leftrightarrow \left|D_{5/2}, -3/2\right\rangle$ obtained at a magnetic field of 0.203 mT. The axial sidebands are about 1.12 MHz apart from the carrier whereas the radial sidebands are approximately 2.9 MHz away from it.

In the regime where the atom's wavefunction is much smaller than the wavelength of the exciting field, the so-called Lamb-Dicke regime ($\eta^2(2n+1) \ll 1$), the Rabi frequency assumes the form

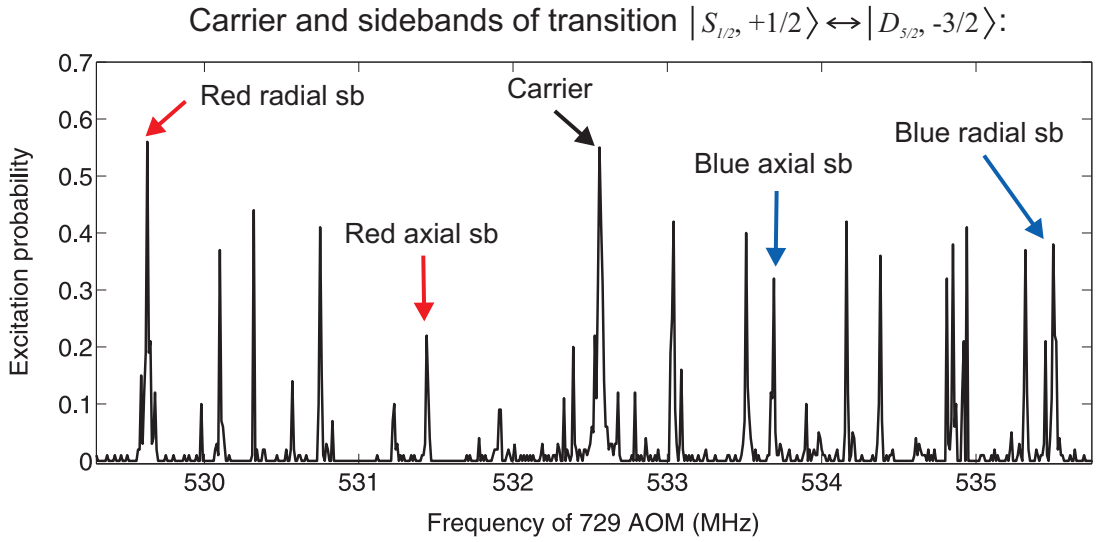

Figure 7.3: Spectrum of one quadrupole transition. Carrier and sidebands of the transition $\left|S_{1/2}, +1/2\right\rangle \leftrightarrow \left|D_{5/2}, -3/2\right\rangle$ obtained using the 729 nm laser at a magnetic field of 0.203 mT, in the presence of optical pumping, are identified. The additional peaks are attributed to first or higher order sidebands of other transitions.

$$\Omega_{n,n-1} = \Omega\sqrt{n}\eta \tag{7.2}$$

for red sideband transitions, and

$$\Omega_{n,n+1} = \Omega\sqrt{n+1}\eta \tag{7.3}$$

for blue sideband transitions. The quantity Ω represents the Rabi frequency on the carrier transition $\left|S_{1/2}\right\rangle|n\rangle \leftrightarrow \left|D_{5/2}\right\rangle|n\rangle$. The parameter $\eta = k\cos\theta\sqrt{\frac{\hbar}{2m\omega}}$ is the so-called Lamb-Dicke parameter and it is related to the applied light field angular frequency ω and wave vector k, incident at an angle θ with the ion oscillation axis, and to the mass of the ion m.

The transition and laser linewidths are here so narrow that allows us not only to distinctly address the axial and radial sidebands of secular motion but also to resolve the two close-to-degenerate radial sidebands. This can be more clearly verified in figure 7.4, where the two blue radial sidebands associated with the $\left|S_{1/2}, +1/2\right\rangle \leftrightarrow \left|D_{5/2}, +5/2\right\rangle$ carrier transition are shown. As can be seen in this figure, these two sidebands are separated by 60 kHz. Their size asymmetry might be due to geometry deviations from the idealized configuration depicted in subsection 4.5.2 but has not been thoroughly investigated so far.

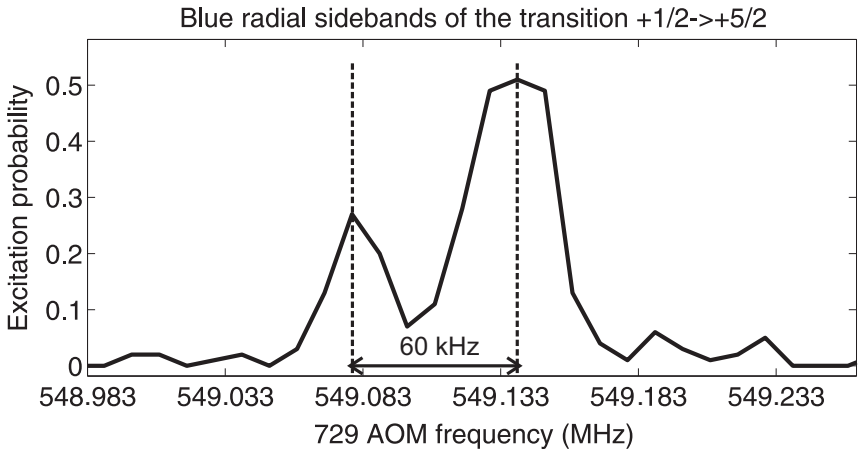

Figure 7.4: Spectrum of the blue radial motional sidebands of the ion in the trap associated with the carrier transition $\left|S_{1/2}, +1/2\right\rangle \leftrightarrow \left|D_{5/2}, +5/2\right\rangle$.

7.2 Rabi oscillations

As described in chapter 2, when laser light is applied to a two-level atom, the atomic population cycles between the two levels according to the pulse area $\int \Omega(t)dt$, performing the so-called Rabi oscillations. One Rabi cycle is given by the time the atom takes to come back to the initial state and the inverse of this cycle period times 2π corresponds to the Rabi frequency Ω.

Measurements of Rabi oscillations of different carriers of the $S_{1/2} \rightarrow D_{5/2}$ transition have been performed and figure 7.5 pictures them on the $\left|S_{1/2}, +1/2\right\rangle$ to the $\left|D_{5/2}, +5/2\right\rangle$ carrier. The experiment is realized by measuring the average over 100 experiments of the excitation probability for a certain pump laser frequency as a function of the pump pulse length. The pulse sequence used in this experiment is similar to the one presented in figure 7.1, but now the parameter being varied is the temporal length of the pump pulse.

The decoherence mechanism causing the decay of the Rabi oscillations is usually attributed to the motion of the ion [112]. The function[1]

$$y = \frac{1}{2}\left\{1 - \frac{[\cos(2\Omega t) + 2\eta^2 n\Omega t \cdot \sin(2\Omega t)]}{1 + (2\eta^2 \bar{n}\Omega t)^2}\right\} \tag{7.4}$$

was used to fit the Rabi oscillations presented in figure 7.1. The parameter n is related to the average number of phonons in a particular motional mode as follows[2]

[1] This function was obtained from a fitting program developed by Christian Roos [112].

[2] For this calculation we have assumed that the axial and radial potential wells are populated to the same depth, that is, $\bar{n}_{radial} = \bar{n}_{axial}\omega_{axial}/\omega_{radial}$, where ω_{axial} and ω_{radial} are the angular frequencies of the secular motion on the axial and radial directions of the trap.

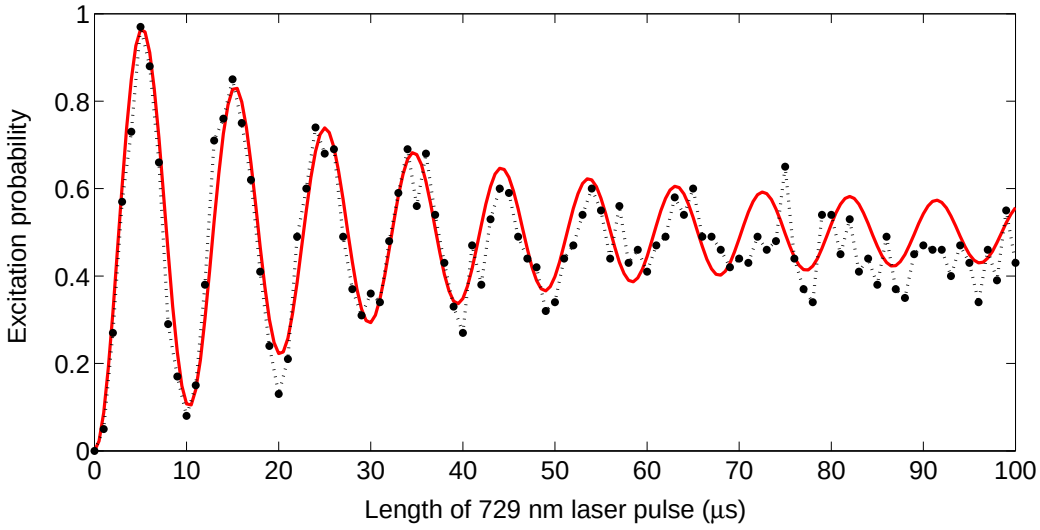

Figure 7.5: Rabi oscillations on the $\left|S_{1/2}, +1/2\right\rangle \rightarrow \left|D_{5/2}, +5/2\right\rangle$ carrier without sideband cooling.

$$n = (\eta_{axial}^2 \bar{n}_{axial} + 2\eta_{radial}^2 \bar{n}_{radial})/\eta^2, \tag{7.5}$$

where $\bar{n}_{axial}$ and $\bar{n}_{radial}$ are the average phonon numbers of the axial and radial modes, respectively, and η_{axial} and η_{radial} are the respective Lamb-Dicke parameters for each of these modes. These average number of phonons associated to each motional mode can be extracted from the fit to the experimental data and for figure 7.5 are $\bar{n}_{axial} = 23$ for the axial mode and $\bar{n}_{radial} = 8$ for the radial ones. The value of $\Omega = 668\,\mathrm{kHz}$ for the Rabi frequency has also been extracted from the fit parameters.

Although this data has been obtained without sideband cooling, preliminary experiments with sideband cooling of the axial mode showed no substantial improvement in the coherence time. This indicates that other motional modes are highly populated or other decoherence mechanisms are dominating.

7.3 Ramsey experiments

Figure 7.6 depicts the basic pulse scheme of a Ramsey experiment, in which two $\pi/2$ pulses are applied on a carrier transition with particular phases Φ_1 and Φ_2, separated by a certain waiting time t_R called Ramsey time.

The initial $\pi/2$-carrier laser pulse applied to the ion generates a superposition state $(|S\rangle + i\,|D\rangle)/\sqrt{2}$. If no relative phase shift between the phase of the laser and

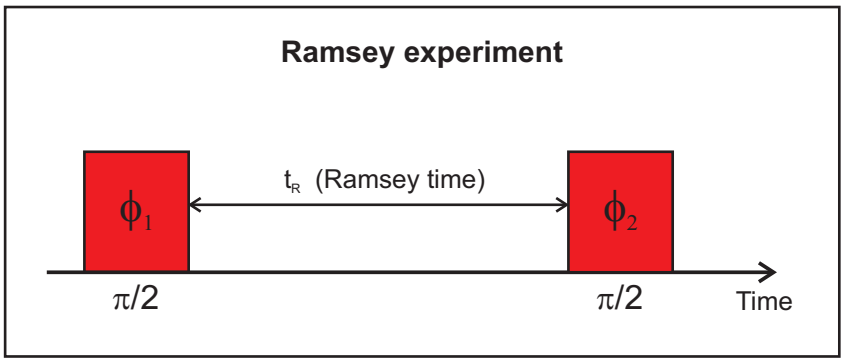

Figure 7.6: Schematic drawing of a Ramsey experiment.

the phase of the atomic superposition is induced, the second $\pi/2$-pulse transfers the ion to the $|D\rangle$-state, resulting in an excitation probability of one.

Ramsey interference fringes can be measured in experiments in which the phase Φ_2 of the second pulse is varied. The variation of this phase corresponds in the Bloch sphere picture to a variation of the chosen rotation axis in the equatorial plane, which causes an oscillation of the D-state excitation probability [77, 92]. The contrast of the Ramsey fringes relies on the phase coherence of the atomic superposition generated by the first Ramsey pulse. This phase coherence decreases with time and the longer the Ramsey time the smaller the contrast of the fringes. The outcome of these experiments vary according to changes in the magnetic field and frequency of the laser used for the Ramsey pulses, which introduce a phase shift in the interference pattern. The measurement of these shifts then allows us to use Ramsey experiments as a tool to correct for drifts of the 729 nm laser frequency and the magnetic field. With the information obtained from such experiments, it is possible to feedback correction signals to the system and to compensate for slow drifts in these two experimental parameters, as discussed in the next section.

Figure 7.7 shows Ramsey fringes on the $\left|S_{1/2}, +1/2\right\rangle$ to the $\left|D_{5/2}, +1/2\right\rangle$ transition for Ramsey times of 100 µs (red traced line), 200 µs (blue continuous line) and 400 µs (black traced-dotted line). In these experiments, the probability of exciting the ion to the $D_{1/2}$ manifold is measured as a function of the phase of the second Ramsey pulse.

Each point of these curves represents an average over 100 equal experiments performed one after the other. The three different curves were obtained in sequence of growing Ramsey times, with intervals of less than five minutes between consecutive plots. The contrast of the fringes decreases from 98 % for $t_R = 100$ µs to approximately 85 % for $t_R = 400$ µs due to decoherence mechanisms. A comparison between these curves shows horizontal displacements as well as differences in the

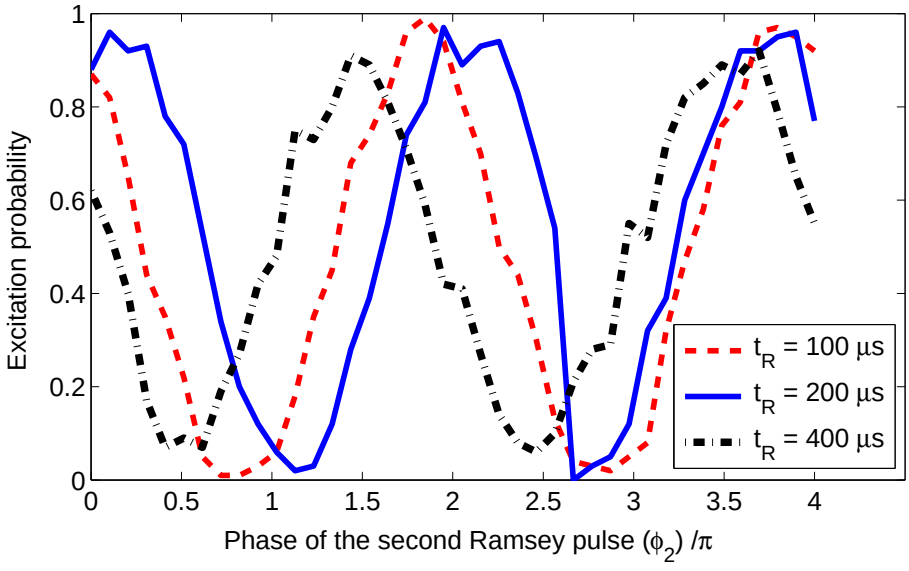

Figure 7.7: Ramsey fringes on the $\left|S_{1/2}, +1/2\right\rangle \leftrightarrow \left|D_{5/2}, +1/2\right\rangle$ transition for Ramsey times of 100 µs (red traced line), 200 µs (blue continuous line) and 400 µs (black traced-dotted line), with associated contrasts of 98 %, 95 % and 85 %, respectively.

periodicity of each curve with respect to each other. These features can be caused by mainly three reasons: instability of the 729 laser frequency, fluctuations in the magnetic field or uncertainties in the phase of the Ramsey pulses.

The stability of the laser frequency in the experimental setup has been confirmed via a beat measurement with stabilized reference light, showing a FWHM linewidth of around 400 Hz for the light going to the ion. Measurements of the magnetic field outside the chamber have exhibited a magnetic field noise of approximately 0.3 µT in amplitude on average, presenting random spikes that could sometimes be correlated to shifts in Ramsey experiments when both measurements were running simultaneously. This leads to the conclusion that magnetic field fluctuations around the apparatus limit the coherence in Ramsey experiments. The third possible cause of these shifts in the Ramsey fringes, which is a phase uncertainty of the Ramsey pulses, has not been carefully investigated yet and can therefore not be excluded as contributor to the undesired changes in the Ramsey experiments. The changes in the outcome of the Ramsey experiments are fast and erratic and represent a problem in the use of the Ramsey experiments to implement corrections to drifts in the magnetic field and laser frequency, as discussed in the next section.

7.4 Lock of the laser to the ion

This section briefly describes the procedure used to stabilize the 729 nm laser to the ion and to use the measured magnetic field drifts to correct for addressing of the quadrupole transition. More information about this subject can be found in reference [114].

The locking procedure begins with the selection of two quadrupole transition carriers and the precise determination of their frequencies. In our case we have selected the $|S_{1/2}, +1/2\rangle \leftrightarrow |D_{5/2}, +1/2\rangle$ and $|S_{1/2}, +1/2\rangle \leftrightarrow |D_{5/2}, +5/2\rangle$ transitions, which differ in magnetic field sensitivity according to formula 3.1. Two Ramsey experiments are realized in each transition sequentially, for which the phase on the second Ramsey pulse differs from the first by π. If the laser frequency changes, the Ramsey fringes acquire a phase shift, and a comparison between the outcomes of these two experiments in one transition makes it possible to determine how much and in which direction the laser frequency has changed. Furthermore, the comparison between shifts in the two transitions allows us to extract the drift in the magnetic field, once each transition has a different magnetic field dependence. The current fast and unpredictable changes observed in the outcome of the Ramsey experiments used to infer drifts in the magnetic field and laser frequency hinder the feedback mechanism.

7.5 Sideband cooling on the quadrupole transition

One important application of the 729 nm laser is the implementation of sideband cooling, with possibility of bringing the ion to the ground state of motion. This is done by executing a sideband cooling stage in the pulse sequence, during which the 729 nm and 854 nm lasers are continuously on and the optical pumping and the 866 nm recycling lasers are pulsing [115]. A schematic drawing of this pulse sequence can be seen in figure 7.8.

The pulse sequence used for this experiment is the similar to the one used for the quadrupole transition spectra with the difference that a sideband cooling stage is added between the Doppler cooling and the optical pumping pulses. In this stage the 729 nm laser frequency is set to address the red axial sideband of motion associated with the $|S_{1/2}, +1/2\rangle \leftrightarrow |D_{5/2}, +5/2\rangle$ carrier and is, together with the 854 nm recycling laser, continuously on for 5.5 ms. In this same time interval, the optical pumping and the 866 nm recycling lasers are simultaneously pulsed seven times to assure that the atomic population returns to the initial state for sideband cooling. After the cooling stage, the 854 nm laser is switched off and spectroscopy

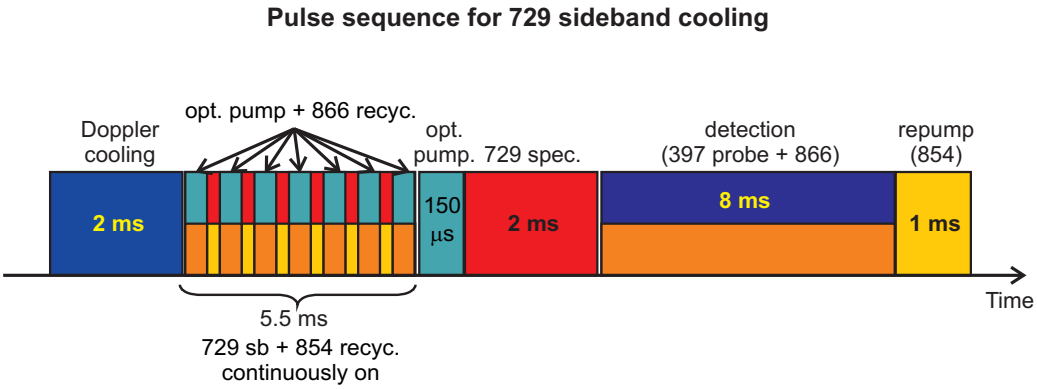

Figure 7.8: Pulse sequence of the 729 sideband cooling.

is performed using the 729 nm laser to probe the motional sideband.

The 729 nm and 854 nm lasers of the sideband cooling stage are depicted in the level scheme of figure 7.9(a). As the 729 nm laser is acting on the red axial sideband during this stage, its function is to take phonons out of the system, as depicted in the basic level scheme of figure 7.9(b). Each cycle in which the ion is excited by this 729 nm laser and recycled by the 854 nm laser removes one phonon from the system and successful repetitions of it allows for cooling to the motional ground state.

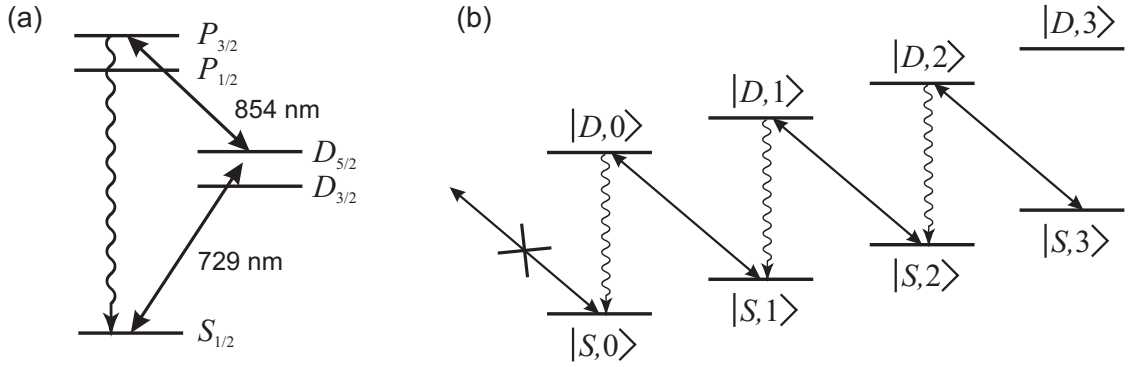

Figure 7.9: Scheme of sideband cooling: (a) calcium level scheme with the transition and lasers used for sideband cooling; (b) basic principle of sideband cooling.

The effects of sideband cooling on the ion can be seen when comparing frequency scans over the red sideband before and after sideband cooling was performed, shown in figure 7.10. The reduction of the red sideband after sideband cooling is evident, indicating a decrease in the number of axial phonons in the system. The two peaks at frequency shifts of around 2.5 kHz and 7.5 kHz observed in the blue dotted line of figure 7.10 are attributed to a brief heating of the ion during the detection process.

Furthermore, the blue sideband did not show any significant modification after

sideband cooling, as can be observed in figure 7.11. We have driven Rabi oscillations on the carrier for the cases with and without sideband cooling but no significant change in the decoherence time was observed, which indicates that other decoherence effects are dominating over the axial motion of the ion.

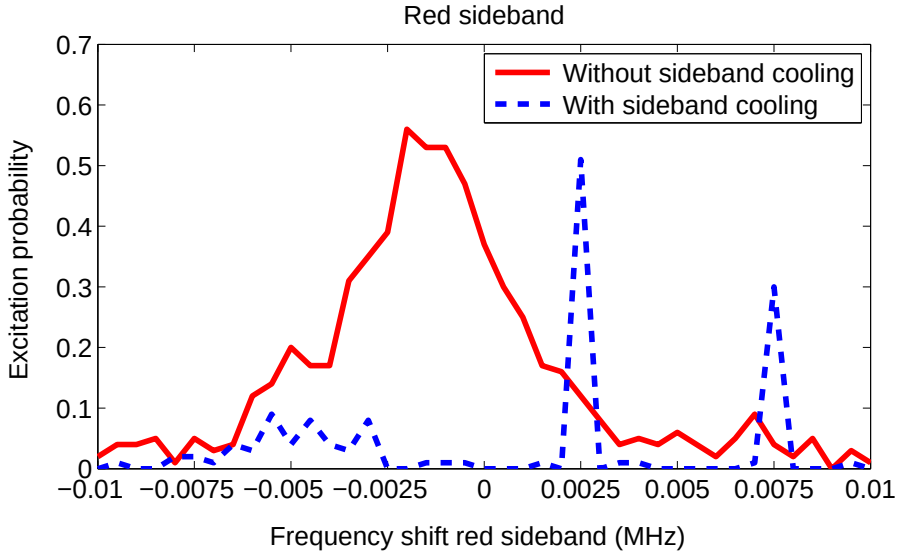

Figure 7.10: Spectra of the red sideband without (red continuous line) and with (blue dotted line) sideband cooling.

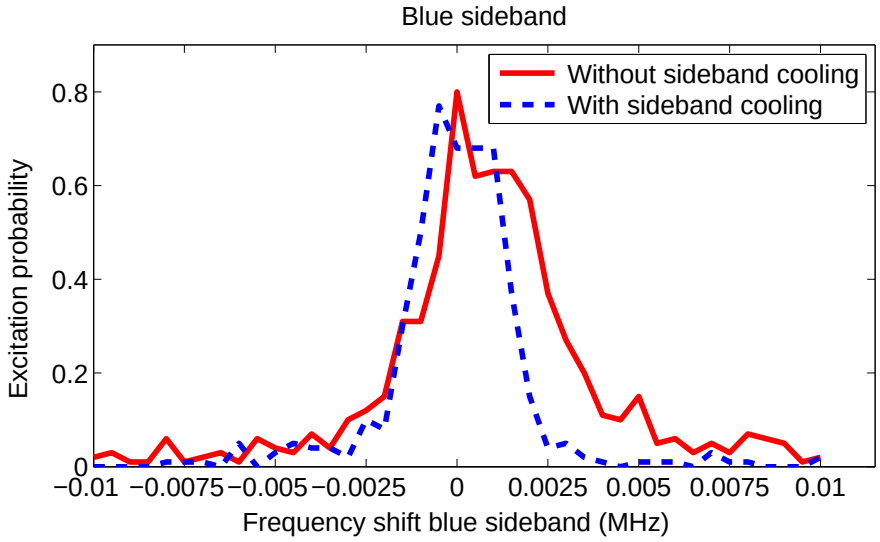

Figure 7.11: Spectra of the blue sideband without (red continuous line) and with (blue dotted line) sideband cooling.

7.6 Discussion

The purpose of this chapter was to show preliminary results on the quadrupole transition obtained in our setup. Although these type of experiments have already been explored in depth in other projects in our group, it is clear that such basic measurements are important for investigating our system's behavior under similar circumstances. The results shown provide information about issues like magnetic field noise and laser instability affecting our apparatus, which should be addressed to continue experiments towards coherent state manipulation and the implementation of quantum information processing protocols in our system.

The realization of entanglement between an ion and a cavity photon represents one of the future goals for this setup and depends on the reliable manipulation of the quadrupole transition. Furthermore, the achievement of the motional ground state via sideband cooling using the quadrupole laser will bring us a step closer to the realization of cavity-assisted sideband cooling, mentioned in chapter 5.

8 Summary and outlook

The work presented in this thesis involves two basic elements of quantum mechanics: single atoms and single photons. It has been shown here that a system composed of a single ion and a high-finesse optical cavity constitutes an excellent playground for state-of-the-art experiments in quantum optics. In particular, the study of their interaction opens up the possibility for studying both fundamental properties of the system as well possible applications in fields like quantum computation and quantum cryptography [11].

A theoretical description of the system has been provided and good agreement between simulation and experiment has been demonstrated. The possibility of simulating the system theoretically allows us not only to confirm our understanding of the system and attest our calibration measurements but also to design experiments and obtain from the simulations the correct parameters necessary to achieve our goals.

The investigation of Raman transitions through the observation of the cavity photons provided great insight into the behavior of our system. Spectroscopy measurements confirmed the predicted transition strengths and good agreement between experiment and theory ascertained the relevance of the theoretical model. The introduction of Doppler cooling on the Raman spectroscopy measurements permitted the distinction of all possible transitions as well as first order sidebands of the ion's secular motion. The distinction of these sidebands using cavity photons yields the possibility for performing cavity-assisted sideband cooling [108]. Experiments along these lines are currently on their way in our laboratory with prospects of cooling to the motional ground state.

High-efficiency and deterministic generation of single photons has been reported. Measurements of the second-order correlation function evidence the single-photon nature of the source, where the high suppression of two-photon events observed is limited by dark counts of the photodetectors. In these measurements, a photon creation efficiency of $\eta_c = (88 \pm 17)\,\%$ has been achieved. This represents a threefold improvement over our previous achievements [65] and a tenfold improvement over other cavity-ion single-photon sources reported in the literature [109].

Furthermore, this efficiency is also comparable to state-of-the-art experiments with single neutral atoms and high-finesse optical resonators [61, 62]. The creation of single photons represents a major achievement toward the realization of a deterministic light-matter interface for distributing quantum information.

The pioneering work on quantum computation protocols implemented by our group [116, 117] uses sublevels of the manifolds $S_{1/2}$ and $D_{5/2}$ of the $^{40}Ca^{+}$ion as the qubit states $|1\rangle$ and $|0\rangle$, respectively. In these realizations, the quantum information is transported between the ions via phonons, carefully manipulated via the use of a laser that addresses the quadrupole transitions between these two manifolds. Many experimental tools like sideband cooling, state preparation and state read-out have been developed using this narrow linewidth laser. The implementation of the quadrupole transition addressing in our apparatus has been reported here. Some initial results have been presented, which revealed technical issues that should be overcome for the full employment of the quadrupole transition laser. Preliminary sideband cooling measurements using this laser have been presented, where a significant reduction of the red axial motional sideband has been shown.

The results presented in this thesis summarize some of the important features of our ion-cavity system. The investigation and understanding of the Raman process and the possibility of addressing individual Raman transitions opens the way for both cavity-assisted sideband cooling and quantum information experiments. In both of these goals, the presence of the quadrupole transition laser is of extreme importance, either for the performance of ground state cooling or for state preparation and state read-out of the qubit. Ground state cooling of ions using cavity photons has never been realized and corresponds to the next experiment to be performed in our apparatus. More applied experiments would then follow, where the entanglement between a single ion and a cavity photon should be demonstrated. State mapping experiments transferring information from the ion to a cavity photon could come next, paving the road towards entanglement of two distant ions using cavity photons, which represents the ultimate goal of this experiment. The work developed here thus constitutes a step forward towards more complex fundamental and applied quantum optics experiments.

The next generation of such setups points towards the development of smaller, more scalable ion-cavity systems, with the vision of building a quantum computer where trapped ions store information and photons are the information bus. Many approaches are currently under development. Among these ideas are the implementation of fiber cavities [118] in miniaturized linear Paul traps, surface segmented traps [119–121] and endcap traps [119]. The next generation of the cavity QED

project is already under development with trapped ions in our group. Nonetheless, technology advances are still required to transform the challenge of unifying small cavities and miniaturized traps into daily reality.

Appendix A: Afterpulsing of the APDs

In this appendix, the so-called afterpulsing effect of the avalanche photodiodes is discussed and the measurements performed to quantify this feature in our devices are reported.

We have observed that our APDs experience after-pulsing, i.e., one detection event creates an electronic signal that presents a tail extending to a couple of μs. This effect can be seen in figure 8.1, where the auto-correlation of the detection events on the current APD0 and also on a new (fiber coupled) APD taken when their inputs were blocked are shown as a function of time delay between detection events. Similar results to the ones of APD0 were also obtained for the second APD in our setup (APD1), which completed the pair of APDs composing the HBT setup used in the experiments presented in this thesis.

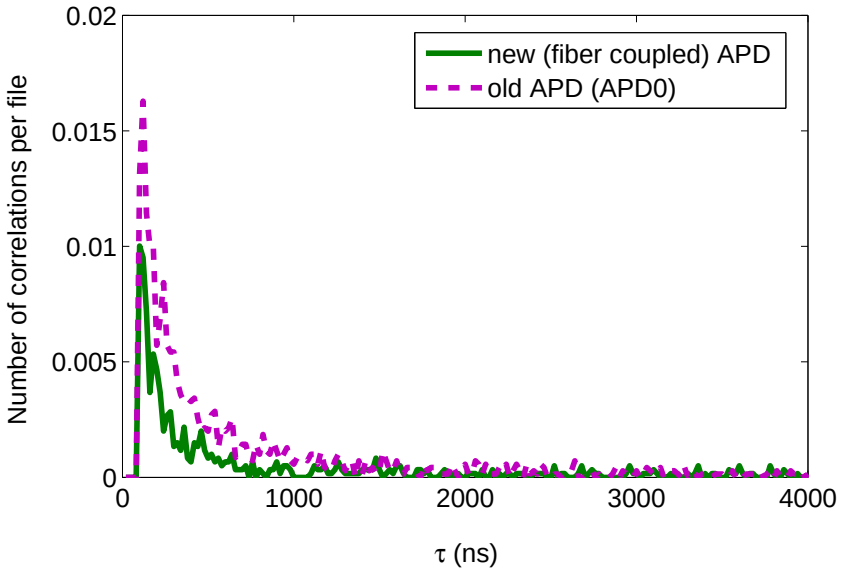

Figure 8.1: APD0 afterpulsing.

By integrating the number of counts presented in figure 8.1 in a certain time interval and dividing it by the total number of counts, the probability of detecting

an afterpulsing event in this determined time window is obtained. For the time window between 0 and 2.5 µs, these probabilities are of 0.9 % for the current APD0 and 0.22 % for the new APD.

To compensate for the afterpulsing, an artificial dead time has been introduced in the processing of the data presented in chapter 6.

Appendix B: Interferometric measurements of the mechanical stability of cavity and trap

Interferometric measurement results of the mechanical stability of both cavity and trap are reported in this appendix. These measurements were performed with the SP-S series laser interferometric vibrometer device from SIOS. The goal of these experiments was to measure how much mechanical noise both cavity and trap exhibited under different laboratory conditions.

The setup is based on a Michelson interferometer in which one arm consists of a beam back-reflected from the measured object. Its resolution is of 0.3 nm and the measured frequency can range from 0 to 500 kHz.

The measurement of the cavity mechanical noise was performed by sending this reference beam on the output cavity mirror mount in a diagonal direction, as shown in figure 8.2. A similar setup was also used for measuring the noise on the trap, by pointing to one of the trap blade electrodes.

The measurements were realized for different configurations of noise in the laboratory with the goal of identifying the noise sources in our setup. Three main noise sources are considered here: the laboratory air conditioner (AC), the flow boxes on top of the Doppler and detection 397 nm laser table (FB 397) and the flow box on top of the Raman 397 nm laser table (FB 393). Also the influence of the sound protection covers (SP) around our experiment is investigated here. The measurement results on the cavity output mirror can be seen in figure 8.3, where the mechanical oscillations are shown in nm as a function of time in ms. Here, the beige curve was taken when all noise sources are turned on and the sound protection covers are off and the blue plot was taken when all the noise sources are off and the sound protection covers are set in place.

As can be seen in figure 8.3, the worse situation presents an amplitude of movement of the cavity mirror of around 90 nm, whereas for the best case this amplitude was reduced to approximately 15 nm. Under normal experimenting situations, how-

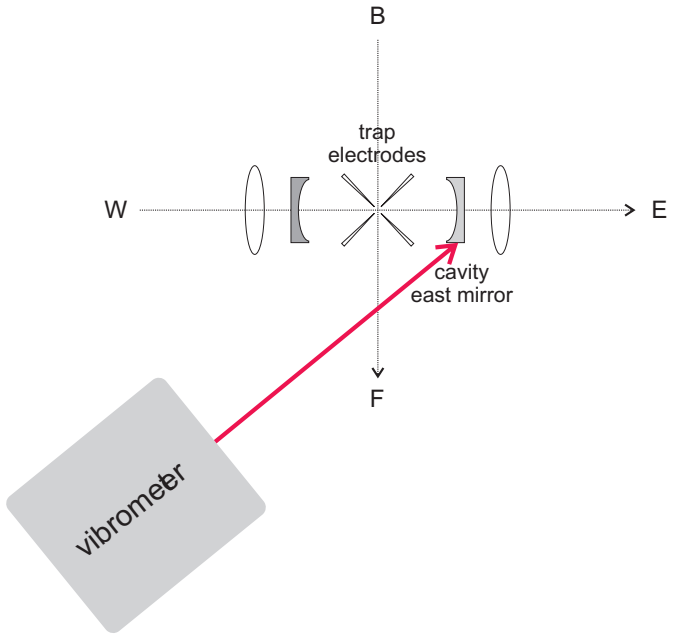

Figure 8.2: Experimental setup for measuring the mechanical noise of the cavity: vibrometer points towards the cavity output mirror.

ever, all noise sources are present and the sound cover is set in place, which leads to a measured noise amplitude of around 60 nm.

Similar measurements where performed on one of the trap blades. In contrast to the cavity mirror, the trap proved to be robust against external mechanical noises, as expected, keeping its fast oscillation amplitude below 40 nm for all laboratory conditions. The relative vibrations between the cavity mirror and the trap are relevant and could be investigated with a new version of the vibrometer that allows to use a probe and a reference beam.

In order to identify the sources of particular noise peaks in the cavity we have calculated the Fast Fourier Transform (FFT) of the amplitude measurements for cases in which only one of the noise sources was present. As can be seen in figure 8.4, the source of the noise at 100 Hz are the flow boxes above the Verdis and Ti:Sapphire laser tables. The devices responsible for the peak at 74 Hz are the air conditioning and the flow box on the 397 Raman laser table, located both in the back of the laboratory, about 4 meters away from our apparatus.

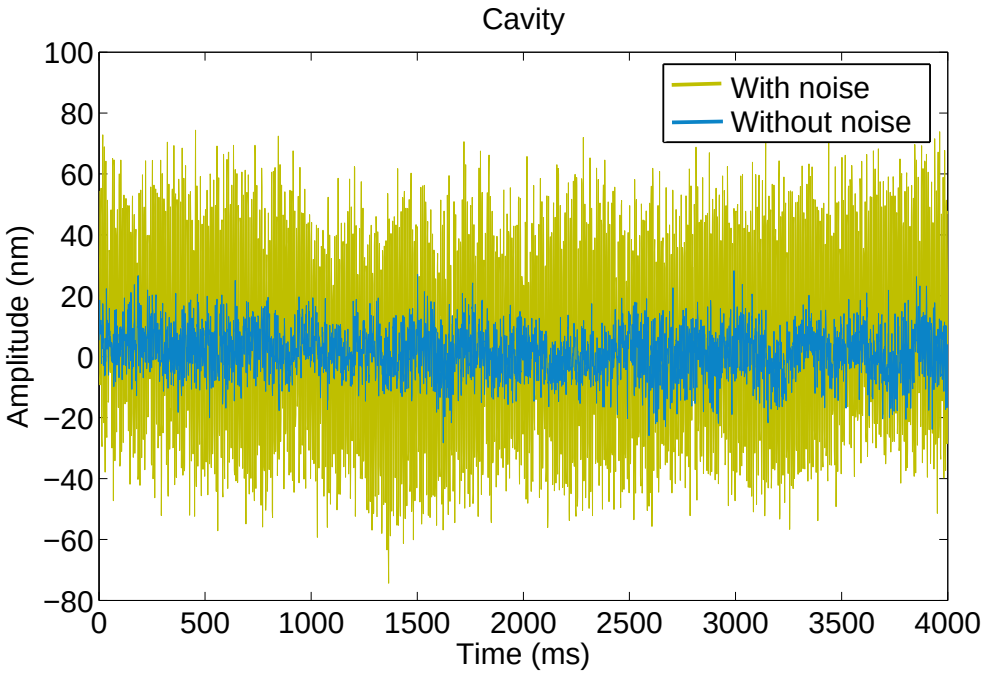

Figure 8.3: Amplitude of the mechanical noise on the cavity east mirror for the situations in which the noises in the laboratory where fully present or not.

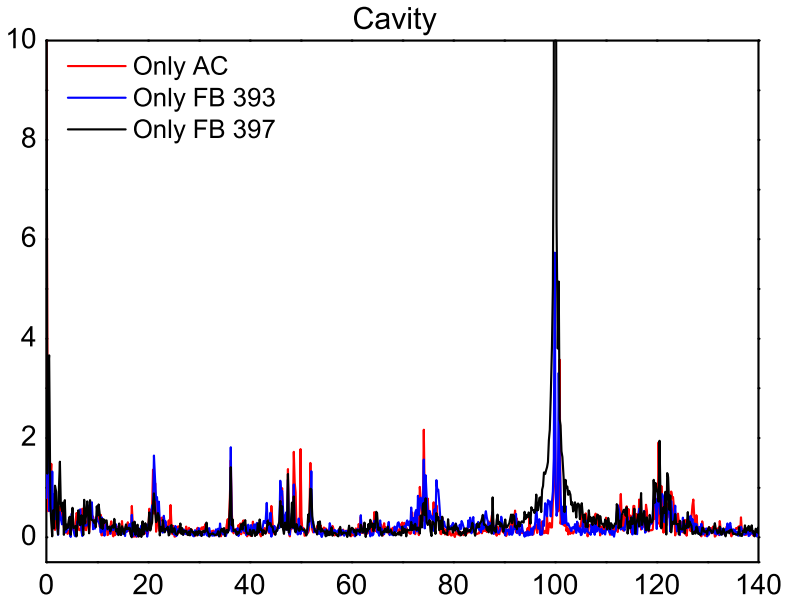

Figure 8.4: Spectrum of the cavity mechanical noise for three different situations where each main noise source is applied to the system individually.

Summarizing, the mechanical vibrations of cavity and trap have been measured for different noise configurations in the laboratory. We can see that the cavity is between two and three times more sensitive to the environmental noise than the trap. The three noise sources considered contribute to an increase of about 30 nm in the oscillation amplitude of the cavity mirror. The presence of the sound protection covers around our experiment attenuate these oscillations by approximately 30 nm. Furthermore, we can assume an amplitude of motion of around 60 nm of the cavity in normal experimenting configuration. This will lead to a decrease in the coupling constant between the ion and the cavity field, as discussed in chapter 5.

Bibliography

[1] A. Einstein, Ann. Phys. Lpz. **17**, 132 (1905). Cited in page(s): 1.

[2] A. Einstein, Ann. Phys. Lpz. **20**, 199 (1906). Cited in page(s): 1.

[3] A. Einstein, Ann. Phys. Lpz. **22**, 180 (1907). Cited in page(s): 1.

[4] A. Einstein, Ann. Phys. Lpz. **10**, 185 (1909). Cited in page(s): 1.

[5] A. Einstein, Ann. Phys. Lpz. **10**, 817 (1909). Cited in page(s): 1.

[6] E. M. Purcell, Phys. Rev. **69**, 674 (1946). Cited in page(s): 1.

[7] P. Goy, J. M. Raimond, M. Gross, and S. Haroche, Phys. Rev. Lett. **50**, 1903 (1983). Cited in page(s): 1.

[8] D. J. Heinzen, J. J. Childs, J. E. Thomas, and M. S. Feld, Phys. Rev. Lett. **58**, 1320 (1987). Cited in page(s): 1.

[9] D. J. Heinzen and M. S. Feld, Phys. Rev. Lett. **59**, 2623 (1987). Cited in page(s): 1.

[10] P. R. Berman, ed., *Cavity Quantum Electrodynamics* (Academic Press, 1994). Cited in page(s): 1 and 15.

[11] H. Walther, B. T. H. Varcoe, B. Englert, and T. Becker, Rep. Prog. Phys. **69**, 1325 (2006). Cited in page(s): 1 and 91.

[12] R. Miller, T. E. Northup, K. M. Birnbaum, A. Boca, A. D. Boozer, and H. J. Kimble, J. Phys. B **38**, S551 (2005), URL http://stacks.iop.org/0953-4075/38/S551. Cited in page(s): 1.

[13] H. J. Kimble, Phys. Scr. **76**, 127 (1998). Cited in page(s): 1.

[14] D. Meschede, Phys. Rep. **211**, 201 (1992). Cited in page(s): 1.

[15] J. M. Raimond, M. Brune, and S. Haroche, Rev. Mod. Phys. **73**, 565 (2001). Cited in page(s): 1.

[16] A. Wallraff, D. I. Schuster, A. Blais, L. Frunzio, R.-S. Huang, J. Majer, S. Kumar, S. M. Girvin, and R. J. Schoelkopf, Nature **431**, 162 (2004). Cited in page(s): 1.

[17] C. Weisbuch, M. Nishioka, A. Ishikawa, and Y. Arakawa, Phys. Rev. Lett. **69**, 3314 (1992). Cited in page(s): 1.

[18] J. Reithmaier, G. Sek, A. Loffler, C. Hofmann, S. Kuhn, S. Reitzenstein, L. Keldysh, V. Kulakovskii, T. Reinecke, and A. Forchel, Nature **432**, 197 (2004). Cited in page(s): 1.

[19] T. Yoshie, A. Scherer, J. Hendrickson, G. Khitrova, H. M. Gibbs, G. Rupper, C. Ell, O. B. Shchekin, and D. G. Deppe, Nature **432**, 200 (2004). Cited in page(s): 1.

[20] G. R. Guthöhrlein, M. Keller, K. Hayasaka, W. Lange, and H. Walther, Nature **414**, 49 (2001). Cited in page(s): 1 and 2.

[21] A. B. Mundt, A. Kreuter, C. Becher, D. Leibfried, J. Eschner, F. Schmidt-Kaler, and R. Blatt, Phys. Rev. Lett. **89**, 103001 (2002). Cited in page(s): 1 and 2.

[22] M. Keller, B. Lange, K. Hayasaka, W. Lange, and H. Walther, Appl. Phys. B **76**, 125 (2003). Cited in page(s): 1, 2, and 57.

[23] F. Bernardot, P. Nussenzveig, M. Brune, J. M. Raimond, and S. Haroche, Europhys. Lett. **17**, 33 (1992). Cited in page(s): 1.

[24] A. Boca, R. Miller, K. M. Birnbaum, A. D. Boozer, J. McKeever, and H. J. Kimble, Phys. Rev. Lett. **93**, 233603 (2004). Cited in page(s): 1.

[25] G. Rempe, H. Walther, and N. Klein, Phys. Rev. Lett. **58**, 353 (1987). Cited in page(s): 1.

[26] M. Brune, F. Schmidt-Kaler, A. Maali, J. Dreyer, E. Hagley, J. M. Raimond, and S. Haroche, Phys. Rev. Lett. **76**, 1800 (1996). Cited in page(s): 1.

[27] P. Münstermann, T. Fischer, P. Maunz, P. W. H. Pinkse, and G. Rempe, Phys. Rev. Lett. **82**, 3791 (1999). Cited in page(s): 2.

[28] C. J. Hood, T. W. Lynn, A. C. Doherty, A. S. Parkins, and H. J. Kimble, Science **287**, 1447 (2000). Cited in page(s): 2.

[29] C. Russo, H. Barros, A. Stute, F. Dubin, E. Phillips, T. Monz, T. Northup, C. Becher, T. Salzburger, H. Ritsch, et al., Appl. Phys. B (2009), published online. Cited in page(s): 2 and 53.

[30] T. Pellizzari, S. A. Gardiner, J. I. Cirac, and P. Zoller, Phys. Rev. Lett. **75**, 3788 (1995). Cited in page(s): 2.

[31] I. Cirac, P. Zoller, J. Kimble, and H. Mabuchi, Phys. Rev. Lett. **78**, 3221 (1997). Cited in page(s): 2.

[32] H.-J. Briegel, J. I. Cirac, W. Dür, S. J. van Enk, H. J. Kimble, H. Mabuchi, and P. Zoller, Quant. Comp. Quant. Comm. **1509/1999**, 373 (1998). Cited in page(s): 2.

[33] P. Zoller, T. Beth, D. Binosi, R. Blatt, H. Briegel, D. Bruss, T. Calarco, J. I. Cirac, D. Deutsch, J. Eisert, et al., Eur. Phys. J. D **36**, 203 (2005). Cited in page(s): 2.

[34] T. Wilk, S. C. Webster, A. Kuhn, and G. Rempe, Science **317**, 488 (2007), http://www.sciencemag.org/cgi/reprint/317/5837/488.pdf, URL http://www.sciencemag.org/cgi/content/abstract/317/5837/488. Cited in page(s): 2.

[35] A. D. Boozer, A. Boca, R. Miller, T. E. Northup, and H. J. Kimble, Phys. Rev. Lett. **98**, 193601 (pages 4) (2007). Cited in page(s): 2.

[36] H. Häffner, W. Hänsel, C. F. Roos, J. Benhelm, D. Chek-al-Kar, M. Chwalla, T. Körber, U. D. Rapol, M. Riebe, P. O. Schmidt, et al., Nature **438**, 643 (2005). Cited in page(s): 2.

[37] D. Leibfried, E. Knill, S. Seidelin, J. Britton, R. B. Blakestad, J. Chiaverini, D. B. Hume, W. M. Itano, J. D. Jost, C. Langer, et al., Nature **438**, 639 (2005). Cited in page(s): 2.

[38] R. Reichle, D. Leibfried, E. Knill, J. Britton, R. B. Blakestad, J. D. Jost, C. Langer, R. Ozeri, S. Seidelin, and D. J. Wineland, Nature **443**, 838 (2006). Cited in page(s): 2.

[39] J. Benhelm, G. Kirchmair, C. F. Roos, and R. Blatt, Nature Physics **4**, 463 (2008). Cited in page(s): 2.

[40] R. Blatt and D. Wineland, Nature **453**, 1008 (2008). Cited in page(s): 2.

[41] H. Häffner, C. F. Roos, and R. Blatt, Phys. Rep. **469**, 155 (2008), 0809.4368. Cited in page(s): 2.

[42] D. L. Moehring, P. Maunz, S. Olmschenk, K. C. Younge, D. N. Matsukevich, L.-M. Duan, and C. Monroe, Nature **449**, 68 (2007). Cited in page(s): 2.

[43] P. Maunz, S. Olmschenk, D. Hayes, D. N. Matsukevich, L. Duan, and C. Monroe, Phys. Rev. Lett. **102**, 250502 (2009), 0902.2136. Cited in page(s): 2.

[44] S. Olmschenk, D. Hayes, D. N. Matsukevich, P. Maunz, D. L. Moehring, and C. Monroe, ArXiv e-prints (2009), 0907.1702. Cited in page(s): 2.

[45] S. Olmschenk, D. N. Matsukevich, P. Maunz, D. Hayes, L. Duan, and C. Monroe, ArXiv e-prints (2009), 0907.5240. Cited in page(s): 2.

[46] C. Monroe, Nature **416**, 238 (2002). Cited in page(s): 2.

[47] E. Knill, R. Laflamme, and G. J. Milburn, Nature **409**, 46 (2001). Cited in page(s): 2.

[48] R. Raussendorf and H. J. Briegel, Phys. Rev. Lett. **86**, 5188 (2001). Cited in page(s): 2.

[49] N. Gisin, G. Ribordy, W. Tittel, and H. Zbinden, Rev. Mod. Phys. **74**, 145 (2002). Cited in page(s): 2.

[50] K. M. Gheri, K. Ellinger, T. Pellizzari, and P. Zoller, Fortschritte der Physik **46**, 401 (1998). Cited in page(s): 2.

[51] P. Grangier, B. Sanders, and J. Vuckovic, New Journal of Physics **6** (2004), URL http://stacks.iop.org/1367-2630/6/i=1/a=E04. Cited in page(s): 2.

[52] C. Brunel, B. Lounis, P. Tamarat, and M. Orrit, Phys. Rev. Lett. **83**, 2722 (1999). Cited in page(s): 2.

[53] B. Lounis and W. E. Moerner, Nature **407**, 491 (2000). Cited in page(s): 2.

[54] R. Brouri, A. Beveratos, J.-P. Poizat, and P. Grangier, Opt. Lett. **25**, 1294 (2000). Cited in page(s): 2.

[55] C. Kurtsiefer, S. Mayer, P. Zarda, and H. Weinfurter, Phys. Rev. Lett. **85**, 290 (2000). Cited in page(s): 2.

[56] C. Santori, M. Pelton, G. Solomon, Y. Dale, and Y. Yamamoto, Phys. Rev. Lett. **86**, 1502 (2001). Cited in page(s): 2.

[57] D. Press, S. Götzinger, S. Reitzenstein, C. Hofmann, A. Löffler, M. Kamp, A. Forchel, and Y. Yamamoto, Phys. Rev. Lett. **98**, 117402 (2007). Cited in page(s): 2.

[58] B. Darquie, M. P. A. Jones, J. Dingjan, J. Beugnon, S. Bergamini, Y. Sortais, G. Messin, A. Browaeys, and P. Grangier, Science **309**, 454 (2005), http://www.sciencemag.org/cgi/reprint/309/5733/454.pdf, URL http://www.sciencemag.org/cgi/content/abstract/309/5733/454. Cited in page(s): 2.

[59] P. Maunz, D. L. Moehring, S. Olmschenk, K. C. Younge, D. N. Matsukevich, and C. Monroe, Nature Physics **3**, 538 (2007). Cited in page(s): 2 and 76.

[60] M. Almendros, J. Huwer, N. Piro, F. Rohde, C. Schuck, M. Hennrich, F. Dubin, and J. Eschner, ArXiv e-prints (2009), 0905.3725. Cited in page(s): 2 and 76.

[61] J. McKeever, A. Boca, A. D. Boozer, R. Miller, J. R. Buck, A. Kuzmich, and H. J. Kimble, Science **303**, 1992 (2004), http://www.sciencemag.org/cgi/reprint/303/5666/1992.pdf, URL http://www.sciencemag.org/cgi/content/abstract/303/5666/1992. Cited in page(s): 2, 3, 76, and 92.

[62] M. Hijlkema, B. Weber, H. P. Specht, S. C. Webster, A. Kuhn, and G. Rempe, Nature Physics **3**, 253 (2007). Cited in page(s): 3, 76, and 92.

[63] M. Keller, B. Lange, K. Hayasaka, W. Lange, and H. Walther, Nature **431**, 1075 (2004). Cited in page(s): 3 and 70.

[64] H. G. Barros, A. Stute, T. E. Northup, C. Russo, P. O. Schmidt, and R. Blatt, New J. Phys. **11**, 103004 (2009), 0905.2885. Cited in page(s): 3 and 67.

[65] C. Russo, Ph.D. thesis, University of Innsbruck (2008). Cited in page(s): 3, 14, 15, 17, 20, 21, 31, 34, 35, 44, 47, 49, 53, 67, 72, 73, and 91.

[66] C. Gardiner and P. Zoller, *Quantum Noise* (Springer, Berlin, 2004). Cited in page(s): 5, 12, 17, and 21.

[67] R. Loudon, *The Quantum Theory of Light* (Oxford University Press, 1973). Cited in page(s): 6 and 19.

[68] B. D. C. Cohen-Tannoudji and F. Laloe, *Quantum Mechanics, Vol. 2* (Hermann and John Wiley and Sons, 1977). Cited in page(s): 6 and 20.

[69] D. Meschede, *Optics, Light and Lasers* (WILEY-VCH, 2007). Cited in page(s): 6.

[70] A. E. Siegman, *Lasers* (University Science Books, Sausalito, California, 1986). Cited in page(s): 7 and 35.

[71] M. O. Scully and M. S. Zubairy, *Quantum Optics* (Cambridge University Press, 1997). Cited in page(s): 8.

[72] E. Jaynes and F. Cummings, Proceedings of the IEEE **51**, 89 (1963). Cited in page(s): 8.

[73] L. Allen and J. H. Eberly, *Optical resonance and two-level atoms* (Wiley, 1975). Cited in page(s): 8.

[74] H. Carmichael, *An Open Systems Approach to Quantum Optics* (Springer-Verlag, 1993). Cited in page(s): 12.

[75] C. Maurer, C. Becher, C. Russo, J. Eschner, and R. Blatt, New J. Phys. **6**, 94 (2004). Cited in page(s): 12, 14, and 17.

[76] G. Lindblad, Commun. Math. Phys. **48**, 119 (1976). Cited in page(s): 13.

[77] C. J. Foot, *Atomic Physics* (Oxford University Press, 2005). Cited in page(s): 14 and 85.

[78] C. C. Gerry and J. H. Eberly, Phys. Rev. A **42**, 6805 (1990). Cited in page(s): 14.

[79] M. Alexanian and S. K. Bose, Phys. Rev. A **52**, 2218 (1995). Cited in page(s): 14.

[80] Y. Wu, Phys. Rev. A **54**, 1586 (1996). Cited in page(s): 14.

[81] C. Di Fidio, S. Maniscalco, W. Vogel, and A. Messina, Phys. Rev. A **65**, 033825 (2002). Cited in page(s): 14.

[82] F. Dubin, C. Russo, H. Barros, A. Stute, C. Becher, P. Schmidt, and R. Blatt (2009), in preparation. Cited in page(s): 15.

[83] M. Chwalla, J. Benhelm, K. Kim, G. Kirchmair, T. Monz, M. Riebe, P. Schindler, A. S. Villar, W. Hänsel, C. F. Roos, et al., Phys. Rev. Lett. **102**, 023002 (2009), 0806.1414. Cited in page(s): 17 and 79.

[84] S. M. Tan, J. Opt. B **1**, 424 (1999). Cited in page(s): 29.

[85] K. R. Vogel, S. A. Diddams, C. W. Oates, E. A. Curtis, R. J. Rafac, W. M. Itano, J. C. Bergquist, R. W. Fox, W. D. Lee, J. S. Wells, et al., Opt. Lett. **26**, 102 (2001). Cited in page(s): 29.

[86] C. Cohen-Tannoudji, J. Dupont-Roc, and G. Grynberg, *Atom-Photon Interactions: Basic Processes and Applications* (Wiley-VCH, New York, 1998). Cited in page(s): 29.

[87] W. Paul, Rev. Mod. Phys. **62**, 531 (1990). Cited in page(s): 31.

[88] D. Leibfried, R. Blatt, C. Monroe, and D. Wineland, Rev. Mod. Phys. **75**, 281 (2003). Cited in page(s): 32 and 33.

[89] M. G. Raizen, J. M. Gilligan, J. C. Bergquist, W. M. Itano, and D. J. Wineland, Phys. Rev. A **45**, 6493 (1992). Cited in page(s): 33.

[90] D. J. Wineland, C. Monroe, W. M. Itano, D. Leibfried, B. E. King, and D. M. Meekhof, J. Res. Natl. Inst. Stand. Technol. **103**, 259 (1998). Cited in page(s): 33 and 64.

[91] M. Drewsen and A. Brøner, PRA **62**, 045401 (2000). Cited in page(s): 33.

[92] M. Riebe, Ph.D. thesis, Universität Innsbruck (2005). Cited in page(s): 33, 79, 80, and 85.

[93] S. Gulde, Ph.D. thesis, Universität Innsbruck (2003). Cited in page(s): 33.

[94] R. W. P. Drever, J. L. Hall, F. V. Kowalski, J. Hough, G. M. Ford, A. J. Munley, and H. Ward, Appl. Phys. B **31**, 97 (1983). Cited in page(s): 37.

[95] E. D. Black, Am. J. of Phys. **69**, 79 (2001). Cited in page(s): 37.

[96] G. Kirchmair, Master's thesis, Universität Innsbruck (2007). Cited in page(s): 37.

[97] M. Chwalla, Ph.D. thesis, Universität Innsbruck (2009). Cited in page(s): 37, 40, and 79.

[98] T. W. Hänsch and A. L. Schawlow, Opt. Comm. **13**, 68 (1975). Cited in page(s): 37.

[99] D. J. Wineland, R. E. Drullinger, and F. L. Walls, Phys. Rev. Lett. **40**, 1639 (1978). Cited in page(s): 37.

[100] H. Rohde, Ph.D. thesis, University of Innsbruck (2001). Cited in page(s): 43.

[101] C. Kurtsiefer, P. Zarda, S. Mayer, and H. Weinfurter, J. Mod. Opt. **48**, 2039 (2001), arXiv:quant-ph/0104103. Cited in page(s): 48 and 71.

[102] T. Körber, *qfp manual* (2007). Cited in page(s): 51.

[103] D. Rotter, Ph.D. thesis, Universität Innsbruck (2008). Cited in page(s): 53.

[104] J. Eschner, Eur. Phys. J. D **22**, 341 (2003). Cited in page(s): 56 and 57.

[105] J. I. Cirac, R. Blatt, P. Zoller, and W. D. Phillips, Phys. Rev. A **46**, 2668 (1992). Cited in page(s): 64.

[106] P. Domokos and H. Ritsch, J. Opt. Soc. Am. B **20**, 1098 (2003), URL http://josab.osa.org/abstract.cfm?URI=josab-20-5-1098. Cited in page(s): 65.

[107] S. Zippilli and G. Morigi, Phys. Rev. A **72**, 053408 (pages 16) (2005), URL http://link.aps.org/abstract/PRA/v72/e053408. Cited in page(s): 65.

[108] D. R. Leibrandt, J. Labaziewicz, V. Vuletić, and I. L. Chuang, Phys. Rev. Lett. **103**, 103001 (2009), 0905.0148. Cited in page(s): 65 and 91.

[109] M. Keller, B. Lange, K. Hayasaka, W. Lange, and H. Walther, New J. Phys. **6**, 95 (2004). Cited in page(s): 74 and 91.

[110] R. Ozeri, C. Langer, J. D. Jost, B. DeMarco, A. Ben-Kish, B. R. Blakestad, J. Britton, J. Chiaverini, W. M. Itano, D. B. Hume, et al., Phys. Rev. Lett. **95**, 030403 (2005). Cited in page(s): 76.

[111] R. Ozeri, W. M. Itano, R. B. Blakestad, J. Britton, J. Chiaverini, J. D. Jost, C. Langer, D. Leibfried, R. Reichle, S. Seidelin, et al., Phys. Rev. A **75**, 042329 (2007). Cited in page(s): 76.

[112] C. Roos, Ph.D. thesis, Universität Innsbruck (2000). Cited in page(s): 79, 80, and 83.

[113] J. I. Cirac and P. Zoller, Phys. Rev. Lett. **74**, 4091 (1995). Cited in page(s): 79.

[114] J. Benhelm, Ph.D. thesis, Universität Innsbruck (2008). Cited in page(s): 87.

[115] C. Roos, T. Zeiger, H. Rohde, H. Nägerl, J. Eschner, D. Leibfried, F. Schmidt-Kaler, and R. Blatt, Phys. Rev. Lett. **83**, 4713 (1999). Cited in page(s): 87.

[116] F. Schmidt-Kaler, H. Häffner, M. Riebe, S. Gulde, G. P. T. Lancaster, T. Deuschle, C. Becher, C. F. Roos, J. Eschner, and R. Blatt, Nature **422**, 408 (2003). Cited in page(s): 92.

[117] M. Riebe, H. Häffner, C. F. Roos, W. Hänsel, J. Benhelm, G. P. T. Lancaster, T. W. Körber, C. Becher, F. Schmidt-Kaler, D. F. V. James, et al., Nature **429**, 734 (2004). Cited in page(s): 92.

[118] T. Steinmetz, Y. Colombe, D. Hunger, T. W. Hänsch, A. Balocchi, R. J. Warburton, and J. Reichel, Appl. Phys. Lett. **89**, 111110 (pages 3) (2006), URL http://link.aip.org/link/?APL/89/111110/1. Cited in page(s): 92.

[119] D. R. Leibrandt, Ph.D. thesis, Massachusetts Institute of Technology (2009). Cited in page(s): 92.

[120] F. Splatt, Ph.D. thesis, Universität Innsbruck (2009). Cited in page(s): 92.

[121] S. Seidelin, J. Chiaverini, R. Reichle, J. J. Bollinger, D. Leibfried, J. Britton, J. H. Wesenberg, R. B. Blakestad, R. J. Epstein, D. B. Hume, et al., Phys. Rev. Lett. **96**, 253003 (2006). Cited in page(s): 92.

Danksagung

I would first like to thank professor Rainer Blatt for giving me the great opportunity of working here. During these almost five years I have had the pleasure to be part of his group and acquire an immense amount of knowledge not only in Physics but also in several other areas ranging from electronics to performing public presentations. His experience in the field and his ability to quickly dive into our problems, suggesting the required solutions, have been of great importance throughout my doctoral thesis. The exciting work environment enriched by enjoyable and helpful people taught me to work in groups and, most importantly, provided me with the chance to further develop the ability to solve problems.

I would then like to thank professor Piet Schmidt for his undeniable optimism and interest in our project. As our project leader he has provided us with the demanded guidance and the necessary tools and ideas to perform our work in the best way possible. His open and joyful personality contributed to a pleasant work environment and motivated fruitful discussions.

A big thanks to my great CQED companions Andreas Stute, Tracy Northup, Birgit Brandstätter and Carlos Russo. You have helped me immensely through this time and have transformed dark work days and nights in the lab into a delight. Also thanks to Christoph Becher for his assistance in my first months here and further discussions about cavity QED and to Eoin Phillips for his help.

I would like to thank Frau Patricia Moser for the incredible help with bureaucratic problems and for the good advices. I would also like to thank the mechanical workshop people Helmut, Tony and Joseff for the help with building pieces and giving useful suggestions and also the electronics workshop people Manuel and Arthur for the support in fixing electronic devices.

Also thanks to other friends and work colleagues, specially Felicity, Rui and all the girls from LiP: our meetings have been really enjoyable! Special thanks to my dear friends Clarice and Börge. My life in Innsbruck has become much more interesting and fun after I have met you.

Ich möchte meiner lieben Mitbewohnerin Teresa danken. Du hast dich so nett um mich gekümmert wenn ich gestresst und ohne Zeit war.

Vielen Dank möchte ich auch Christians Familie sagen, im speziellen an Brigitte und Reinhard, für die großartige Unterstützung. Ihr habt mir Eure Arme und Euer Haus geöffnet und mich herzlich aufgenommen. Danke für die unzähligen schönen Wochenenden, voll mit gutem Essen, viel "Deutsch" (oder besser Dütsch), einigen Ausflügen und lustigen Spielen!

À minha família, muitíssimo obrigada pela enorme ajuda que vocês me deram. Sem o seu incentivo eu jamais teria vindo para cá e sem o seu apoio jamais teria conseguido permanecer aqui. Obrigada pela paciência nos meus momentos de estresse, pelo interesse pelas coisas que faço e principalmente pelo carinho que vocês me deram. Dedico a vocês esta tese e gostaria que soubessem que sem a presença de vocês em minha vida eu não seria quem eu sou e não alcançaria o que alcancei. Muito obrigada!

Finalmente, gostaria de agradecer a Christian pela fantástica companhia e pelo incomensurável apoio. Sua alegria e capacidade de me fazer sentir bem comigo mesma e, acima de tudo, feliz e amada contribuíram enormemente na luta contra a solidão e a saudade de minha família. Com sua ajuda consegui enfrentar problemas que precisavam ser resolvidos e aliviar dores que não tinham fim. Com você, construí um novo lar que me proporcionou uma estadia ainda mais prazerosa neste continente que aprendo a cada dia a aproveitar mais. Obrigada por tudo!